

## The Evolving Interstellar Medium of Star-Forming Galaxies, as traced by Stardust\*

VASILY I. KOKOREV,<sup>1,2</sup> GEORGIOS E. MAGDIS,<sup>1,3,2</sup> IARY DAVIDZON,<sup>1,2</sup> GABRIEL BRAMMER,<sup>1,2</sup> FRANCESCO VALENTINO,<sup>1,2</sup>  
EMANUELE DADDI,<sup>4</sup> LAURE CIESLA,<sup>5,4</sup> DAIZHONG LIU,<sup>6</sup> SHUOWEN JIN,<sup>7,8</sup> ISABELLA CORTZEN,<sup>9</sup> IVAN DELVECCHIO,<sup>10,4</sup>  
CLARA GIMÉNEZ-ARTEAGA,<sup>1,2</sup> CARLOS GÓMEZ-GUIJARRO,<sup>4</sup> MARK SARGENT,<sup>11</sup> SUNE TOFT,<sup>1,2</sup> AND JOHN R. WEAVER<sup>1,2</sup>

<sup>1</sup>*Cosmic Dawn Center (DAWN), Jagtvej 128, DK2200 Copenhagen N, Denmark*

<sup>2</sup>*Niels Bohr Institute, University of Copenhagen, Blegdamsvej 17, DK2100 Copenhagen Ø, Denmark*

<sup>3</sup>*DTU-Space, Technical University of Denmark, Elektrovej 327, DK2800 Kgs. Lyngby, Denmark*

<sup>4</sup>*CEA, Irfu, DAP, AIM, Université Paris-Saclay, Université de Paris, CNRS, F-91191 Gif-sur-Yvette, France*

<sup>5</sup>*Aix Marseille Univ, CNRS, CNES, LAM, Marseille, France*

<sup>6</sup>*Max-Planck-Institut für Extraterrestrische Physik (MPE), Giessenbachstr. 1, D-85748 Garching, Germany*

<sup>7</sup>*Instituto de Astrofísica de Canarias (IAC), E-38205 La Laguna, Tenerife, Spain*

<sup>8</sup>*Universidad de La Laguna, Dpto. Astrofísica, E-38206 La Laguna, Tenerife, Spain*

<sup>9</sup>*Institut de Radioastronomie Millimétrique (IRAM), 300 ruède la Piscine, 38400 Saint-Martin-d'Hères, France*

<sup>10</sup>*INAF - Osservatorio Astronomico di Brera, via Brera 28, I-20121, Milano, Italy & via Bianchi 46, I-23807, Merate, Italy*

<sup>11</sup>*Astronomy Centre, Department of Physics and Astronomy, University of Sussex, Brighton, BN1 9QH, UK*

(Received February 26, 2021; Revised June 28, 2021; Accepted July 10, 2021)

Submitted to ApJ

### ABSTRACT

We analyse the far-infrared properties of  $\sim 5,000$  star-forming galaxies at  $z < 4.5$ , drawn from the deepest, super-deblended catalogues in the GOODS-N and COSMOS fields. We develop a novel panchromatic SED fitting algorithm, **Stardust**, that models the emission from stars, AGN, and infrared dust emission, without relying on energy balance assumptions. Our code provides robust estimates of the UV-optical and FIR physical parameters, such as the stellar mass ( $M_*$ ), dust mass ( $M_{\text{dust}}$ ), infrared luminosities ( $L_{\text{IR}}$ ) arising from AGN and star formation activity, and the average intensity of the interstellar radiation field ( $\langle U \rangle$ ). Through a set of simulations we quantify the completeness of our data in terms of  $M_{\text{dust}}$ ,  $L_{\text{IR}}$  and  $\langle U \rangle$ , and subsequently characterise the distribution and evolution of these parameters with redshift. We focus on the dust-to-stellar mass ratio ( $f_{\text{dust}}$ ), which we parametrise as a function of cosmic age, stellar mass, and specific star formation rate. The  $f_{\text{dust}}$  is found to increase by a factor of 10 from  $z = 0$  to  $z = 2$  and appears to remain flat at higher- $z$ , mirroring the evolution of the gas fraction. We also find a growing fraction of warm to cold dust with increasing distance from the main sequence, indicative of more intense interstellar radiation fields, higher star formation efficiencies and more compact star forming regions for starburst galaxies. Finally, we construct the dust mass functions (DMF) of star-forming galaxies up to  $z = 1$  by transforming the stellar mass function to DMF through the scaling relations derived here. The evolution of  $f_{\text{dust}}$  and the recovered DMFs are in good agreement with the theoretical predictions of the Horizon-AGN and IllustrisTNG simulations.

*Keywords:* galaxies: evolution — galaxies: high-redshift — galaxies: ISM — submillimeter: ISM

### 1. INTRODUCTION

One of the main mechanisms driving galaxy evolution is the interaction between the interstellar medium (ISM), primarily consisting of gas and dust, and the radiation field induced by stellar activity. In this context, dust poses challenges in the detection of the UV/optical emission of galaxies and in the interpretation of these observations in terms of physical properties (e.g. star for-

Corresponding author: Vasily Kokorev  
vasilii.kokorev@nbi.ku.dk

\* <https://github.com/VasilyKokorev/stardust/>

mation rate (SFR), stellar mass  $M_*$ , etc), but also is an important tracer of star formation and ISM in the FIR observations. At the same time, dust shields cold molecular hydrogen from ionising photons, and facilitates the collapse of molecular gas and subsequent star formation (Goldsmith 2001; Krumholz et al. 2011; Narayanan et al. 2011, 2012; Narayanan & Davé 2012). As such, dust plays a critical role in the life cycle of galaxies and offers observational signatures regarding their past evolutionary stages.

The impressive variety of infrared and millimetre facilities commissioned in the last few decades have propelled the extragalactic ISM studies at an ever increasing number, redshift, and detail. Indeed, the enormous observational efforts manifested by the large far-IR/mm imaging and spectroscopic surveys such as PEP (Lutz et al. 2011), GOODS-Herschel (Elbaz et al. 2011), PHIBBS (Tacconi et al. 2013), S2CLS (Geach et al. 2017) and many others (e.g. Oliver et al. 2012; Magnelli et al. 2013; Walter et al. 2016; Saintonge et al. 2017; Dunlop et al. 2017; Maddox et al. 2018; Franco et al. 2020; Valentino et al. 2020; Béthermin et al. 2020; Reiter et al. 2020, for a review see Carilli & Walter 2013 and Hodge & da Cunha 2020) have yielded a wealth of multi-wavelength data sets and have advanced our understanding of galaxy evolution through scaling relations that have been used to guide simulations and theoretical models (e.g. Dekel et al. 2009; Popping et al. 2014; Narayanan et al. 2015; Lagos et al. 2015, 2020; Popping et al. 2017; Davé et al. 2017, 2020).

In the evolutionary picture that is emerging from the analysis of the FIR/mm surveys, the majority of star-forming galaxies (SFGs) follow a tight relation – the Main Sequence (MS) – between the SFR and  $M_*$  with an increasing normalisation factor (specific star-formation rate,  $\text{sSFR} = \text{SFR}/M_*$ ) at least up to  $z \sim 4$  (Brinchmann et al. 2004; Daddi et al. 2007; Elbaz et al. 2007; Noeske et al. 2007; Salim et al. 2007; Chen et al. 2009; Pannella et al. 2009; Santini et al. 2009; Daddi et al. 2010; Elbaz et al. 2010; Oliver et al. 2010; Magdis et al. 2010; Elbaz et al. 2011; Karim et al. 2011; Rodighiero et al. 2011; Shim et al. 2011; Lee et al. 2012; Reddy et al. 2012; Salmi et al. 2012; Whitaker et al. 2012; Zahid et al. 2012; Kashino et al. 2013; Moustakas et al. 2013; Rodighiero et al. 2014; Sargent et al. 2014; Steinhardt et al. 2014; Sobral et al. 2014; Speagle et al. 2014; Whitaker et al. 2014; Lee et al. 2015; Schreiber et al. 2015; Shivaei et al. 2015; Tasca et al. 2015; Whitaker et al. 2015; Erfanianfar et al. 2016; Kurczynski et al. 2016; Santini et al. 2017; Pearson et al. 2018; Leslie et al. 2020). This elevation of  $\text{sSFR}$  with lookback-time, which broadly mirrors the overall increase of the star-formation rate density of the

Universe from  $z = 0$  to  $z = 2 - 3$ , is also followed by a similar rise in the gas fraction ( $f_{\text{gas}} = M_{\text{gas}}/M_*$ ) of SFGs (e.g. Daddi et al. 2010; Geach et al. 2011; Magdis et al. 2012a,b; Tacconi et al. 2013; Liu et al. 2019a,b). Nevertheless, for fixed  $M_*$ , the increase in star-formation efficiencies ( $\text{SFE} = \text{SFR}/M_{\text{gas}}$ ) surpasses that in  $M_{\text{gas}}$ , resulting in higher SFR, an activity that coupled with the observed  $M_*$ -size evolution (e.g. van der Wel et al. 2014) instils warmer luminosity-weighted dust temperatures of the ISM as a function of redshift (e.g. Magdis et al. 2012a, 2017; Magnelli et al. 2014; Béthermin et al. 2015; Casey et al. 2018; Schreiber et al. 2018; Liang et al. 2019; Cortzen et al. 2020).

Although the purity of the MS as a measure of the evolutionary stage of a galaxy has recently been challenged (e.g. Elbaz et al. 2018; Puglisi et al. 2019; Valentino et al. 2020), it appears that the majority of SFGs grow along the MS by secularly converting (and hence depleting) their gas mass reservoirs into stars (e.g. Daddi et al. 2010; Davé et al. 2012; Lilly et al. 2013; Tacchella et al. 2016), with a high degree of uniformity in the properties of their ISM (at fixed redshift). On the other hand, galaxies above the MS (starbursts; hereafter SBs) are primarily characterised by elevated  $\text{sSFR}$ , SFE and dust temperature ( $T_{\text{d}}$ ) with respect to the average star-forming population at their corresponding redshift (e.g. Daddi et al. 2010; Magdis et al. 2012a; Magnelli et al. 2014; Scoville et al. 2017; Tacconi et al. 2018; Silverman et al. 2018). Galaxies below the MS are mainly post starbursts or quenched systems with low levels of star-formation activity, low gas fractions and cold  $T_{\text{d}}$  (e.g. Williams et al. 2020; Magdis et al. 2021).

At the core of the aforementioned results is the robustness of the derived FIR properties, namely the total infrared luminosity ( $L_{\text{IR}}$ ), the dust mass ( $M_{\text{dust}}$ ), the mean intensity of the radiation field ( $\langle U \rangle \propto L_{\text{IR}}/M_{\text{dust}}$ ) and  $T_{\text{d}}$ . These quantities and their emerging evolution with redshift rely on the availability of FIR/mm data and on selection effects. In this regard, while the ongoing ALMA observations are quickly filling the gap in resolution and sensitivity between the available UV/optical/NIR (sub-arcsecond) data and the coarse resolution of the confusion-limited SCUBA2 and SPIRE/*Herschel* surveys, the vast majority of the SFG samples with available FIR photometry are still restricted to the latter. Thus, FIR studies are still largely focusing either on the FIR luminous and most massive SFGs, on limited and possibly non-homogeneous or biased ALMA samples, or on stacking techniques.

Moreover, the derived measurements of  $M_{\text{dust}}$  and  $T_{\text{d}}$  heavily rely on the adopted models and fitting techniques (e.g. Dale et al. 2014; Berta et al. 2016). In-

deed, without a coherent and homogeneous treatment of the data sets it is impossible to overcome systematic effects that could distort the observed trends. On top of that, recent high-resolution observations with ALMA indicate that the UV/optical and millimetre emission of some of high- $z$  SFGs are spatially distinct (e.g. Hodge et al. 2016), posing challenges to the widely adopted energy balance assumption that is inherent in most multi-wavelength fitting codes. Similarly, there is an ever increasing number of IR bright yet optically faint/dark sources (e.g. Wang et al. 2016; Jin et al. 2019; Casey et al. 2019; Franco et al. 2020) that an energy balance approach would have technical difficulties to accommodate.

Finally, while many studies have focused on  $f_{\text{gas}}$ , the evolution of the dust fraction ( $f_{\text{dust}} = M_{\text{dust}}/M_*$ ) and the dust mass function (DMF) with redshift have not been scrutinised to the same extent (Dunne et al. 2011; Magdis et al. 2012a; Santini et al. 2014; Tan et al. 2014; Béthermin et al. 2015; Driver et al. 2018; Magnelli et al. 2020; Donevski et al. 2020). Given that the use of  $M_{\text{dust}}$  as a proxy of  $M_{\text{gas}}$  either through the metallicity dependent dust-to-gas mass ratio technique (e.g. Leroy et al. 2011; Eales et al. 2012; Magdis et al. 2011, 2012a; Berta et al. 2016; Tacconi et al. 2018) or (indirectly) through the monochromatic flux densities in the Rayleigh-Jeans (R-J) tail of the SED (e.g. Groves et al. 2015; Scoville et al. 2017) has gained momentum, a proper investigation of the evolution of  $f_{\text{dust}}$  and DMF with redshift is necessary, and remains to be done. More importantly, the  $f_{\text{dust}}$ , the DMFs and in general the life cycle of dust are key in our understanding of metal enrichment processes and dust production mechanisms. These derived properties are also critical parameters of semi-analytical and analytical models that couple the evolution of stars, metals, and gas (Lacey et al. 2016; Popping et al. 2017; Imara et al. 2018; Cousin et al. 2019; Vijayan et al. 2019; Lagos et al. 2019; Pantoni et al. 2019), as well as of cosmological simulations that also trace the dark matter component (Hayward et al. 2013; Narayanan et al. 2015; McKinnon et al. 2017; Davé et al. 2019; Aoyama et al. 2019).

These considerations provide motivation for a coherent and homogeneous analysis of the full population of IR galaxies that are detected in the recently constructed, state-of-the-art ‘Super-Deblended’ FIR catalogues in two of the most extensively studied cosmological fields, the Great Observatories Origins Deep Survey North (GOODS-N; Dickinson et al. 2003) and the Cosmic Evolution Survey (COSMOS; Scoville et al. 2007). These catalogues are built using the ‘Super-Deblending’ technique (Liu et al. 2018; Jin et al. 2018) that allows

prior-based source extraction from highly confused *Herschel* and *SCUBA+AzTEC* maps, yielding robust UV to radio photometry for thousands of individually detected galaxies. To model the observed SEDs we built and make publicly available a novel, time efficient and panchromatic SED fitting algorithm that we use to infer and explore the evolution and the variations of IR properties of SFGs ( $M_{\text{dust}}$ ,  $T_{\text{d}}$ ,  $\langle U \rangle$ ,  $f_{\text{dust}}$ ,  $f_{\text{gas}}$ , DMF) out to  $z \sim 4$  and compare those to recent theoretical predictions. The catalogues with the derived FIR parameters for the full sample are also publicly released.

The paper is organised as follows. In Section 2 we describe the data sets used in this work, while Section 3 introduces our SED fitting algorithm. In Section 4 we perform various simulations to determine the robustness of our sample, as well as the limiting  $M_{\text{dust}}$ . Section 5 presents our physical estimates for each galaxy in the sample, and their evolution with  $z$ . In Section 6 we analyse the evolution of  $f_{\text{dust}}$  and calculate the DMF through the conversion of the stellar mass function (SMF). In Section 7 we constrain the evolution of  $f_{\text{gas}}$  and compare it to the literature results. We discuss the implications that our findings have in Section 8, and present our main conclusions and summary in Section 9.

Throughout this paper we assume a flat  $\Lambda$ CDM cosmology with  $\Omega_{\text{m},0} = 0.3$ ,  $\Omega_{\Lambda,0} = 0.7$  and  $H_0 = 70 \text{ km s}^{-1} \text{ Mpc}^{-1}$ , and a Chabrier (2003) initial mass function (IMF).

## 2. PANCHROMATIC CATALOGUES AND SAMPLE SELECTION

### 2.1. GOODS-N ‘Super-Deblended’ Catalogue

We first consider the ‘Super-Deblended’ photometric catalogue (hereafter SDC1) constructed by Liu et al. (2018) using the FIR and sub-mm images in GOODS-N. These images come from the *Herschel* Space Observatory (PACS and SPIRE instruments, see Elbaz et al. 2011; Magnelli et al. 2013) and the ground-based facilities SCUBA-2 (850  $\mu\text{m}$ ; Geach et al. 2017) and AzTEC+MAMBO (1.16 mm; Penner et al. 2011).

Several novelties introduced in SDC1 are particularly useful for our analysis. First, detections from deep Spitzer IRAC and VLA 20 cm (Owen 2018) are used as a prior for the positions of the blended FIR/sub-mm sources. Second, the SED information from shorter-wavelength photometry is also used as a prior for subtracting lower redshift sources. This substantially decreases blending degeneracies and allows for a robust photometry extraction of sources at longer wavelengths. Moreover, the authors estimated more realistic photometry uncertainties for each photometric measurement with extensive Monte Carlo simulations. These improve-

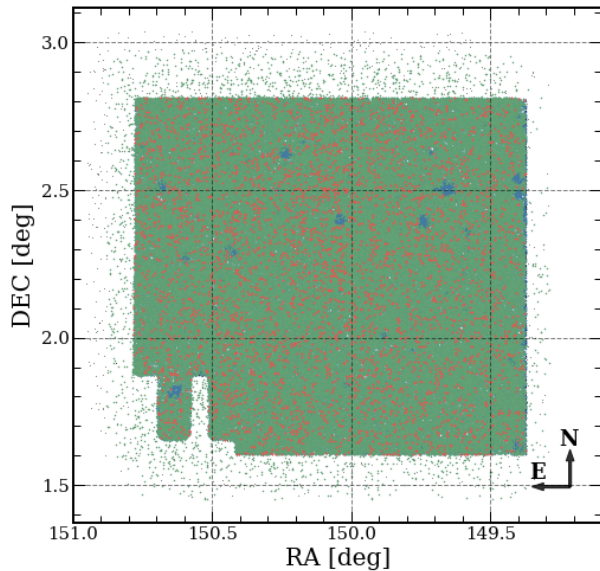


**Figure 1.** COSMOS sky map. The blue regions and black points represent sources from Muzzin et al. (2013) with `goodArea` = 1 and 0 respectively (according to the quality flag in Jin et al. 2018 catalogue). The Laigle et al. (2016) coverage is shown in green. Sources that we use for our analysis are indicated in red.

ments allow for deeper detection limits and statistically reliable estimates (both measurements and uncertainties) in the FIR+mm bands.

The SDC1 contains 3,306 priors in total, including over 1,000 FIR+mm detections. All sources have photometric redshifts and stellar masses inferred by EAZY (Brammer et al. 2008), and FAST (Kriek et al. 2009) respectively, based on the 3D-HST UV-near-IR (Skelton et al. 2014) and Pannella et al. 2015 GOODS-N catalogues. Following Liu et al. (2018), we extend the photometric coverage of the published SDC1 catalogue to shorter wavelengths by cross-matching with the 3D-HST UV-near-IR (Skelton et al. 2014) and Pannella et al. 2015 GOODS-N catalogues. Approximately half of the objects within the catalogue are spectroscopically confirmed. However, as mentioned by the authors, the outer perimeter of the GOODS-N area contains objects with high instrumental noise in the  $24\mu\text{m}$  prior image that may impair the extraction process. We therefore choose to limit our analysis to the central  $134\text{arcmin}^2$  with reliable photometry (flag `goodArea` = 1 in SDC1). This reduced our final sample to 2,344 objects.

## 2.2. COSMOS ‘Super-Deblended’ Catalogue

We supplement our study with the ‘Super-Deblended’ catalogue (SDC2 hereafter) presented in Jin et al. (2018). The catalogue covers  $1.7\text{deg}^2$  in COSMOS, in the same bands as in SDC1, plus additional MAMBO data at 1.2 mm (Bertoldi et al. 2007).

In practice, the deblending methodology remains identical to that adopted in SDC1, with one primary difference: an additional step selecting a highly complete sample of priors in  $K_s$  band from the UltraVista catalogues (McCracken et al. 2012). The resulting  $24\mu\text{m}$  detections are then combined with the mass-limited sample of  $K_s$  sources in order to fit the remaining bands in the catalogue.

The final input dataset contains 195,107 priors, with 13% of them having spectroscopic confirmation. The authors highlight that only 11,220 objects are in fact detected over the  $100\text{--}1200\mu\text{m}$  range. Similarly to GOODS-N, we impose the `goodArea` = 1 flag to only include sources that are present in the UltraVista Data Release 4 area (McCracken et al. 2012).

We note that for their catalogue, Jin et al. (2018) used a combination of Laigle et al. (2016) and Muzzin et al. (2013) (M13 hereafter) catalogues. The M13 catalogue has an advantage in that it does not completely remove the sources around saturated stars, which has a positive effect on the number counts, however the reduced quality of the photometry could lead to unreliable estimates for photometric redshifts ( $z_{\text{phot}}$ ), as well as any parameters extracted by fitting optical templates. To be on the safe side, our analysis of SDC2 will only focus on the Laigle et al. 2016 sources, which narrows down the number of objects in the input catalogue to 186,549 and the total area to  $1.38\text{deg}^2$ . The COSMOS 2015 catalogue (Laigle et al. 2016), also comes with a plethora of UV-optical photometry, spanning an additional  $\sim 20$  bands, as well as photometric redshifts and stellar mass estimates by LePhare (Arnouts et al. 1999; Ilbert et al. 2006). We exploit these data by cross-matching the same COSMOS 2015 UV-optical photometry that was used to derive  $M_*$  and redshift to SDC2, thus extending our photometric coverage. In total, the merged catalogues consist in  $\sim 40$  bands.

For posterity, in Figure 1 we present the UltraVista Data Release 2 map (Laigle et al. 2016; Davidzon et al. 2017) (L16 area), with the regions where the star subtraction took place being clearly identified. In addition to that, on the West border of the survey there exists a number of sources falling outside of the L16 area. These only have UltraVista coverage and lack additional *Subaru* photometry, which could affect the reliability of the  $z_{\text{phot}}$ .



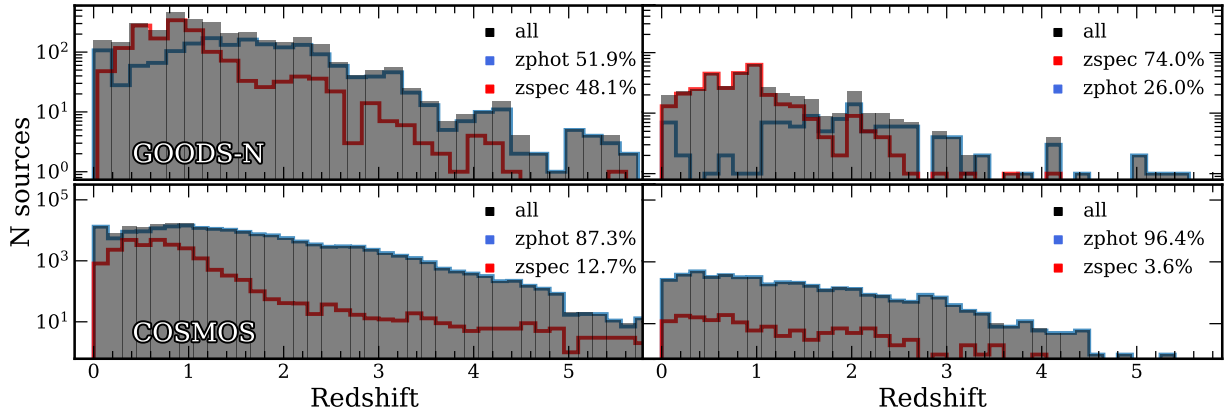


**Figure 2.** Redshift distributions of the sources considered in the present work. Both the photometric and spectroscopic redshifts were taken from the corresponding SDCs. The left and right panels show the redshift distribution of the original, full catalogue and of the final sample that meets the selection criteria described in Section 2.3, respectively.

### 2.3. Sample Selection

The primary parameters that we can derive from observing the rest-frame FIR emission are the total infrared luminosity ( $L_{\text{IR}}$ ), the dust mass ( $M_{\text{dust}}$ ), and  $T_{\text{d}}$  or equivalently the intensity of interstellar radiation field ( $U$ ) in the Draine & Li (2007) dust model. To obtain robust estimates for these parameters, an adequate multi-wavelength sampling of a galaxy’s SED is required. As such, constraining the IR-peak is necessary for a robust  $L_{\text{IR}}$  estimate, while detections in the long wavelength regime (Rayleigh-Jeans) are imperative to capture the emission from cold dust.

With these considerations in mind, after the initial cleaning of the catalogues described above, we perform our sample selection based on the following requirements:

- Detection at a  $S/N > 3$  significance in at least three FIR to sub-mm bands from  $100 \mu\text{m}$  to  $1.2 \text{ mm}$ <sup>1</sup>.
- Available  $z_{\text{phot}}$  (or  $z_{\text{spec}}$ ) and  $M_*$  estimates inferred by UV to near-IR photometry

After the quality cuts and the selection criteria, we are left with 4,331 objects in COSMOS and 585 sources in GOODS-N, which constitute our sample. We have additionally identified 75 objects within SDC2, that fulfil our FIR detection criteria, but despite having a well sampled UV-optical photometry, do not have either  $z_{\text{phot}}$  or  $M_*$  estimates. We subsequently fit these sources with EAZY (Brammer et al. 2008), extract their  $z_{\text{phot}}$ , as well as other UV-optical properties, and add them to our final

catalogue. This brings the total amount of COSMOS sources to 4,406. The  $z_{\text{phot}}$  and  $z_{\text{spec}}$  distributions of the final sample in the two fields are presented in Figure 2 (right). As we will discuss later, a third criterion requesting at least one detection at  $\lambda_{\text{rest}} > 150 \mu\text{m}$  will be imposed in order to define a sub-sample with robust  $M_{\text{dust}}$  estimates.

## 3. SED FITTING

### 3.1. The Inventory of Available SED fitting routines

Prior to providing the description of our methodology, we believe it is important to outline and present a brief introduction of the available SED fitting codes that deal with a three component fitting approach, namely combining the optical, AGN and dust emissions. These include the well established and widely used energy-balance routines such as CIGALE (Burgarella et al. 2005; Noll et al. 2009; Boquien et al. 2019), MAGPHYS (da Cunha et al. 2008; Battisti et al. 2019) as well as its AGN template extension presented in Chang et al. 2017. These have inspired more novel and sophisticated approaches that optimise the template libraries to achieve significant improvements in computational speeds - SED3FIT (Berta et al. 2013), or adopt MCMC methods when extracting best fit parameters such as AGNfitter (Calistro Rivera et al. 2016) and Prospector- $\alpha$  (Leja et al. 2018). These efforts are not just limited to published software packages, with many authors implementing their own routines for a panchromatic model analysis (e.g. see Feltre et al. 2013; Symeonidis et al. 2013).

### 3.2. Basic Description of the Stardust Fitting Code

<sup>1</sup> Three bands are also required to reduce fitting degeneracies

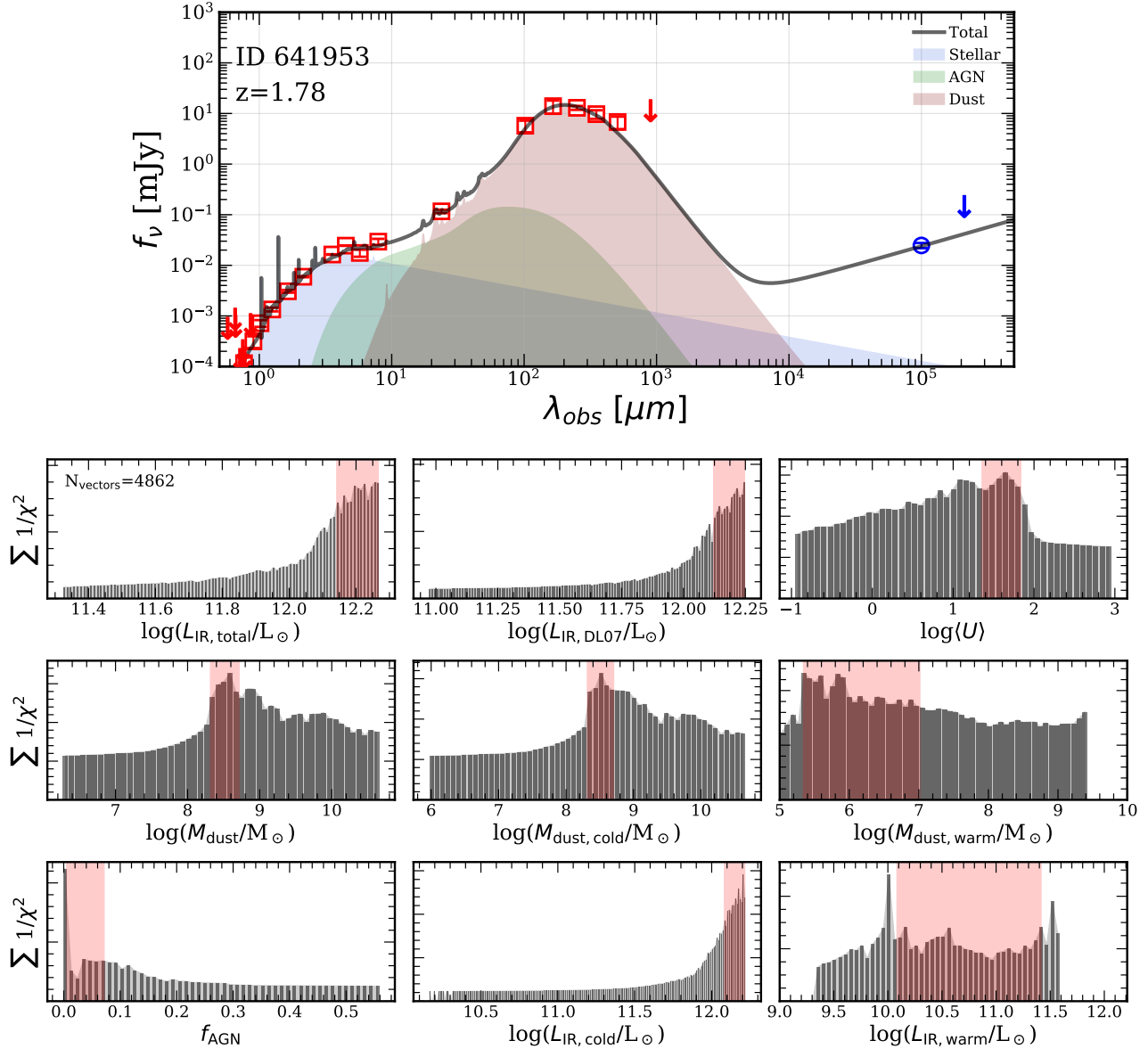


**Figure 3. Top:** Example of an observed and best fit SED, as obtained with **Stardust** code for a  $z_{phot} = 1.78$  galaxy (ID641953) drawn from the SDC2 sample. The squares and circles represent the  $S/N > 3$  photometric detections while  $3\sigma$  upper limits are shown as downward arrows. Red symbols represent the SDC2 photometry that was used in our fitting routine, while blue symbols show the radio measurements at 1.4 GHz and 3 GHz that were not included in the fit. Instead, the radio part of the model SED is based on the  $L_{IR} - L_{1.4\text{GHz}}$  relation of [Delvecchio et al. \(2020\)](#). The shaded red, green and blue regions, correspond to the dust, AGN and stellar components respectively. A linear combination of all three is given by a solid black line. **Bottom:** The  $\chi^2$  distributions for the main derived parameters. The shaded red areas enclose solutions for which  $\Delta\chi^2 = 1$ .

To model the extensive photometric coverage of the galaxies in our sample we develop a new, panchromatic SED fitting tool: **Stardust**. The code performs a multi-component fit that linearly combines stellar libraries with AGN torus templates and IR models of dust emission arising from star-formation (SF-IR). This approach, which is very similar to that presented in ([Liu et al. 2021](#)), has a number of key differences compared to the

currently existing SED fitting codes such as **MAGPHYS**, **CIGALE** and **SED3FIT**.

First, the three components (stellar, AGN and SF-IR) are fit simultaneously yet independently from each other, without assuming an energy balance between the absorbed UV/optical radiation and the IR emission. The energy balance approach relies on the assumption that fitted stellar and dust emissions are co-

spatial, i.e. the process of UV absorption and subsequent re-emission at IR wavelength happen in the same environment (da Cunha et al. 2008, e.g. see their Section 2.1 and 2.2). However, the detected stellar and dust distributions within a galaxy are not always physically connected. Resolved observations of high- $z$  dusty-SFGs (DSFGs) (Simpson et al. 2015; Gómez-Guijarro et al. 2018; Franco et al. 2018; Hodge et al. 2016, 2019; Kaasinen et al. 2020) have revealed spatial offsets between the extent of the dust and stellar emitting sizes of high- $z$  DSFGs, with the former being on average more compact (e.g. Chen et al. 2017; Tadaki et al. 2017; Calistro Rivera et al. 2018; Cochrane et al. 2021). While energy balance is anticipated to apply universally, the aperture and sensitivity limitations of our observations cast a concern on how reliably we can bring these components together in the same panchromatic fit. These observations are also theoretically supported by radiative transfer codes (e.g. SKIRT, Cochrane et al. 2019) and hydrodynamical simulations (e.g. IllustrisTNG, Pillepich et al. 2019; Popping et al. 2021).

Moreover, the detection of ‘HST-dark’ galaxies, i.e. sources that are undetected in the UV/optical bands, and thus do not have the photometry to constrain neither dust absorption nor stellar emission, but are bright in the IRAC and FIR/mm bands (Wang et al. 2016; Franco et al. 2018), pose another technical challenge to the correct application of the energy balance approach. Finally, the manner in which dust and stellar emission are connected, by assuming a single dust attenuation law and dust composition, can have a significant impact on derived parameters, as these recipes have been shown not to apply universally (Buat et al. 2019). In summary, while the premise of the energy balance routines is undoubtedly elegant and in most cases physically motivated, we choose to use independent stellar, AGN, and dust components to better focus on the dust properties themselves.

Furthering this complex picture, it is important to note the presence of cold diffuse dust, that is being heated by an older stellar population, rather than an ongoing star-formation activity, (see Boquien et al. 2011; Bendo et al. 2012; Galametz et al. 2014; Hayward et al. 2014). However, when dealing with non-resolved observations, the diffuse dust and RJ-tail emissions are highly degenerate, and as such none of the aforementioned codes, nor **Stardust**, utilise these templates.

The other advantage of **Stardust** is related to the  $\chi^2$  minimisation approach to select the best fit models. Instead of finding the solution from a vast library of pre-compiled templates, we devise an optimisation method to find the best linear combination of a much smaller

set of ‘basic’ templates (similar to eigenvectors in principal component analysis). This is the same approach adopted in the photometric redshift fitting code **EAZY** (Brammer et al. 2008). In our case, the basic templates are divided in three classes and the linear combination includes a sum of templates from these classes. The models used to create these templates are the following:

- **Stellar library.** We incorporate an updated version of the Stellar Population Synthesis (SPS) models described in Brammer et al. (2008). Although UV and optical photometry is not always available, the inclusion of the stellar component in the code is important in the NIR regime. In particular, it allows to better constrain the AGN contribution (see Figure 18 and Appendix A). This stellar library represents an optimised basis-set, where the non-negative linear combinations of models can be considered to be the “principal components” of a much larger parent template catalogue (see Brammer et al. 2008 and Blanton & Roweis 2007).
- **AGN library.** We adopt empirically derived templates from Mullaney et al. (2011) describing AGN intrinsic emission from 6 to 100  $\mu\text{m}$ <sup>2</sup>. We include both high- and low-luminosity templates (total of 2). Since these can be linearly combined, we do not include the median luminosity AGN template.
- **Infrared library.** It consists in 4,862 Draine & Li 2007 (DL07 hereafter) templates, with the additional updates from Draine et al. 2014 (also see Aniano et al. 2020). These models describe the contribution from warm dust and polycyclic aromatic hydrocarbon (PAH) features in the photodissociation regions (PDR), together with cold dust in the diffuse part of the ISM. We consider<sup>3</sup> a wide array of values for the minimum radiation field ( $U_{\text{min}}$ ) in the  $0.1 < U_{\text{min}} < 50$  range, as well as the fraction of the total dust mass locked in PAHs ( $q_{\text{PAH}}$ ) between 0 and 10 %. We have fixed  $U_{\text{max}} = 10^6$  and  $\alpha = 2$ , as described in Magdis et al. 2012a. These templates are not linearly combined within their class, the algorithm instead chooses a single best-fit DL07 template.
- **Radio continuum.** Data points in radio are not considered by our fitting routine, however they can

<sup>2</sup> Note: These templates do not account for X-ray selected QSOs. The flexible nature of the code however allows these templates to be manually injected if necessary.

<sup>3</sup> The modular structure of the code allows the user to decide which DL07 templates to use.

be used a posteriori to quantify possible radio excess and further confirm the presence of an AGN, if needed. Our radio model is based on the radio-FIR correlation, described in [Delvecchio et al. \(2020\)](#), with a spectral index of  $-0.75$ .

More details on the characteristics of the templates and the motivation for selecting them are provided in [Appendix A](#). With such a configuration, fitting a single object (including the computation of the uncertainties) with **Stardust** takes less than 10 seconds<sup>4</sup>, i.e. a factor of 8-10 faster than software like **CIGALE** (see [Appendix C](#)), based on large pre-compiled template sets. If we choose to pre-compile all of our templates, instead of linearly combining them, the resulting model library would contain millions of possible SEDs, with computation time increasing by a significant amount. The code is also highly parallelised, which allows it to run on multiple threads simultaneously, thus achieving significant computation speeds on modern CPUs.

### 3.3. Configuration of the Code

For each object, the input consists of measured flux densities, their corresponding uncertainties and a redshift estimate.<sup>5</sup> The user must then choose the corresponding filter curves from the pre-compiled set, or upload their own. The individual template components can be switched off and on as an additional user input. The algorithm then outputs the best-fit FIR as well as AGN properties of the source. If the photometry is available, the UV-optical parameters are also produced. These can be summarised as follows:

- The total infrared luminosity integrated over the SF-IR+AGN templates ( $L_{\text{IR,total}}$ )<sup>6</sup>, the total infrared luminosity associated with star-formation ( $L_{\text{IR,DL07}}$ ) and the relative contribution of the PDR component ( $f_{\text{PDR}}$ ) to  $L_{\text{IR,DL07}}$ .
- The bolometric IR luminosity of the AGN ( $L_{\text{AGN}}$ ) and its fractional contribution ( $f_{\text{AGN}}$ ) to the total IR energy budget<sup>7</sup>.
- The total dust mass ( $M_{\text{dust}}$ ), the warm dust mass component heated by PDRs ( $M_{\text{dust}}^{\text{warm}}$ ), the fraction

of the total dust mass heated by PDRs ( $\gamma$ ), the cold dust mass component ( $M_{\text{dust}}^{\text{cold}}$ ) in the diffuse ISM, and the fraction of the total dust mass locked in PAHs  $q_{\text{PAH}}$ .

- The intensity of the radiation field at which the diffuse ISM is exposed to ( $U_{\text{min}}$ ), which is a proxy of the mass-weighted  $T_{\text{d}}$  of the ISM, and the mean radiation field intensity ( $\langle U \rangle$ ), which is a proxy of the luminosity-weighted  $T_{\text{d}}$ .
- The stellar mass ( $M_*$ ), star-formation history (SFH),  $E(B-V)$  and the unobscured SFR, if there is available optical photometry.

[Figure 3](#) presents an example fit to one of the COSMOS galaxies, chosen for its prominent AGN contribution. The top panel of the Figure shows the data points and the best-fit model, with different colours for the four components listed above; the bottom panel displays the  $\chi^2$  distributions of all relevant IR quantities.

### 3.4. Derivation of Uncertainties

In order to estimate the errors associated with the derived quantities during the fitting procedure of **Stardust**, we consider two main sources of uncertainty; one concerning the linear combination coefficients of the best-fit optimisation and one linked to the broad-band photometric data.

To quantify the linear combination uncertainty, we re-sample the best solution coefficients. A covariance matrix is first created by considering all of the templates that went into the best-fit solution. We draw the coefficients from a multivariate normal distribution whose median are given by the coefficient of the best-solution vector and the standard deviation is computed from the diagonalised covariance matrix. This is done  $10^4$  times to provide a good balance between robustness of the error estimates and computational speed. We recompute all the relevant FIR properties for each realisation of our routine. From resultant distributions we then define our lower and upper uncertainty as the 16th and 84th percentile confidence interval respectively. However, given the fact that only a single solution with a single coefficient is considered in the IR, the final uncertainty on the FIR properties is underestimated.

We therefore also consider the observational uncertainty, that is primarily driven by the quality of the photometric data. We compute it by considering all possible solutions from our template library which fall within the 68% confidence interval range of the best-fit. This would correspond to a region where the solutions fall within  $\Delta\chi_{\nu}^2 = 1$ , where  $\Delta\chi_{\nu}^2 = \chi_{\nu,i}^2 - \chi_{\nu,\text{best}}^2$ , since

<sup>4</sup> Tested on a i9-8950HK CPU.

<sup>5</sup> It is also possible to manually define a rectangular filter at a desired wavelength, for cases where the filter transmission curve is not easily obtainable, e.g. ALMA.

<sup>6</sup> In this work we use terms  $L_{\text{IR}}$  and  $L_{\text{IR,total}}$  interchangeably.

<sup>7</sup> The quality of the photometry in this work does not allow us to distinguish bolometric AGN contributions below  $\sim 0.5\%$ , and thus the non-zero entries below that threshold are treated here as zero.



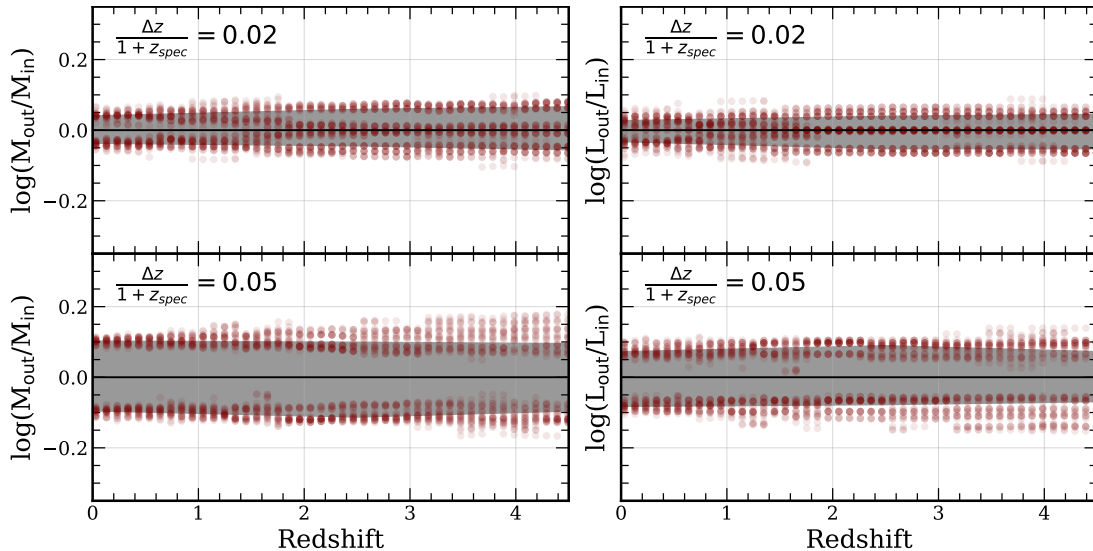


**Figure 4.** Effect of the  $z_{\text{phot}}$  uncertainty in the derivation of  $M_{\text{dust}}$  (left panel) and  $L_{\text{IR}}$  (right panel) assuming  $\epsilon = 0.02$  (top) and  $\epsilon = 0.05$  (bottom). Red circles represent the ratio of the output to input quantities from our simulations, as inferred by shifting the fitted redshift by  $\pm\Delta z$ . The shaded regions cover the 68% confidence interval and the solid black line indicates a ratio equal to unity.

the non-diagonal terms of the template covariance matrix are not zero<sup>8</sup>. We show these as red shaded areas on the bottom panel of Figure 3. The observational uncertainty is then derived as simply the width of the shaded region.

The final errors are computed as a quadrature sum of the linear combination uncertainty and the observational uncertainty.

### 3.5. The Effect of Photometric Redshift Uncertainty

To explore and quantify how the uncertainty in  $z_{\text{phot}}$  propagates into the estimates of  $L_{\text{IR}}$  and  $M_{\text{dust}}$ , we built mock IR SEDs of 1,200 galaxies utilising a suite of  $0.1 < U_{\text{min}} < 50$  DL07 models and place them uniformly in the  $0.03 < z_{\text{true}} < 5$  redshift range. Thus, each mock SED is characterised by a set of pre-defined  $L_{\text{IR,in}}$ ,  $M_{\text{dust,in}}$ , and  $z_{\text{true}}$  values. We then infer synthetic broad-band photometry in all IR bands available in *SDC2* (24-1100  $\mu\text{m}$ ) for each simulated galaxy. Since we are interested in the effect of the  $z_{\text{phot}}$  uncertainty on the derived FIR properties, to minimize any other possible sources of error (e.g. photometric uncertainty, poor photometric sampling of the SED) we adopt  $S/N = 5$  in all bands and add to our photometric data set the monochromatic flux density of the template at 2.2 mm. We then fit the synthetic photometry of each galaxy by

fixing the redshift first to  $z_- = z_{\text{true}} - \Delta z$ , and then to  $z_+ = z_{\text{true}} + \Delta z$  where  $\Delta z = \epsilon (1 + z_{\text{true}})$ . For our purposes, and based on the  $z_{\text{phot}}$  accuracy of the COSMOS field ( $\epsilon = 0.005 - 0.03$  as quantified in L16) we first adopt  $\epsilon = 0.02$  and then repeat the analysis for an even more conservative case with  $\epsilon = 0.05$ . The comparison between the extracted  $L_{\text{IR,out}}$  and  $M_{\text{dust,out}}$  to the input values for each simulation is presented in Figure 4.

Our analysis suggests that the effects  $\Delta z$  has in the derivation of the FIR properties is not negligible, even for the idealised case of detailed (24  $\mu\text{m} - 2.2$  mm) and high quality ( $S/N = 5$ ) photometric coverage. Indeed, we find that a typical value of  $\epsilon = 0.02$  ( $\epsilon = 0.05$ ), introduces an extra scatter of  $\sim 12\%$  (25%) and  $\sim 17\%$  (35%) in the derived  $L_{\text{IR}}$  and  $M_{\text{dust}}$ , that remains rather constant with redshift (at least out to  $z = 4$ ). At the same time, we also find that a symmetric  $\Delta z$ , as the one adopted in our simulations, does not inflict a noticeable systematic offset in the extracted FIR quantities ( $< 0.05$  dex).

Based on these results we update the uncertainties of the inferred FIR properties of our  $z_{\text{phot}}$ -sample ( $\text{ztype}=0$ , see Table 3) by adding in quadrature the extra error arising from a symmetric  $\Delta z$  (assuming  $\epsilon = 0.02$  for all sources) to the error budget inferred by the SED fitting procedure (photometry+model). While our correction is based on an average value of  $\epsilon = 0.02$ , we note that for catastrophic  $z_{\text{phot}}$  failures ( $\epsilon \sim 0.15$ ) we find a systematic offset of  $\leq 30\%$  between the input

<sup>8</sup> See sections 15.1 and 15.6 of Press et al. (1986) and Avni (1976). Note that  $\Delta\chi^2_{\nu} = 1$  only applies when marginalised over all other parameters.

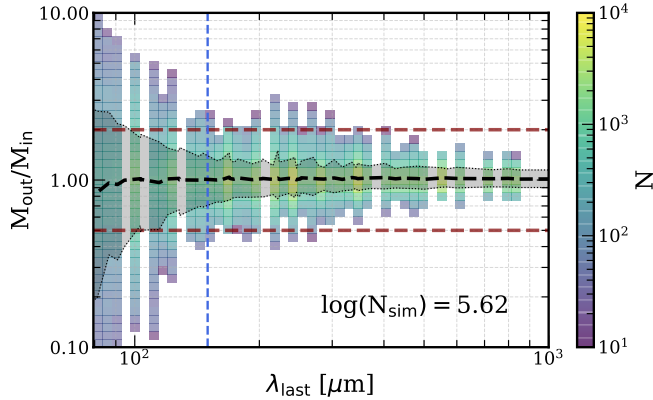


**Figure 5.** Accuracy of the inferred  $M_{\text{dust}}$  estimates as a function of (rest-frame)  $\lambda_{\text{last}}$ , parametrised by the ratio of the output to input  $M_{\text{dust}}$  in our simulations. The colour coding illustrates the density of the data points. The dashed black line and the shaded grey area denote the median and the 16<sup>th</sup> and 84<sup>th</sup> percentile confidence intervals respectively. The dashed maroon lines represent the value where the  $M_{\text{dust}}$  ratio is 0.5 and 2. The vertical blue line at  $150 \mu\text{m}$  denotes the  $\lambda_{\text{last}}$  onwards where for  $\geq 68\%$  of the simulated galaxies the accuracy of the recovered  $M_{\text{dust}}$  is  $\geq 70\%$ . The quantisation along the x axis is a consequence of the step-size in redshift, alongside with the available observed bands.

vs output  $M_{\text{dust}}$ , while the  $L_{\text{IR}}$  ratios remain uniformly scattered around unity.

#### 4. COMPLETENESS AND SYSTEMATICS

By construction, the photometric catalogues considered in this work combine observations that span  $\sim 4$  orders of magnitude in wavelength range, have different sensitivity limits and are differently affected by source blending and confusion. The fact that we choose to draw our sample based on the criteria described in section Section 2, rather than selecting galaxies detected in a single band (i.e. a flux limited sample), necessitates a series of simulations in order to quantify possible biases, systematic effects, as well as the completeness of our sample in terms of  $M_{\text{dust}}$  and  $L_{\text{IR}}$ .

##### 4.1. The effect of $\lambda_{\text{last}}$ Cutoff

It has been well established that for a robust modelling of the  $M_{\text{dust}}$ , at least one photometric data point longwards of the FIR peak, i.e. into the R-J tail of the SED, is necessary (e.g. Draine et al. 2007; Magdis et al. 2012a; Berta et al. 2016; Scoville et al. 2017). Here, we attempt to quantify how the accuracy of the derived  $M_{\text{dust}}$  estimates varies as a function of the rest-frame wavelength of the last available detection in conjunction with the selection criteria of our sample (i.e. at least

3 detections at  $24 \mu\text{m} < \lambda \leq 1200 \mu\text{m}$ ). For this, we perform the following simulations.

We start by building mock IR SEDs of fixed  $M_{\text{dust}}$  and  $L_{\text{IR}}$ , with  $0.1 < U_{\text{min}} \leq 50$ ,  $0 \leq \gamma \leq 0.5$  and  $q_{\text{PAH}} = 2.8\%$ , using the DL07 library and place them at  $0.01 \leq z \leq 4.5$  with a step of  $\Delta z = 0.05$ . After all of the models are created, synthetic photometry is performed by convolving each mock redshifted SED with a filter transmission curve. We consider all filters redder than MIPS  $24 \mu\text{m}$  available in SDC2, for a total of 9 bands and set all recovered fluxes to a  $S/N=3$  significance level. At each redshift the algorithm calculates the rest-frame wavelength for each available band, producing a grid of possible rest-frame wavelengths of the last detection ( $\lambda_{\text{last}}$ ) after accounting for our selection criterion that requests the availability (and the detection) in at least two bluer bands. For each  $\lambda_{\text{last}}$  it then randomly selects two additional bands bluewards of  $\lambda_{\text{last}}$ , producing a final set of three photometric data points. We then fit each set, and 50 permutations by varying the original fluxes by 10 %, with our code to extract  $M_{\text{dust}}$  and  $L_{\text{IR}}$  estimates. This procedure is then repeated for all mock SEDs and all acceptable values of  $\lambda_{\text{last}}$  in each redshift.

The accuracy with which we can recover  $M_{\text{dust}}$  estimates for each  $\lambda_{\text{last}}$  is then quantified by the scatter of the output to input  $M_{\text{dust}}$  ratio presented in Figure 5. As expected, we find a decreasing scatter in  $M_{\text{dust,out}}/M_{\text{dust,in}}$  at longer  $\lambda_{\text{last}}$ , that drops from a factor of  $\sim 2$  (for 68% of the simulated galaxies) at  $\lambda_{\text{last}} = 100 \mu\text{m}$  to a factor of  $\sim 1.1$  at  $\lambda_{\text{last}} = 400 \mu\text{m}$ .

Based on these results, we choose to define the subsample of ‘ $M_{\text{dust-robust}}$ ’ galaxies, for which at least one detection at  $\lambda_{\text{last}} \geq 150 \mu\text{m}$  is available. This threshold was chosen as an optimal compromise between the number of the rejected sources and the precision of the derived  $M_{\text{dust}}$  that for  $\lambda_{\text{last}} \geq 150 \mu\text{m}$  is  $\geq 70\%$ . Indeed, while  $\lambda_{\text{last}} \geq 150 \mu\text{m}$  is evidently not deep into the R-J, it seems that the addition of the two extra data points blueward of  $\lambda_{\text{rest}} = 150 \mu\text{m}$  are adequate to anchor the general shape, and eventually the  $M_{\text{dust}}$ , of the templates.

As a sanity check for the effectiveness of our criterion, we cross match the ‘ $M_{\text{dust-robust}}$ ’ sample with the A3COSMOS ALMA photometric catalogue presented in Liu et al. 2019a and refit the 233 galaxies that we find in common, adding this time the extra ALMA data point to the input photometry. The comparison of the inferred  $M_{\text{dust,A3}}$  to our  $M_{\text{dust}}$  estimates yields a very good agreement between the two estimates with a median  $\log(M_{\text{dust,A3}}/M_{\text{dust}}) \approx -0.04 \pm 0.06$ , further supporting our analysis. Nevertheless, we do identify a handful of sources for which the addition of the ALMA data

point results in lower  $M_{\text{dust}}$  estimates by a factor of  $\geq 3$ . An inspection of the SEDs of these extreme outliers reveals that the discrepancy originates either from possible catastrophic blending of the SPIRE 500  $\mu\text{m}$  photometry or alternatively from over-resolved ALMA photometry<sup>9</sup>.

The emerging ‘ $M_{\text{dust-robust}}$ ’ sample consists of 3,312 sources drawn from the same  $M_*$  and redshift distributions as the originally 4,991 selected galaxies. Finally, we note that our simulations operate under the assumption that the DL07 models are a good representation for the FIR emission of the real galaxies. Variations in dust composition, dust emissivity and dust absorption coefficients that could result in systematic offsets in the inferred  $M_{\text{dust}}$  (e.g. Magdis et al. 2012a; Dale et al. 2012; Berta et al. 2016; Scoville et al. 2017) cannot be modelled with our approach. As is the case for any other  $M_{\text{dust}}$  analysis - the relative rather than the face value estimates bare more physical significance.

#### 4.2. Limiting $M_{\text{dust}}$ and $L_{\text{IR}}$

We now attempt to compute the completeness threshold of our sample in terms of  $M_{\text{dust}}$  and  $L_{\text{IR}}$  as a function of redshift. Again, we build a grid of mock IR SED in the  $z = 0 - 5$  range using the same approach as described above. However, instead of considering the full range of possible  $\langle U \rangle \propto L_{\text{IR}}/M_{\text{dust}}$  values of the DL07 models, the constructed templates this time follow the  $\langle U \rangle - z$  relation of MS galaxies presented in Béthermin et al. (2015). At each redshift we then create a grid of templates normalised to  $\log(M_{\text{dust}}/M_{\odot}) = 6 - 10$  in steps of 0.1.

As before, the templates are used to produce synthetic photometry for each template in all bands available in the SDC2 catalogue. For each band we then adopt an rms based on the depth of the corresponding survey at each wavelength in the COSMOS field (Jin et al. 2018), and impose the same selection criteria to the mock photometry as those applied to the real catalogues. Following Section 4.1 we also request that the simulated sources have  $\lambda_{\text{last}} \geq 150 \mu\text{m}$ . If a galaxy of given  $M_{\text{dust}}$  fulfils these criteria at a given redshift, the algorithm moves to a lower  $M_{\text{dust}}$  until the object is rejected by our selection. By following these steps at different redshifts we thus obtain a limiting  $M_{\text{dust}}$  as a function of  $z$ , that we coin  $\text{lim}(M_{\text{dust}})(z)$ . In the process we also consider the scatter of the  $\langle U \rangle - z$  relation of Béthermin et al. 2015, in order to account for the variation of  $\langle U \rangle$

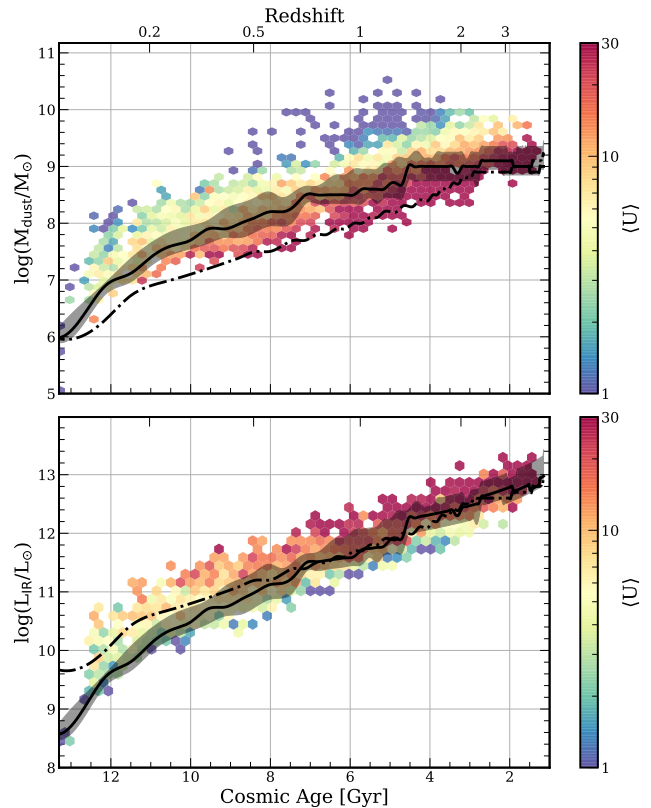


**Figure 6.** Simulated evolution of the  $\text{lim}(M_{\text{dust}})(z)$  (top) and  $\text{lim}(L_{\text{IR}})(z)$  (bottom), as described in Section 4.2. The black line represents the derived trend for MS galaxies and the dashed-dotted line shows the same relations for SBs ( $\langle U \rangle \sim 40$ ). The shaded regions define the 16<sup>th</sup> and 84<sup>th</sup> percentile confidence intervals, based on the scatter of the  $\langle U \rangle - z$  relation from Béthermin et al. (2015). The hexagonal bins contain the inferred parameters of the ‘ $M_{\text{dust-robust}}$ ’ sample (i.e. at least one detection at  $\lambda \geq 150 \mu\text{m}$ ), colour coded by mean radiation field intensity  $\langle U \rangle$ .

among MS galaxies at a given redshift. The derived  $\text{lim}(M_{\text{dust}})(z)$  can then be converted to  $\text{lim}(L_{\text{IR}})(z)$ , via:

$$\langle U \rangle = \frac{L_{\text{IR,DL07}}}{125 M_{\text{dust}}}, \quad (1)$$

as described in Draine & Li (2007).

We also repeat our simulation for SBs, by fixing  $\langle U \rangle = 40$  (e.g. Magdis et al. 2012a; Tan et al. 2014; Béthermin et al. 2015). We note however that the  $\langle U \rangle$  of SBs can vary substantially to lower or higher values (e.g. Magdis et al. 2012a, 2017; Schreiber et al. 2018; Jin et al. 2019; Cortzen et al. 2020). Therefore, the chosen  $\langle U \rangle = 40$  is only representative, but not necessarily unique. Nevertheless,  $\langle U \rangle < 40$  templates are represented in the simulation of the MS galaxies while galaxies with  $\langle U \rangle > 40$  are rather rare.

<sup>9</sup> The SEDs of the most extreme outliers can be retrieved here [https://github.com/VasilyKokorev/sdc\\_ir\\_properties/](https://github.com/VasilyKokorev/sdc_ir_properties/).

**Table 1.** Properties of the galaxy sample selected in Section 2. With the exception of redshift, the other quantities are derived via SED fitting. Values are presented as the median and a double sided 68% confidence interval.

	#	$z$	$L_{\text{IR},\text{total}}^a$	$L_{\text{IR},\text{DL07}}^b$	SFR <sup>c</sup>	$M_{\text{dust}}$	$M_*$ <sup>d</sup>	$f_{\text{AGN}}$	$\langle U \rangle$
	Galaxies		[ $10^{12} L_{\odot}$ ]	[ $10^{12} L_{\odot}$ ]	[ $M_{\odot} \text{ yr}^{-1}$ ]	[ $10^8 M_{\odot}$ ]	[ $10^{10} M_{\odot}$ ]	[%]	
COSMOS	4,406	$0.88^{+1.09}_{-0.57}$	$0.45^{+2.17}_{-0.40}$	$0.44^{+2.10}_{-0.39}$	$43.96^{+209.93}_{-38.88}$	$2.73^{+16.66}_{-2.08}$	$4.17^{+5.83}_{-2.89}$	$0.86^{+2.44}_{-0.60}$	$10.12^{+29.55}_{-7.72}$
GOODS-N	585	$1.01^{+1.02}_{-0.53}$	$0.35^{+1.60}_{-0.28}$	$0.34^{+1.53}_{-0.27}$	$33.84^{+152.74}_{-27.02}$	$2.60^{+10.34}_{-1.76}$	$3.56^{+6.03}_{-2.32}$	$2.60^{+4.74}_{-2.14}$	$9.38^{+29.82}_{-6.95}$
All	4,991	$0.90^{+1.08}_{-0.58}$	$0.44^{+2.09}_{-0.38}$	$0.42^{+2.04}_{-0.37}$	$42.30^{+203.88}_{-37.06}$	$2.71^{+15.71}_{-2.04}$	$4.07^{+5.93}_{-2.72}$	$0.93^{+3.06}_{-0.67}$	$10.00^{+29.68}_{-7.58}$

<sup>a</sup> Computed over a linear combination of AGN+DL07 best fit templates.

<sup>b</sup> Only considering the best fit DL07 template.

<sup>c</sup> Computed from  $L_{\text{IR},\text{DL07}}$ .

<sup>d</sup> Taken from the parent catalogue.

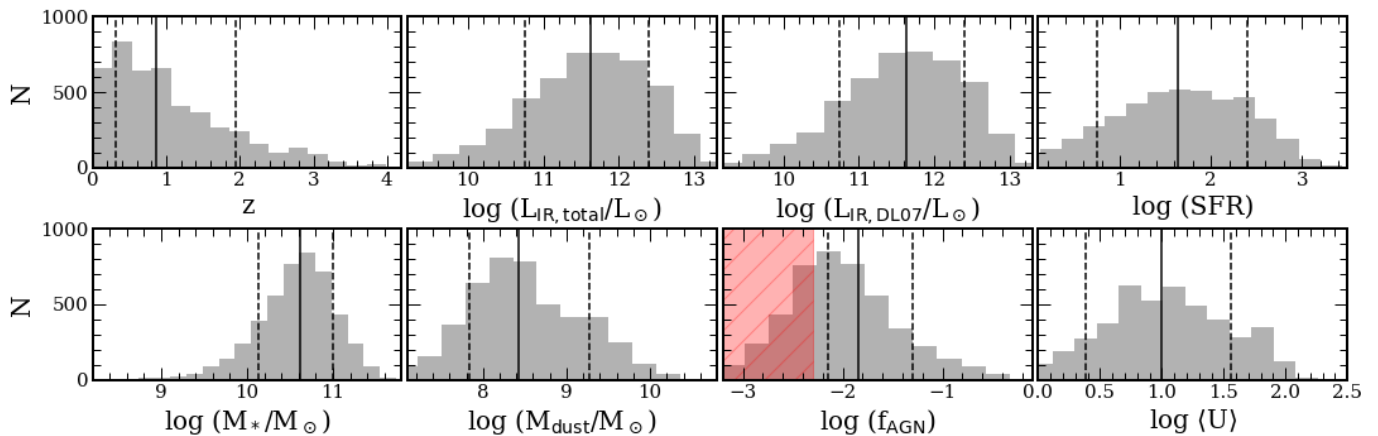


**Figure 7.** Distribution of the inferred IR properties of the COSMOS and GOODS-N samples. With the exception of  $z$  and  $M_*$ , these properties are the output of our SED fitting code (see Section 3). The solid black and dashed lines represent the median and the 68% confidence interval respectively. The hatched red region on the  $f_{\text{AGN}}$  histogram highlights the range where estimates are not reliable (i.e.,  $f_{\text{AGN}} < 0.005$ ).

The results of our simulations are presented in Figure 6, where we show the derived  $M_{\text{dust}}$  and  $L_{\text{IR}}$  as a function of  $z$  for the whole sample, along with the evolution of  $\text{lim}(M_{\text{dust}})$  and  $\text{lim}(L_{\text{IR}})$ . We see that the limiting  $M_{\text{dust}}$  increases towards high- $z$ , peaking at  $z \sim 2$  and remains flat afterwards, signifying that the balance between cosmological dimming and negative K - correction is achieved beyond that point. Following the black line we could infer the  $M_{\text{dust}}$  threshold above which our sample should be 100 % complete, assuming an MS-like population of galaxies. However, since our sample is not limited to MS galaxies we naturally also find sources that fall below our limiting  $M_{\text{dust}}$  track. As we will discuss later, these are predominately starbursting galaxies that exhibit elevated  $\langle U \rangle$  with respect to the MS. Our

secondary  $\text{lim}(M_{\text{dust}})$  trend for an SB-like population displays that with the SDC2 detection limits it is possible to detect a low  $M_{\text{dust}}$  object only if it is also a starburst.

We also find a similar trend for MS galaxies when considering the evolution of  $\text{lim}(L_{\text{IR}})$ . In this case, however we do not observe a flattening at  $z \sim 2$  and the trend continues to rise into the early Universe. The balance between cosmological dimming and the negative K - correction is not being achieved here, since the wavelengths that are required to reliably constrain the  $L_{\text{IR}}$  are positioned to the left of the FIR peak.

Admittedly, depths of FIR surveys are not the only limiting factors of sample selection. A requirement to have a photometric redshift and  $M_*$ , would mean that



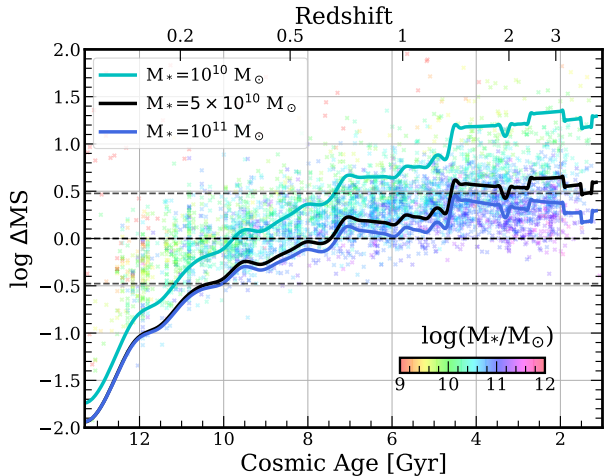


**Figure 8.** Position of our sources with respect to the MS as a function of cosmic age and redshift. Points are colour coded according to the  $M_*$ . The dashed black and gray lines denote the MS and its 0.5 dex scatter. The solid coloured lines correspond to the  $\Delta\text{MS}$  detection limit as computed based on the inferred  $\text{lim}(L_{\text{IR}})$  (see Section 4.2), and assuming  $M_* = 10^{10}$ ,  $5 \times 10^{10}$  and  $10^{11} M_\odot$ .

the optical photometry has to be sufficiently sampled, to allow such an analysis. Moreover, the deblending procedure itself goes through various selection stages, including both brightness and mass cuts. Various IR studies (Wang et al. 2016; Franco et al. 2018) have revealed substantial populations of optically dark sources at  $2 < z < 4$ , that are otherwise bright in IRAC and FIR bands, which would be unintentionally excluded from our analysis. Moreover, even at low- $z$ , objects that are faint in the  $K$ -band would also be missed. Indeed, a combination of these factors creates significant obstacles in our completeness analysis, we address this in more detail in Section 6.2.

## 5. FAR-INFRARED PROPERTIES OF GOODS-N AND COSMOS GALAXIES

Using our newly developed code presented in Section 3, we extract the FIR and UV-optical properties for all 4,991 galaxies from the SDC1 and SDC2 that meet our selection criteria as listed in Section 2. Moreover, since both input catalogues contain  $M_*$  estimates provided by either LePhare, EAZY or FAST, we are able to carry out a comparison of these  $M_*$  to the ones derived by Stardust. We find that the stellar masses are consistent with one another and direct the reader to Appendix B for a more detailed comparison between the two methods, as well as to EAZY derived  $M_*$ . Despite the similarities between the available and derived  $M_*$ , in our subsequent analysis we will utilise the  $M_*$  from the

parent catalogue, unless it is specified otherwise. This is done to preserve the original mass cuts described in Liu et al. (2018) and Jin et al. (2018), and therefore the mass completeness and homogeneity of the catalogue.

In total, out of 4,991 sources, we find 21 that we consider to be catastrophic fits ( $\chi^2_\nu > 100$ ), these only comprise 0.4 % of the entire output catalogue and are subsequently removed. The average  $\chi^2$  per degree of freedom of the entire dataset was computed to be equal to 0.98. The distribution of the FIR properties of the whole sample, their medians and associated uncertainties are presented in Figure 7 and summarised in Table 1. The catalogue containing the extracted FIR properties is described in the Appendix and is publicly available along with the best fit SED for each object.

We also calculate the position of the galaxies in our sample with respect to the MS, by converting the AGN-free  $L_{\text{IR,DL07}}$  estimates to SFR (Kennicutt 1998) and using the functional form of the main-sequence as presented in Schreiber et al. (2015), accounting for the fact that they use a Salpeter (1955) IMF. The distribution of  $\Delta\text{MS} = \text{SFR}/\text{SFR}_{\text{MS}}$  as a function of redshift and stellar mass is presented in Figure 8. We define the boundary between the star-forming and quiescent galaxies at  $\log\Delta\text{MS} = -0.5$  dex and between MS and SBs at  $\log\Delta\text{MS} = 0.5$  dex, which in linear space corresponds to  $\times 3$  below/above the MS. Quite naturally, for decreasing  $M_*$  and increasing redshift, our sample is progressively restricted to galaxies that lie above the MS. This is shown by the tracks in Figure 8 that indicate the limiting  $\Delta\text{MS}$  for fixed  $M_*$  as a function of redshift that is reached by our data, after converting the inferred  $\text{lim}(L_{\text{IR}})$  to  $\text{lim}(\text{SFR})$ . Nevertheless, we find that the majority of our sources are classified as MS galaxies (69%), with the remaining objects either considered to be undergoing a phase of ‘bursty’ star-formation (26%) or being passive galaxies (5%).

As a final sanity check we additionally fit the same sources with CIGALE, by utilising DL07 models and similar sets of optical and AGN templates. We find that the output parameters as derived from the two codes are in good agreement and defer the reader to Appendix C for a more detailed comparison.

### 5.1. The ‘ $M_{\text{dust-robust}}$ ’ Sample

We now focus on the FIR properties of the ‘ $M_{\text{dust-robust}}$ ’ galaxies described in Section 4.1, that should represent the most reliable sample for the exploration of the dependency of the  $L_{\text{IR}}$ ,  $M_{\text{dust}}$ , and  $\langle U \rangle$  on redshift, cosmic age, and  $\Delta\text{MS}$ . The emerging results are presented in Figure 9, where for completeness and to fa-

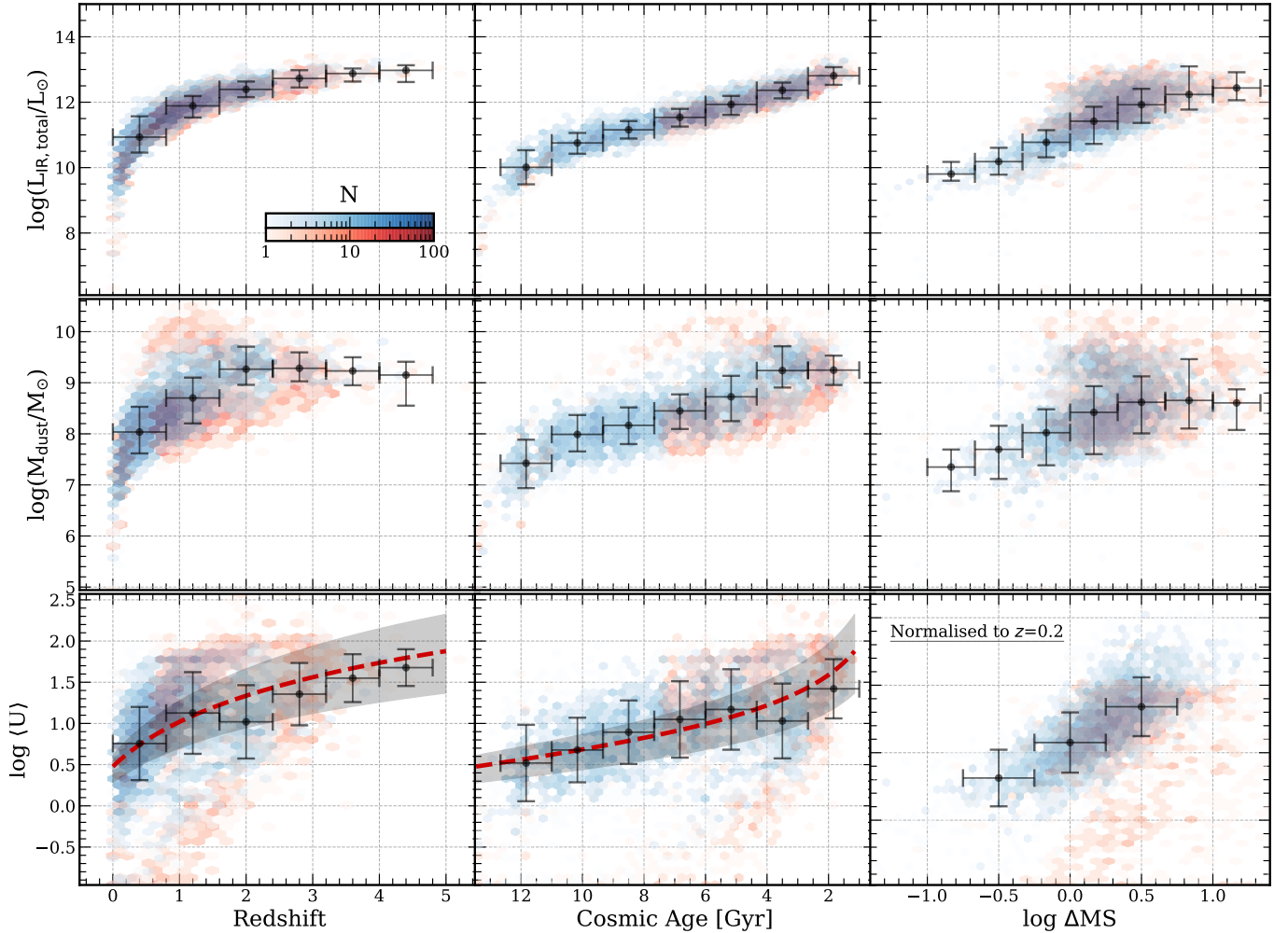


**Figure 9.** Evolution of general FIR properties, as computed with *Stardust*, as a function of  $z$ , cosmic age and  $\Delta\text{MS}$ . The hexagonal bins are normalised by the number count, and contain the ‘ $M_{\text{dust-robust}}$ ’ sample in blue, and the objects that were removed after the quality cut in red. For the ‘ $M_{\text{dust-robust}}$ ’ we show the binned median points, with their  $y$ -uncertainty corresponding to the 16<sup>th</sup> and 84<sup>th</sup> percentile intervals and  $x$ -uncertainty to the bin width. The dashed red lines and shaded regions correspond to the  $\langle U \rangle - z$  relation for MS galaxies from Béthermin et al. (2015).

facilitate comparisons, we also include the inferred properties of the full sample.

Both  $L_{\text{IR}}$  and  $M_{\text{dust}}$  are found to increase smoothly as a function of  $\Delta\text{MS}$ . At the same time, we also find that for MS galaxies  $\langle U \rangle$  evolves as  $(3.2 \pm 1.3) \times (1+z)^{1.2 \pm 0.3}$ , which is in excellent agreement with the stacking analysis of Béthermin et al. (2015). The fact that our individually detected galaxies appear to follow the same  $\langle U \rangle - z$  relation as the much deeper stacked ensembles, reinforces the notion that the adopted ‘ $M_{\text{dust-robust}}$ ’ sub-sample does not introduce a significant bias towards colder objects.

Since  $\langle U \rangle$  is proportional to  $L_{\text{IR,DL07}}/M_{\text{dust}}$ , and also a proxy for  $T_{\text{d}}$ , our analysis provides further evidence that dust in MS galaxies becomes warmer to-

wards higher redshifts, a trend that has already been recovered in previous studies (most of them based on stacking analysis, see e.g. Magnelli et al. 2014; Schreiber et al. 2015; Davidzon et al. 2018). Similarly, our data also confirm a progressive increase of  $\langle U \rangle$  (or  $T_{\text{dust}}$ ) with an increasing elevation above the MS (e.g. Magdis et al. 2017; Jin et al. 2019).

It is worth noticing that the full sample follows the same general trends albeit with a considerably larger scatter ( $\sim \times 2$ ) in  $M_{\text{dust}}$  and  $\langle U \rangle$ . The reduced scatter for the ‘ $M_{\text{dust-robust}}$ ’ sub-sample is driven by the imposed  $\lambda_{\text{last}} \geq 150 \mu\text{m}$  selection criteria that primarily removes the locus of sources with very cold fitting solutions ( $\langle U \rangle \lesssim 1$ ). We highlight that the rejection of these objects should not introduce a bias in our

sample since such low  $\langle U \rangle$  values are more indicative of poor photometric coverage/quality (lack of available data point in the R-J) rather than of realistic, extremely cold ISM conditions. However, we note that not all the extremely cold solutions have been removed from the ‘ $M_{\text{dust-robust}}$ ’ sample by our selection, as  $\sim 200$  objects with  $\langle U \rangle < 1$  meet our  $\lambda_{\text{last}} > 150 \mu\text{m}$  criterion. These can be easily identified in the  $\langle U \rangle - z$  plot and as the outliers populating the secondary blue cloud of points in the  $M_{\text{dust}} - \Delta\text{MS}$  plot in Figure 9. As we will discuss later, these could be sources with unreliable  $z_{\text{phot}}$  estimates, failures of the deblending in the SPIRE bands, or, more interestingly, gas giants or very compact galaxies with optically thick FIR emission.

### 5.2. Cold vs Warm Dust

The SED decomposition introduced in Section 3 can also provide constraints on the relative contribution of the warm (PDR,  $L_{\text{IR}}^{\text{warm}}$ ,  $M_{\text{dust}}^{\text{warm}}$ ) and cold (diffuse,  $L_{\text{IR}}^{\text{cold}}$ ,  $M_{\text{dust}}^{\text{cold}}$ ) ISM components to the total  $L_{\text{IR}}$  output and the total  $M_{\text{dust}}$  budget of the galaxies in our sample. In particular, it is worth investigating if and how the relative contribution of the components varies as a function of  $\Delta\text{MS}$ . Indeed, if SBs are experiencing elevated star-formation activity per surface area (Elbaz et al. 2011, 2018; Valentino et al. 2020) then one would expect to see an increased fraction of  $L_{\text{IR}}$  (and  $M_{\text{dust}}$ ) originating (and being heated) from the ‘PDR’ component, where the radiation intensity ranges from  $U_{\text{min}}$  to  $U_{\text{max}}$  (Draine & Li 2007).

In Figure 10 we plot the inferred properties of the warm and cold ISM components as a function of  $\Delta\text{MS}$ . We find that for a fixed  $L_{\text{IR}}$  (or equally SFR), SBs tend to have lower amounts of  $M_{\text{dust}}^{\text{cold}}$ , with  $M_{\text{dust}}^{\text{cold}}/L_{\text{IR}}$  showing a tight anti-correlation with  $\Delta\text{MS}$ . The same, however, does not apply to  $M_{\text{dust}}^{\text{warm}}/L_{\text{IR}}$ , which exhibits a significantly larger scatter and only a very weak dependence on  $\Delta\text{MS}$ . This is a consequence of an increasing fraction of warm to cold  $M_{\text{dust}}$  and  $L_{\text{IR}}$  between MS and SBs galaxies (Figure 10).

The observed trends suggest that compared to MS galaxies, SBs have a larger fraction of their total  $M_{\text{dust}}$  exposed to the intense stellar radiation fields of the PDRs, in agreement with expectations discussed above. Our result could indeed reflect an increase in the compactness of the star-formation activity for increasing distance from the MS as suggested in recent high resolution studies. Finally, under the assumption that  $M_{\text{dust}}^{\text{cold}}$  is proportional to  $M_{\text{gas}}$ , and  $L_{\text{IR}}$  is proportional to SFR, our results point to enhanced star-formation efficiencies and shorter gas depletion time scales for sources residing above the MS, as already reported in the literature

(e.g. Tacconi et al. 2010, 2020; Daddi et al. 2010; Magdis et al. 2012a, 2017; Sargent et al. 2014; Silverman et al. 2018).

## 6. DUST TO STELLAR MASS RELATION AND DUST MASS FUNCTIONS

As discussed in Section 1, constraints on the evolution of  $f_{\text{dust}}$  and the DMF are key towards a better understanding of dust production and destruction mechanisms at different epochs. Within this context, we explore how the current data set traces the evolution of  $f_{\text{dust}}$  and use it to characterise the DMFs at various redshifts.

### 6.1. The Evolution of the Dust Mass Fraction

To infer the evolution of  $f_{\text{dust}}$  we adopted the formula described in Liu et al. (2019b), which parametrises  $f_{\text{dust}}$  in terms of  $z$ ,  $M_*$  and  $\Delta\text{MS}$ . Compared to more simple log-space linear fitting models (e.g. Scoville et al. 2017), this formulation recovers trends that are more physically meaningful and also explores how these parameters are covariant and degenerate with each other in a multi-dimensional fitting space. As an initial check, we performed a Spearman correlation test and found  $M_{\text{dust}}$  to be mildly correlated with  $\log\Delta\text{MS}$  ( $\rho = 0.40$ ) and strongly correlated with  $M_*$  and  $t_{\text{age}}$  ( $\rho = 0.63$  and  $-0.80$  respectively). We consider the following functional form:

$$\begin{aligned} \log(f_{\text{dust}}) = & (a_0 + a_1 \log(M_*/10^{10} M_{\odot})) \log\Delta\text{MS} \\ & + b \log(M_*/10^{10} M_{\odot}) \\ & + (c_0 + c_1 \log(M_*/10^{10} M_{\odot})) t_{\text{age}}(z) \\ & + d \end{aligned} \quad (2)$$

where  $t_{\text{age}}$  is the cosmic age at a given redshift in Gyr and  $M_*$  is the stellar mass in  $M_{\odot}$ . For fitting we use the Python package - `scipy.optimize.curve_fit`, which finds the solution based on the least-squares method. We also consider how the extreme outliers can affect our results and thus only fit the medians in a given redshift bin. The best fit values are as follows:

$$\begin{aligned} a_0 &= -0.90 & a_1 &= 1.31 \\ b &= -0.98 & c_0 &= -0.23 \\ c_1 &= 0.11 & d &= -0.64, \end{aligned}$$

with the uncertainties being computed from the covariance matrix. We then used the functional form given by Equation 2 to re-normalise all galaxies to lie on the main sequence ( $\Delta\text{MS} = 1$ ), and  $M_* = 5 \times 10^{10} M_{\odot}$ , in order to directly compare with our best-fit function in 2 dimensions.

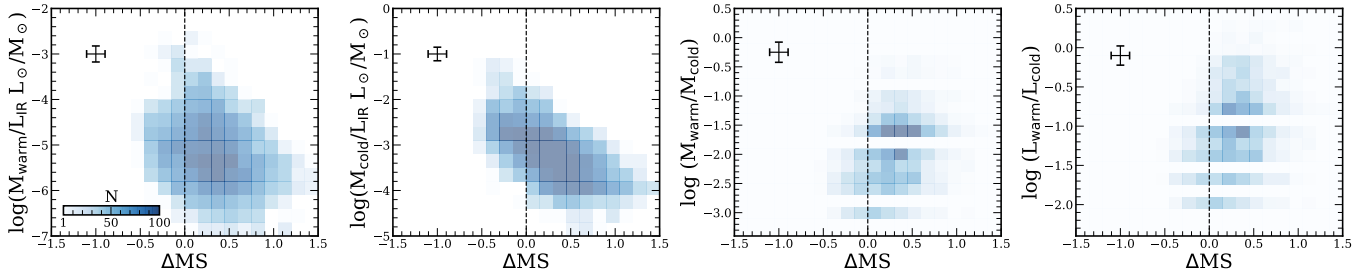


**Figure 10.** Comparison of the properties of the warm (PDR) and cold (diffuse) dust components of the ISM as a function of  $\Delta MS$ . From left to right the panels show the warm and cold dust mass components weighted by the total  $L_{IR}$ , the fraction of warm to cold  $M_{dust}$  and the fraction of ‘PDR’ to diffuse ISM IR output. The bins are coloured based on number density of the data points. We show a typical uncertainty on the plotted parameters in the top left corner of each panel.

The normalised data and the best fit relation presented in Figure 11 are in very good agreement with the collection of similar trends drawn from the literature (e.g. Scoville et al. 2017; Tacconi et al. 2018; Liu et al. 2019b; Magnelli et al. 2020). We note that any apparent discrepancies between the slope and the normalisation of our recovered relation to that of Scoville et al. (2017) and Magnelli et al. (2020) are driven by the model parametrisation, as for the latter the multi-variable functional forms do not consider the covariance between the fitted values.

In Figure 12 we also show how the one dimensional relation between  $M_{dust}$  and  $M_*$  compares to the multi-dimensional fit within six redshift bins. Since our analysis can be affected by the completeness of our sample in terms of  $M_*$  and  $M_{dust}$ , we also consider the underlying selection effects based on our  $\text{lim}(M_{dust})(z)$  derivation and assuming that our catalogue is complete at  $M_* > 10^{10} M_\odot$ . We find that for a fixed redshift range, the inferred  $M_{dust} - M_*$  relation shadows the multi-parameter fit up to  $z \sim 1.1$ , in moderate agreement with the trends reported in Liu et al. (2019b) and Magnelli et al. (2020). However, the increasing incompleteness and the low number statistics do not allow us to extend our analysis at higher redshifts.

Based on these results we will limit the subsequent DMF analysis to the  $0.2 < z < 1.1$  range.

### 6.2. Dust Mass Functions

After obtaining the functional form for  $f_{dust}(t_{age}, M_*, \Delta MS)$ , we are now in position to examine the shape and the evolution of the DMF with redshift. For this we will restrict our analysis to the COSMOS sample (SDC2), as we do not have enough statistics or coverage of the GOODS-N field to reliably constrain the DMF.

The ‘Super-Deblending’ procedure that went into producing the SDC2 catalogue creates a significant obstacle when attempting to consider all of the incompleteness

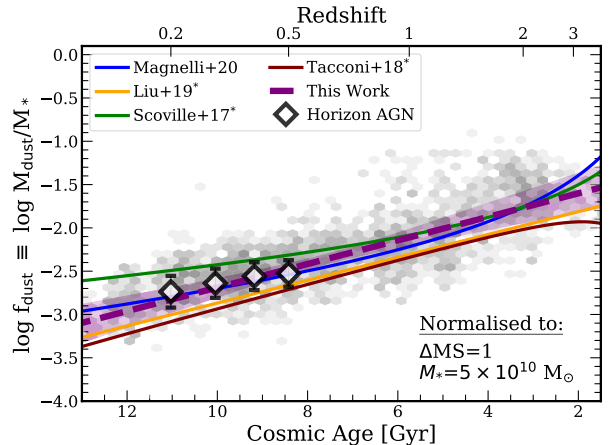


**Figure 11.** Derived relations for  $f_{dust}$  as a function of  $z/t_{age}$ . The dashed purple line shows the fit to our data, while solid coloured lines display literature results. The shaded purple region denotes the 16<sup>th</sup> and 84<sup>th</sup> percentile confidence intervals of our fit. Starred labels denote literature calculations where a direct comparison was not available and a  $\delta_{GDR} = 100$  was assumed. The grey hexbins contain the data from ‘ $M_{dust-robust}$ ’ sample, and are normalised by the number count. Both the data and the derived relations have been re-scaled to  $\Delta MS=1$  and  $M_* = 5 \times 10^{10} M_\odot$ . White diamonds show median positions of the Horizon AGN star-forming galaxies at that redshift, normalised in the same way as our data.

effects of the sample. The objects that end up in our sample go through several selection stages, both before and after the deblending procedure. These include both the brightness and mass cuts of the parent catalogue (Laigle et al. 2016), the availability of infrared coverage (Jin et al. 2018) and the selection criteria imposed in our study. As such, it is not possible to robustly assess the properties and the number of objects that end up being ‘lost’. Therefore, we select an alternative approach in computing the DMF for our objects, namely utilising the derived  $f_{dust}$  parametrisation along with



the available SMFs in the literature. Later in this section, we also attempt to account for the incompleteness effects and compare the SMF-derived DMF to the observed number density of galaxies per  $M_{\text{dust}}$  bin.

### 6.2.1. DMF from SMF

For our analysis we adopt the SMF computed by [Davidzon et al. \(2017\)](#), which covers the entire COSMOS field and the  $z = 0.2\text{--}4$  range. Their mass function already accounts for the Eddington bias, so we do not need to consider any additional corrections. Since the vast majority of galaxies in our sample are star-forming, we adopt the derived parameters for the ‘active’ SMF only.

The galaxy mass function is normally expressed as a Schechter function ([Schechter 1976](#)), which in logarithmic form can be written as:

$$\Phi(\log M)d(\log M) = \ln(10) \exp(-M/M^*) \times \Phi^*(-M/M^*)^{(\alpha+1)} d(\log M_*) \quad (3)$$

where  $\alpha$  is the slope of the faint-end,  $\Phi^*$  is the normalisation and  $M^*$  is the characteristic mass, indicating the position of the ‘knee’ of the Schechter function. To convert the SMF to DMF, we first postulate that the number of galaxies in a given redshift bin is the same, regardless of whether we integrate over  $M_*$  or  $M_{\text{dust}}$ , namely:

$$\int_0^\infty \Phi(\log M_*)d(\log M_*) = \int_0^\infty \Phi(\log M_{\text{dust}})d(\log M_{\text{dust}}),$$

the integrands can be re-arranged to obtain:

$$\Phi(\log M_{\text{dust}}) = \Phi(\log M_*)d(\log M_*)/d(\log M_{\text{dust}}).$$

We then differentiate [Equation 2](#), to obtain  $d(\log M_*)/d(\log M_{\text{dust}}) = (b + c_1 \times t_{\text{age}} + 1)^{-1}$ . In order to perform the final conversion we also transform all the  $M_*$  bins into  $M_{\text{dust}}$  bins, by inverting our formulation of  $f_{\text{dust}}$ , taken at  $\Delta\text{MS} = 1$ .

### 6.2.2. Accounting for the Eddington Bias

Before comparing to the real data it is important to note that, while calculating the SMF-derived DMF, the Eddington bias, induced by the  $f_{\text{dust}}$  scatter should be taken into account. Since we are directly employing the [Davidzon et al.](#) SMF, where the Eddington bias has already been corrected, using the best-fit  $f_{\text{dust}}$  relation to convert SMF to DMF will only reproduce the median trend and will not properly account for the full dynamic range of observed  $M_{\text{dust}}$ . To alleviate this, we rely on the work by [Loveday et al. \(1992\)](#), that showed that the Eddington bias manifests itself as a Gaussian, whose

width is equal to the scatter of the variable of interest, convolved to the mass function. We have thus utilised an approach similar to that used in [Davidzon et al. \(2017\)](#) for the SMF and [Beeston et al. \(2018\)](#) for the DMF, where they successfully deconvolve their observed mass functions by using the scatter of the observed variable. As such, within each redshift bin we consider the standard deviation of the  $f_{\text{dust}}$  in a logarithmic space. We then use this scatter to create a simple Gaussian that is centred at zero, and then convolve it with our SMF-derived DMF. This allows us to better take into account the scatter of our data, and thus produce a more realistic mass function. In conclusion, we have indirectly produced two versions of SMF-derived DMFs, with and without the scatter.

### 6.2.3. Comparison to the Observed Number Density

Now we would like to compare the SMF-derived DMF to the observed number density of galaxies in the ‘ $M_{\text{dust-robust}}$ ’ sample. To this end, we first apply the widely used non-parametric  $1/V_{\text{max}}$  method to correct for the Malmquist bias of our sample ([Schmidt 1968](#)). This method relies on assigning the  $V_{\text{max}}$  to each redshift bin, based on the detection limits of the survey. Effectively, this correction accounts for the fact that in a given volume, a brightness limited survey is more likely to pick up the bright sources, while missing faint galaxies, that would populate the low- $M_{\text{dust}}$  end. We explicitly highlight that the  $V_{\text{max}}$  correction only accounts for the FIR flux rms cuts, and not the selection criteria outlined in [Section 2.3](#).

To calculate the  $V_{\text{max}}$  we use the prescription from [Weigel et al. \(2016\)](#), which provides a volume correction for each individual source. As a first step, and for a given redshift bin, we split our sources into 0.4 dex bins in the  $\log(M_{\text{dust}}/M_{\odot}) = 6\text{--}11$  interval. Given that the median uncertainty on the  $M_{\text{dust}}$  is  $\sim 0.3$  dex, the following bin spacing will ensure that there is very little to no cross-contamination between mass bins. The  $V_{\text{max}, i}$ , where  $i$  denotes an individual galaxy, can be then calculated as:

$$V_{\text{max}} = \frac{A}{3} (d_c(z_{\text{max},i})^3 - d_c(z_{\text{min},i})^3), \quad (4)$$

where  $d_c$  is the comoving distance and  $A$  is the area, which in our case is equal to  $1.38 \text{ deg}^2$ . Following [Weigel et al. \(2016\)](#), the  $z_{\text{min},i}$  is given simply by the lower boundary of the bin. The  $z_{\text{max},i}$  on the other hand can be calculated empirically, either through detection limits of individual bands or by considering a limiting mass of the survey. It however cannot exceed the maximum redshift of the bin.

To obtain the  $z_{\text{max}}$ , we consider the best fit SEDs for our sources, and the rms of the parent catalogues in

order to redshift the sources to the point where they no longer fulfil our selection criteria as outlined in [Section 2](#). Using this method we however found that, for an overwhelming majority of sources, the computed  $z_{\max,i}$  exceeds the upper boundary of the bin they belong to. Therefore, the  $V_{\max}$  correction that we apply becomes effectively bound between the lower and the upper redshift of the bin. We find that this method works best in the lowest ( $0.2 < z < 0.5$ ) redshift bin, with the  $\langle V/V_{\max} \rangle$  test returning a value of 0.47. The remaining two redshift bins are significantly incomplete, with the ratio returning 0.83 and 1.38 respectively.

Among the other sources of incompleteness, as discussed in [Section 6.2](#), here we can attempt to account for lost sources due to the sensitivity limits of the survey and failures in the deblending procedure. We therefore multiply our points by the loss fraction in each redshift bin that is computed as the ratio between sources in our catalogue over the sources that have  $\text{SN-IR} > 1$ <sup>10</sup> in the parent catalogue. The SN-IR parameter, described in greater detail in [Liu et al. \(2018\)](#) and [Jin et al. \(2018\)](#), and references therein, considers a combination of FIR bands starting with  $100 \mu\text{m}$ . We thus expect that in this context, our SN-IR threshold can indicate whether a galaxy is intrinsically dusty.

The comparison of the SMF-derived DMF with and without the Eddington bias taken into account, along with the observed volume-weighted number density of galaxies, derived as described above, for three redshift bins, is presented in [Figure 13](#). We find that the DMF without the Eddington bias is insufficient to reproduce the observed dynamic range of  $M_{\text{dust}}$ , particularly in the higher redshift bins, exactly as we have predicted in [Section 6.2.2](#). On the other hand, the SMF-derived DMF with the artificially induced bias, through the  $f_{\text{dust}}$  scatter, is in good agreement with the data in the high-mass end, further highlighting the necessity of accounting for the observational biases when inferring relations (i.e.  $M_* - M_{\text{dust}}$  in our case) through the observed mass (or luminosity) functions. Although our model underpredicts the high-mass end data in the higher redshift bin, both still agree within the error bars. At the same time though, in the low-mass regime our data significantly underestimate the number density of galaxies mirroring the incompleteness of our sample in this  $M_{\text{dust}}$  regime. It is worth noticing though that the turnover of the observed data perfectly coincides with the independent estimates of  $\lim(M_{\text{dust}})$ , offering an indirect validation of our simulations presented in [Section 4.2](#). For the

analysis in the next sections, we adopt the SMF-derived DMF, which has the Eddington bias corrected out, as the final result against which we will compare previous observationally driven DMFs and theoretical predictions<sup>11</sup>.

## 7. GAS CONTENT OF STAR-FORMING GALAXIES

The inferred  $M_{\text{dust}}$  estimates can be used as an invaluable proxy of the gas mass ( $M_{\text{gas}}$ ). To this end, we adopt the metallicity dependent gas-to-dust mass ratio  $\delta_{\text{GDR}}$  technique, that takes advantage of the relatively tight anti-correlation between the gas-phase metallicity, and the  $\delta_{\text{GDR}}$  of galaxies, both in the local Universe and at high- $z$  (see e.g. [Leroy et al. 2011](#); [Magdis et al. 2012a](#); [Rémy-Ruyer et al. 2014](#); [Genzel et al. 2015](#)). For a source with known metallicity ( $Z$ ) and  $M_{\text{dust}}$ , one can estimate the amount of  $M_{\text{gas}}$  via the following relation:

$$M_{\text{gas}} = \delta_{\text{GDR}}(Z) M_{\text{dust}}, \quad (5)$$

where  $M_{\text{gas}}$  corresponds to  $M_{\text{H}_2} + M_{\text{HI}}$ , i.e. the sum of the atomic and molecular hydrogen.

Given the absence of direct metallicity measurements for our sample, we adopt the fundamental metallicity relation (FMR) of [Mannucci et al. \(2010\)](#). In particular, we use the  $M_*$  and SFR estimates as inputs to the FMR, and obtain metallicities calibrated for the [Kewley & Dopita \(2002\)](#) (KD02) photoionisation models. These metallicities are subsequently converted to the [Pettini & Pagel \(2004\)](#) (PP04 N2) scale following [Kewley & Ellison \(2008\)](#). We then estimate the  $\delta_{\text{GDR}}$  of each galaxy through the  $\delta_{\text{GDR}} - Z$  relation of [Magdis et al. \(2012a\)](#), given as:

$$\log(\delta_{\text{GDR}}) = (10.54 \pm 1.00) - [12 + \log(\text{O}/\text{H})]^{(0.99 \pm 0.12)} \quad (6)$$

and subsequently derive  $M_{\text{gas}}$  through [Equation 5](#), for all the sources in SDC1 and SDC2 catalogues. We propagate the uncertainties on  $M_{\text{gas}}$  by taking into account the uncertainty on  $M_{\text{dust}}$  and combining it with the typical scatter of 0.2 dex on the  $\delta_{\text{GDR}} - Z$  relation ([Magdis et al. 2012b](#)). These inferred  $M_{\text{gas}}$  estimates with associated uncertainties are included in the released catalogue.

### 7.1. Gas to Stellar Mass Relation

Similarly to  $f_{\text{dust}}$ , we also explore the dependence of  $f_{\text{gas}}$  on cosmic age,  $\Delta\text{MS}$  and  $M_*$ . We utilise the same multi-parameter fitting function as before (see [Equa-](#)

<sup>10</sup>  $\text{SN-IR}^2 = \sum_{\lambda} (\text{S}/\text{N})_{\lambda}^2$ , with  $\lambda \geq 100 \mu\text{m}$ .

<sup>11</sup> Tables containing the DMFs can be accessed here: [https://github.com/VasilyKokorev/sdc\\_ir\\_properties](https://github.com/VasilyKokorev/sdc_ir_properties).

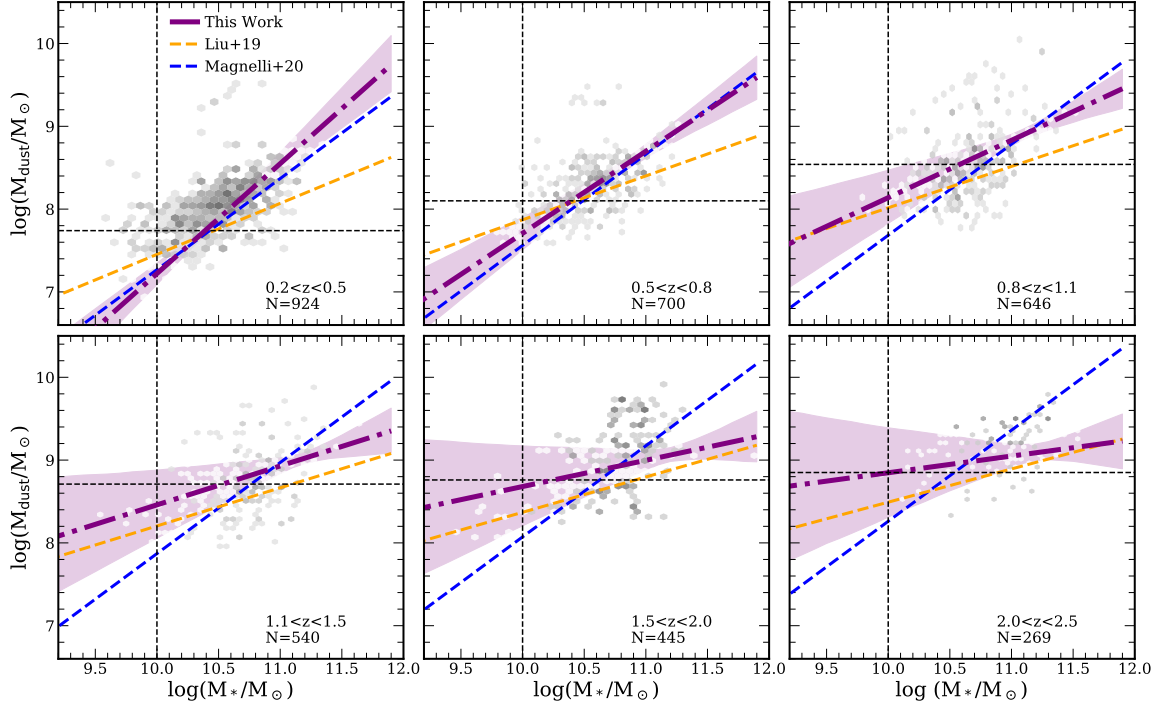


**Figure 12.**  $M_{\text{dust}}$  as a function of  $M_*$  in six redshift bins. The dashed-dotted purple line represents our best fit from Equation 2 that was collapsed to a single dimension, with  $\Delta\text{MS}=1$  and  $z = \langle z_{\text{bin}} \rangle$ . The shaded purple regions denote the 16<sup>th</sup> and 84<sup>th</sup> percentile confidence intervals of our fit. The orange and the blue lines show the relations derived in Liu et al. (2019b) and Magnelli et al. (2020), respectively. The dashed black lines represent the detection limits of the original catalogue, in  $M_*$  (vertical), and the  $\text{lim}(M_{\text{dust}})$  that we compute in Section 4.2 (horizontal).

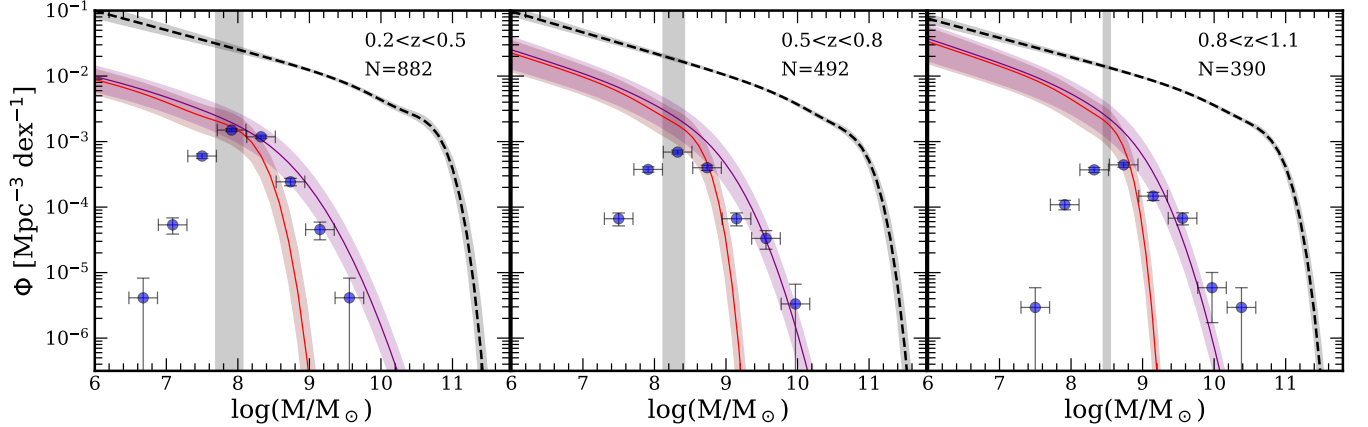


**Figure 13.** Derived DMFs in the  $0.2 < z < 0.5$ ,  $0.5 < z < 0.8$ , and  $0.8 < z < 1.1$  ranges. The dashed black line represents the original SMF for active galaxies from Davidzon et al. (2017). The purple and red lines are the DMFs obtained by converting the SMF, with and without the Eddington bias applied, respectively. The blue points are the DMF calculated directly from our data. The shaded rectangular area highlights the theoretical prediction for  $\text{lim}(M_{\text{dust}})$  in that redshift interval.

tion 2), and focus on the ‘ $M_{\text{dust-robust}}$ ’ sample. We calculate the Spearman rank correlation between our variables and find  $M_{\text{gas}}$  to be mildly correlated with  $\log\Delta\text{MS}$  and  $M_*$  ( $\rho = 0.47$  and  $0.53$  respectively) and strongly negatively correlated with  $t_{\text{age}}$  ( $\rho = -0.82$ ). The fitting procedure yields the following best-fit parameters:

$$\begin{aligned} a_0 &= -0.73 & a_1 &= 1.16 \\ b &= -1.02 & c_0 &= -0.20 \\ c_1 &= 0.09 & d &= 1.39. \end{aligned}$$

The best-fit  $f_{\text{dust}}-t_{\text{age}}$  (or redshift) relation along with our data, both normalised to  $\Delta\text{MS} = 1$  and  $M_* = 5 \times 10^{10} M_{\odot}$ , are presented in Figure 14 (top). Similar to previous studies (Scoville et al. 2017; Tacconi et al. 2018; Liu et al. 2019b; Magnelli et al. 2020), we find a sharp increase in the gas fraction up to  $z = 2$ , followed by a milder evolution at higher redshifts, a change that is noticeable only in the  $f_{\text{dust}}-z$  parameter space. We note however that due to poor statistics and lack of spectroscopic redshifts, our data cannot reliably constrain the high- $z$  evolution of  $f_{\text{gas}}$  at  $z > 2$ . We also detect a population of sources that display significantly elevated gas reservoirs for their redshift ( $\log(f_{\text{gas}}) > 0.5$ ). Some of those objects have either only a  $z_{\text{phot}}$  estimate available, or appear to be blended in the SPIRE bands and therefore could have an erroneously large  $M_{\text{dust}}$ , and subsequently  $M_{\text{gas}}$  estimate assigned to them. However, among these we do identify some sources with spectroscopic redshifts, that are also ‘clean’/isolated in the IR maps. In particular we find  $\sim 40$  such sources with  $\log(f_{\text{gas}}) > 0.5$  and six with  $\log(f_{\text{gas}}) > 1$  that, as we discuss later, we coin as ‘gas-giants’.

## 7.2. Evolution of Depletion Time

Finally, we focus our attention on the depletion time  $\tau_{\text{depl}} = M_{\text{gas}}/\text{SFR} = 1/\text{SFE}$ . We employ the same fitting technique as before, and explore the evolution of  $\tau_{\text{depl}}$  with cosmic age,  $\Delta\text{MS}$  and  $M_*$  in a multi-dimensional parameter space, for the ‘ $M_{\text{dust-robust}}$ ’ sample. The  $\tau_{\text{depl}}$  correlates mildly with age and  $\Delta\text{MS}$  (Spearman  $\rho = -0.46$  and  $-0.58$ , respectively) and weakly with  $M_*$  ( $\rho = -0.23$ ). The best fit parameters are as follows:

$$\begin{aligned} a_0 &= -1.65 & a_1 &= 1.42 \\ b &= -0.95 & c_0 &= -0.02 \\ c_1 &= 0.12 & d &= 0.37. \end{aligned}$$

We show the best-fit  $\tau_{\text{depl}}-t_{\text{age}}$  relation along with our data, both normalised to  $\Delta\text{MS} = 1$  and  $M_* = 5 \times 10^{10} M_{\odot}$ , are presented in Figure 14 (bottom). In line with the previous studies of  $\tau_{\text{depl}}$  by Scoville et al.

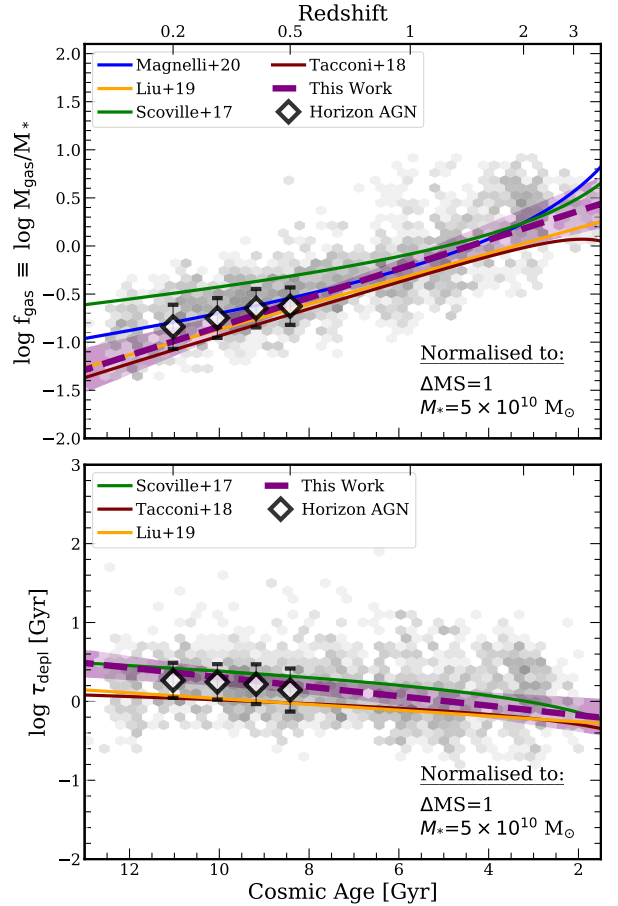


**Figure 14.** Derived relations for  $f_{\text{gas}}$  (top) and  $\tau_{\text{depl}}$  (bottom) as a function of  $z/t_{\text{age}}$ . The dashed purple line shows the fit to our data, while solid coloured lines display literature results. The shaded purple region denotes the 16<sup>th</sup> and 84<sup>th</sup> percentile confidence intervals of our fit. The grey hexbins contain the data from ‘ $M_{\text{dust-robust}}$ ’ sample, and are normalised by the number count. Both the data and the derived relations have been re-scaled to  $\Delta\text{MS}=1$  and  $M_* = 5 \times 10^{10} M_{\odot}$ . White diamonds show median positions of the Horizon AGN star-forming galaxies at that redshift, normalised in the same way as our data.

2017; Tacconi et al. 2018; Liu et al. 2019b, we recover a relatively weak decrease of depletion time (or increase in SFE) with redshift.

## 8. DISCUSSION

### 8.1. On the Dust and Gas Scaling Relations

The recovered trends between  $M_{\text{dust}}$ ,  $M_*$  and  $M_{\text{gas}}$  and their evolution with redshift offer a test-bed against which theoretical and previous observationally driven studies can be compared to. As shown in Figure 11 and Figure 14, our analysis yields  $f_{\text{dust}}$  and  $f_{\text{gas}}$  evolutionary tracks consistent with those presented in Tacconi et al.



(2018); Liu et al. (2019b) and to a smaller degree to those reported in Scoville et al. (2017); Magnelli et al. (2020). As discussed earlier, the mild tension between the latter works and our results could be primarily attributed to the choice of the fitting function.

The  $f_{\text{dust}}$  and  $f_{\text{gas}}$  in our sample of SFGs increase rapidly from  $z = 0$  to  $z = 1$ , peak around  $z \sim 2 - 3$ , and then remain roughly constant. It is however a point of contention whether the latter is driven by actual physical processes or is a consequence of the scarcity of data at  $z > 2$ . It is also worth mentioning that our analysis points towards a milder evolution of  $f_{\text{dust}}$  ( $-0.8$  dex) compared to  $f_{\text{gas}}$  ( $-1.3$  dex) from  $z = 2$  to  $z = 0$  with the latter dropping  $\sim 3\times$  faster. This is aligned with the evolution of  $\rho_{\text{dust}}$  and  $\rho_{\text{gas}}$  derived by the ALMA stacking analysis of Magnelli et al. (2020), and could in fact reflect the evolution of metallicity, and thus of  $\delta_{\text{GDR}}$ , for fixed  $M_*$  towards lower redshifts.

At the same time, the decrease of  $M_{\text{dust}}$  with decreasing redshift, for fixed  $M_*$ , can be attributed to either the destruction of dust grains by interstellar radiation fields, or their incorporation into the stellar population. This is discussed in more detail in Donevski et al. (2020), where they also report a decreasing  $f_{\text{dust}}$  from earlier cosmic age to the present epoch. We note that the observed trend could also mirror the overall decline in the SFRD in the Universe from  $z = 2$  to the present day, that points towards lower star-formation activity and thus lower dust production at later cosmic epochs. Finally, at a fixed redshift, both  $f_{\text{dust}}$  and  $f_{\text{gas}}$  decrease as a function of  $M_*$  (as indicated by a negative value of the fitting parameter  $b$ , see Equation 2), in line with previous studies (e.g. Magdis et al. 2012a; Magnelli et al. 2020 and references therein).

In addition to observational studies, we can also compare our results to theoretical predictions. To this end, we consider the Horizon AGN (HAGN) hydrodynamical simulations in the COSMOS field (Dubois et al. 2014; Laigle et al. 2019) and draw a sample of SFGs ( $\Delta\text{MS} > 0.3$ ) in the  $z = 0.2 - 0.5$  range, selected to meet the  $M_*$  completeness of the COSMOS 2015 survey and which fall within a simulation box of 143 Mpc per side (Dubois et al. 2014). To measure  $\Delta\text{MS}$  for each galaxy we considered the  $M_*$  and the 100 Myr averaged SFR from the simulations. Also, since  $M_{\text{dust}}$  is not an explicit parameter of HAGN galaxies, we used a constant  $\delta_{\text{GDR}} = 100$  to convert the  $M_{\text{gas}}$  values, as derived from the simulations, to  $M_{\text{dust}}$ . We then use the  $M_{\text{gas}}$ ,  $M_*$ , and  $M_{\text{dust}}$  of the simulated galaxies to infer  $f_{\text{gas}}$  and  $f_{\text{dust}}$ . The median values and their scatter, renormalised to MS ( $\Delta\text{MS} = 1$ ) and  $M_* = 5 \times 10^{10} M_{\odot}$  in four redshift bins, are presented and compared to the

real data in Figure 11 and Figure 14. We find a good agreement between the theoretical predictions and our observationally driven trends (in the  $0.2 < z < 0.5$  range at least) indicating that the HAGN simulation can successfully reproduce the baryonic components of the galaxies and its evolution with redshift. Conversely, the agreement of our results with both theoretical and observational studies, provides an extra indirect validation for the performance of our new SED fitting code.

## 8.2. On the Evolution of Depletion Time

As with  $f_{\text{dust}}$  and  $f_{\text{gas}}$ , our recovered trends, that connect  $\tau_{\text{depl}}$  to redshift,  $\Delta\text{MS}$  and  $M_*$ , show similar behaviour to the ones presented in Scoville et al. 2017, and to a lesser extent Tacconi et al. 2018; Liu et al. 2019b. The dependence of  $\tau_{\text{depl}}$  on  $M_*$  is relatively weak across all studies, however, similarly to Liu et al., we find that the depletion time for high-mass galaxies increases from early cosmic ages towards present times, while low-mass galaxies display an opposite trend of decreasing  $\tau_{\text{depl}}$  with cosmic age. As discussed in Liu et al. (2019b) and Hodge & da Cunha (2020), this could be a signature of downsizing, meaning that more massive galaxies evolve at earlier times.

During our analysis we find  $\tau_{\text{depl}} \sim (1+z)^{-1.07}$ , which is more reflective of the scaling relations derived in Scoville et al. (2017) ( $\tau_{\text{depl}} \sim (1+z)^{-1.04}$ ), rather than weaker dependencies ( $\tau_{\text{depl}} \sim (1+z)^{-0.62}$  and  $(1+z)^{-0.58}$ ) found by Tacconi et al. (2018) and Liu et al. (2019b) respectively. As expected, and in line with the literature results, we also find that galaxies above the MS (at a fixed  $M_*$  and  $z$ ), form stars with a much higher efficiency (lower  $\tau_{\text{depl}}$ ), than their MS counterparts, with  $\tau_{\text{depl}} \sim \Delta\text{MS}^{-1.68}$ . We would also like to caution the reader and highlight the fact that Tacconi et al. and Scoville et al. use functional forms that are different from ours, when fitting for evolution of  $\tau_{\text{depl}}$ . For example, Tacconi et al. consider additional dependence on the effective radius  $R_e$ , which might inadvertently carry some redshift dependence. As such the fitted exponents are not necessarily directly comparable. The differences between evolutionary trends could also be attributed to the different samples used (see e.g. Hodge & da Cunha 2020).

Presumably, the existence of these outliers can be explained by an increased SFE, which results from major-merger events (see e.g. Scoville et al. 2017; Cibinel et al. 2019). In fact, galaxies that lie above the MS are also found to have increased gas fractions (Dekel et al. 2009; Tacconi et al. 2020), which is attributed to a more efficient gas accretion from the cosmic web, but the enhanced gas reservoirs are still not large enough to ex-

plain significantly enhanced sSFR. The debates regarding the exact reason, which results in an onset of a SB-like mode of star-formation, are still ongoing, however it seems very likely that it is a combination of both increased gas fractions and enhanced SFE. We find that our sample supports this notion, with galaxies above the MS having both large gas reservoirs with median  $\log(f_{\text{gas}})=0.15$ , meaning that gas mass reservoirs take up  $\sim 59\%$  of the total baryonic matter, and also relatively short depletion times of  $\sim 400$  Myr. Our  $M_{\text{gas}}$  values were however derived with a general FMR, assuming solar-like metallicities. This, however, might not be applicable for SBs, which can display elevated metallicities due to the increased sSFR. In fact it has been shown (see e.g. Silverman et al. 2015), if SBs had super-solar metallicities, it would drive down  $\delta_{\text{GDR}}$  together with  $f_{\text{gas}}$ , and in turn result in increased SFE, thus implying that only the SFE is responsible for galaxies being elevated above the MS.

### 8.3. On the DMFs and the Theoretical Predictions

With the derived DMF in hand, we are also in position to bring together our findings with those presented in previous observationally driven studies and provide a direct comparison to the theoretical predictions as inferred by recent simulations. For our purposes, we focus on the  $0.2 < z < 0.5$  redshift interval that contains the majority of our objects and offers the most robust statistical analysis. These results are shown in Figure 15.

We first compare our DMF to that presented in Pozzi et al. (2020), based on a PACS-160  $\mu\text{m}$  selected sample of SFG. In Figure 15, the two DMFs appear to be in tension both in the high and the low-mass end, with our compilation over-predicting the number density of galaxies with high  $M_{\text{dust}}$  and under-predicting that of less dusty sources. The discrepancy between the two DMFs can be attributed to the choice of fitting methods/templates, the adopted  $\kappa_{\nu}$  to infer  $M_{\text{dust}}$  as well as to selection effects. For example, the DL07 templates adopt a  $\kappa_{250\mu\text{m}}$  of  $0.51 \text{ m}^2 \text{ kg}^{-1}$ , while the analysis in Pozzi et al. uses  $\kappa_{250\mu\text{m}} = 0.4 \text{ m}^2 \text{ kg}^{-1}$ , which would result in a 0.1 dex smaller  $M_{\text{dust}}$  estimates. It is also important to point out that Pozzi et al. compared their MBB SED fitting to MAGPHYS, finding that their MBB method recovers systematically lower  $M_{\text{dust}}$ . Indeed, choice of the fitting methodology can induce up to a factor of two difference in derived  $M_{\text{dust}}$  (see e.g. Magdis et al. 2013 and an in-depth comparison in Berta et al. 2016). Moreover, for a flux limited survey, the mere selection at  $\lambda_{\text{obs}}=160 \mu\text{m}$  could introduce a bias towards warmer sources that for fixed  $L_{\text{IR}}$  have lower  $M_{\text{dust}}$  and which could explain the small number density of sources

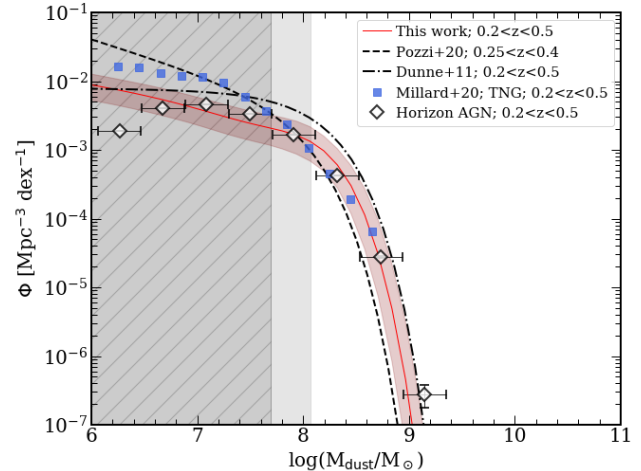


**Figure 15.** A compilation of the theoretical and observationally derived DMFs in the  $0.2 < z < 0.5$  range. The Davidzon et al. (2017) SMF, converted to DMF, is shown as the solid red line, with the shaded area corresponding to the  $1\sigma$  uncertainty. The dashed and dash-dotted black lines correspond to the DMFs of Pozzi et al. (2020) and Dunne et al. (2011) respectively, rescaled to  $\kappa_{250\mu\text{m}} = 0.51 \text{ m}^2 \text{ kg}^{-1}$ . The white diamonds and the blue squares depict the theoretical predictions of the HAGN and TNG simulations from Dubois et al. (2014) and Millard et al. (2020) respectively. The grey shaded region highlights the  $M_{\text{dust}}$  regime below the  $\text{lim}(M_{\text{dust}})$  of our sample, as derived in Figure 6. The hatched region denotes the  $M_{\text{dust}}$  regime where our sample becomes severely limited, i.e.  $> 1\sigma$  below  $\text{lim}(M_{\text{dust}})$ .

with  $\log(M_{\text{dust}}/M_{\odot}) > 8$ . While it is not possible to correct for the effects of selection and broader SED fitting methodology, we have rescaled the Pozzi et al. DMF to have the same  $\kappa_{250\mu\text{m}}$  as was adopted in our analysis.

We also compare our results to Dunne et al. (2011), that computed a DMF based on a sample of 250  $\mu\text{m}$  selected galaxies. For our comparison, we have rescaled their DMF by  $-0.24$  dex, to account for the difference in  $\kappa_{\nu}$ . Contrary to Pozzi et al. (2020), we now find that Dunne et al. (2011) over-predicts the number density of dusty galaxies at high dust masses. This again can be understood in terms of selection effects since the 250  $\mu\text{m}$  selection could bias the sample towards cold sources and thus to higher  $M_{\text{dust}}$  values (again, for a flux limited survey). While our criterion for at least one detection at  $\lambda_{\text{rest}} > 150 \mu\text{m}$  could be perceived as similar to a 250  $\mu\text{m}$  selection at  $z \sim 0.3$ , we note that the requirement for two extra detections at  $\lambda_{\text{rest}} < 150 \mu\text{m}$ , and the super-deblended catalogues, that allow for the detection of fainter than the nominal confusion noise in the SPIRE bands, ease any bias towards either intrinsically cold or

warm objects. This is further supported by the fact that our SMF-derived DMF, where the Eddington bias has already been corrected, falls directly between the calculations from Pozzi et al. and Dunne et al. (Figure 15). In conjunction with the derivation of a  $\langle U \rangle - z$  relation that is in excellent agreement with the stacking analysis of Béthermin et al. (2015), this suggests that the careful treatment of selection criteria and of the detection limits of our parent sample has allowed us to gain a unique and unbiased perspective on the evolution of dust properties of COSMOS galaxies.

Finally, we compliment our analysis by comparing our DMF to the theoretical predictions of the HAGN and IllustrisTNG simulations (Millard et al. 2020). In order to produce a HAGN DMF, we define a simulated sample following the procedure described above, bin the galaxies in 0.4 dex intervals of  $M_{\text{dust}}$ , and normalise by the volume of the simulation ( $4 \times (142)^3 \text{ Mpc}^3$ ). For the IllustrisTNG simulation, Millard et al. (2020) consider multiple TNG100 snapshots in a box size of 106 Mpc per side, comparable to the HAGN simulated subset presented earlier. The TNG-DMF is constructed through the  $M_{\text{dust}}$  values of the simulated galaxies, derived in post-processing through a fixed dust-to-metals ratio of 0.5.

Unlike real data, simulations do not suffer from observational bias, and as such should be compared to DMF derived from the SMF, without adding the Eddington bias. As shown in Figure 15, both HAGN and IllustrisTNG are in excellent agreement with the high-mass end of our SMF-derived DMF. Notably, the HAGN-DMF is also consistent with our results at the low-mass end down to  $M_{\text{dust}} \sim 10^7 M_{\odot}$ . We recall, that for simplicity, when converting  $M_{\text{gas}}$  to  $M_{\text{dust}}$  for the HAGN sample, we considered a universal  $\delta_{\text{GDR}} = 100$ . However, for sources with lower  $M_*$  ( $< 10^8 M_{\odot}$ ) and thus with sub-solar metallicities, a larger  $\delta_{\text{DGR}}$  ( $\sim 150$ ) is probably more applicable (Rémy-Ruyer et al. 2014). This would translate into a  $\times 1.5$  downward correction for the low-mass HAGN bins, bringing them into exact agreement with our DMF down to  $M_{\text{dust}} \approx 10^7 M_{\odot}$ . We note that this  $M_{\text{dust}}$ , assuming an average  $M_{\text{gas}}/M_{\text{dust}} \approx 100$ , corresponds to the  $M_*$  completeness limit of the simulation ( $M_* \approx 10^9 M_{\odot}$ ). Therefore, the observed decline of the number density of the HAGN galaxies at  $M_{\text{dust}} \leq 10^7 M_{\odot}$  is fully consistent with the expectations.

In comparison to the TNG-DMF though, we predict a factor of  $\times 2.5$  fewer objects at the low-mass end. This tension could arise from the incompleteness of our sample at the low-mass end, that leaves the slope of the  $M_{\text{dust}} - M_*$  relation at  $M_{\text{dust}} < 5 \times 10^7 M_{\odot}$  largely un-

constrained. We are thus unable to ascertain whether this discrepancy is caused by the limitations of our sample, or whether the TNG simulations over-predict the number density of the galaxies in the low-mass end.

Put together, these comparisons indicate that, at least down to  $M_{\text{dust}} \approx 5 \times 10^7 M_{\odot}$ , our  $M_{\text{dust}} - M_* - z$  relation and the resulting DMFs are robust and fully consistent with the theoretical expectations.

#### 8.4. Population of Gas Giants

As briefly discussed in Section 7, during our analysis we identified some extreme outliers from the average  $f_{\text{dust}}$  and  $f_{\text{gas}}$  evolutionary trends (Figure 11 and Figure 14), and which typically have  $\log(f_{\text{gas}}) > 0.5$ , i.e. their gas mass reservoir takes  $\sim 75\%$  of their baryonic matter. Since  $z_{\text{phot}}$  could be a major source of uncertainty in both  $M_*$  and  $M_{\text{gas}}$ , before looking further into this population of ‘gas-giants’, we first narrow down our sample to spectroscopically confirmed sources. We then examined the individual SEDs and the cut-out images of the remaining sources in order to identify either poor coverage of the FIR peak or blending issues that could result in erroneously large  $M_{\text{gas}}$  estimates. With the above considerations, we are left with 41 objects whose extreme  $f_{\text{gas}}$  can only be explained by gigantic  $M_{\text{gas}}$  reservoirs. This population spans a wide range in redshift ( $0.21 < z < 4.05$ ,  $\langle z \rangle = 1.34$ ), with  $9.0 < \log(M_*/M_{\odot}) < 11.3$ ,  $\langle \log(M_*/M_{\odot}) \rangle = 10.3$  and  $0.11 < \Delta\text{MS} < 14.2$ ,  $\langle \Delta\text{MS} \rangle = 1.8$ . The best-fit SEDs of two such objects are presented in Figure 16. We also note that these two sources are otherwise unremarkable, and have what can be considered ‘typical’ values for the  $\log(M_*) \sim 10.7$ , and also do not appear to be strong SBs ( $\Delta\text{MS}=3.8$  and  $2.2$ , respectively for 10041706 and 10100707). Furthermore, the cutouts presented in Figure 16 indicate that these sources do not appear to be blended, therefore the only unusual characteristic that they possess, seems to be an elevated  $M_{\text{gas}}$ .

A possible explanation for the very high  $M_{\text{dust}}$  and subsequently  $M_{\text{gas}}$  estimates for these galaxies, other than an extremely low  $\delta_{\text{GDR}}$ , could be an optically thick FIR emission. In this scenario, the attenuation of the emission in the Wien part of the spectrum makes the galaxy appear cold, leading to an overestimate of its true  $M_{\text{dust}}$  (e.g. Jin et al. 2019; Cortzen et al. 2020). Since the DL07 models assume that the galaxy is optically thin at  $\lambda_{\text{rest}} > 1 \mu\text{m}$ , to test this scenario we employed Modified Black Body (MBB) models of general opacity, leaving the effective wavelength ( $\lambda_{\text{eff}}$ ) at which  $\tau = 1$  as a free parameter (e.g. see Casey et al. 2012 for the functional form). We fixed the Rayleigh-Jeans slope to  $\beta = 1.8$ , and only fit the available photometry of each

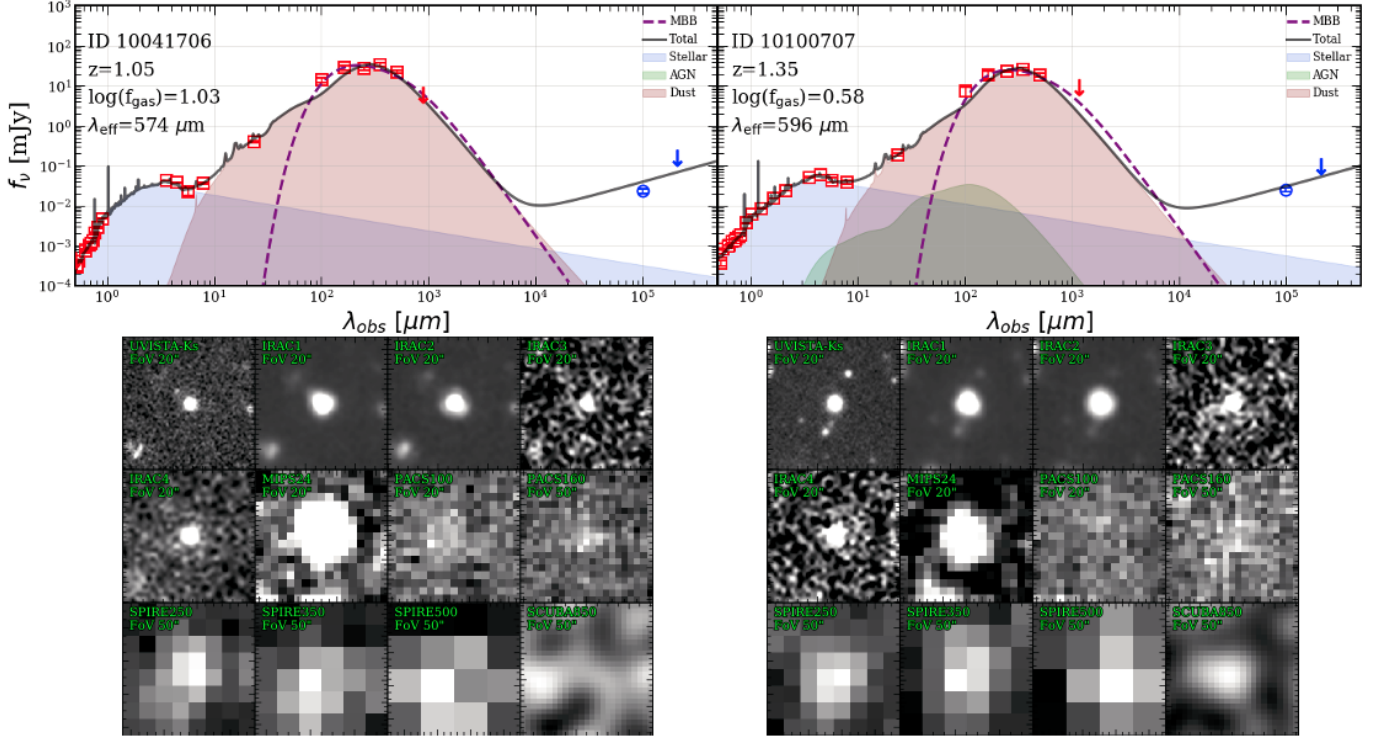


**Figure 16. Top:** Photometry and best-fit SEDs for two ‘gas-giants’ ( $\log(f_{\text{gas}}) > 0.5$ ) at  $z_{\text{spec}} = 1.05$  and  $z_{\text{spec}} = 1.35$ . Colour coding and symbols are the same as in Figure 3, with the addition of a dashed purple line that shows the best-fit optically thick MBB. The  $\lambda_{\text{eff}}$  (in rest-frame) at which the SED becomes optically thick ( $\tau = 1$ ) is displayed in the panels. **Bottom:** NIR-FIR cutouts of these objects. The cutout sizes range from  $20''$  in the NIR-MIR range to  $50''$  in FIR.

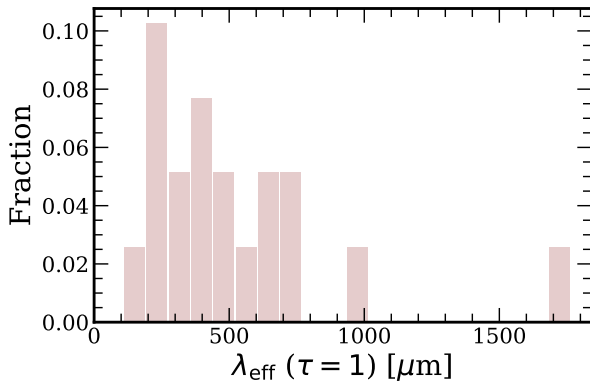


**Figure 17.** Distribution of  $\lambda_{\text{eff}}$ , below which the emission of the ‘gas-giants’ in our sample becomes optically thick ( $\tau = 1$ ), as inferred by MBB models of general opacity.

source at  $\lambda_{\text{rest}} > 40 \mu\text{m}$ . Due to the large number of free parameters in this model, we further limit our sample to sources with five or more IR detections. Out of the 41 ‘gas giants’, we are thus able to constrain  $\lambda_{\text{eff}}$  for only 19. The distribution of the inferred  $\lambda_{\text{eff}}$  values is presented in Figure 17.

We find that the vast majority of these objects have  $\lambda_{\text{eff}} > 100 \mu\text{m}$ , which implies that these galaxies could be optically thick in the FIR. The unusually high  $f_{\text{dust}}$  and  $f_{\text{gas}}$ , can therefore be incorrect simply due to the optical depth effects. Indeed, a comparison between the inferred  $M_{\text{dust}}$  estimates for an optically thin and optically thick case, yields an average ratio of  $\sim \times 1.8$  for our sample. However, while this correction would reduce the average  $f_{\text{gas}}$  of the ‘gas-giants’ from  $\langle \log(f_{\text{gas}}) \rangle = 0.72$  to  $\langle \log(f_{\text{gas}}) \rangle = 0.47$ , this is still substantially larger with respect to the average population of SFGs. Finally, the real  $f_{\text{gas}}$  could in fact be lower if the  $M_*$  of the sources is underestimated, a scenario that is indeed in line with a dusty, optically thick ISM.

To understand whether these objects do indeed host unusually high gas mass reservoirs and shed light on their nature, additional observations, with either ALMA or NOEMA, of  $M_{\text{gas}}$  tracers (e.g. CO and CI) are necessary.

## 9. SUMMARY

In this work we present an in-depth analysis of the evolution of the FIR properties of SFGs by studying a large sample of sources drawn from the publicly available in-



frared catalogues in the GOODS-N and COSMOS fields (Liu et al. 2018; Jin et al. 2018). Both catalogues are constructed based on a novel ‘Super-Deblending’ technique that allows prior-based photometry in the highly confused *Herschel* and *SCUBA+AzTEC* maps.

In the process, we developed a new panchromatic SED fitting algorithm - *Stardust* - to fit a linear combination of stellar, AGN and infrared (star-forming) templates, in an attempt to perform a coherent, systematic and homogeneous analysis in the two fields. Our fitting tool has two key advantages. Firstly, the best-fit model is a set of coefficients rather than a single template, thus it does not rely on iterating through thousands of possible template combinations, speeding up the fitting process by a factor of  $\sim 10$  compared to other multi-wavelength fitting available codes. Secondly, the fitting process does not impose energy balance between absorption in the UV/optical and emission in the IR, treating the stellar and the dust emission components independently. As such, it is very relevant for sources where the stellar and dust emission are not co-spatial. The code itself is also highly modular, allows for user input templates, and is publicly available.

A first product of this new software is a multi-parameter catalogue that contains the FIR properties of  $\sim 5,000$  infrared bright galaxies in GOODS-N and COSMOS. The extracted parameters, their uncertainties and the matched photometry from the original ‘Super-Deblended’ catalogues are released and are also publicly available<sup>12</sup>. The list of output best-fit parameters and the structure of the released catalogue can be found in Table 3.

We subsequently used the extracted parameters to explore the evolution of the FIR properties of SFGs and recover scaling relations, aided by a careful set of simulations that quantify the underlying selection effects and biases of our sample in terms of limiting  $M_{\text{dust}}$ ,  $L_{\text{IR}}$  and  $\langle U \rangle$ . In particular, we parametrised the  $f_{\text{dust}}$  of galaxies as a function of their cosmic age,  $M_*$ , and  $\Delta\text{MS}$ . The median  $f_{\text{dust}}$  is found to increase by a factor of  $\times 10$  from  $z = 0$  to  $z = 2$  with a mild, if any, evolution at higher  $z$ . Through the metallicity dependent  $\delta_{\text{GDR}}$  technique, we also derive the evolution of  $f_{\text{gas}}$  and find it to be consistent with previous observational studies, as well as with theoretical predictions.

Furthermore, we constructed the DMF up to  $z = 1$  by converting the SMF of SFGs to a DMF, through the evolution of  $f_{\text{dust}}$  and its scatter, as parametrised

in our study. A comparison of the derived DMFs to the theoretical predictions of the HAGN and TNG100 simulations in the  $0 < z < 0.5$  range reveals an excellent agreement down to a limiting  $M_{\text{dust}} \sim 5 \times 10^7 M_{\odot}$ , where due to poor statistics we cannot adequately constrain the  $M_{\text{dust}}-M_*$  relation.

Finally, we identified a population of SFGs with extreme  $\log(f_{\text{gas}}) > 0.5$ , that we coin as ‘gas giants’. The  $f_{\text{gas}}$  excess of these galaxies compared to the average SFG population persists even when opacity effects in the FIR emission are taken into account. Follow-up observations targeting alternative  $M_{\text{gas}}$  tracers are necessary to confirm the extreme nature of these systems.

Some further remarks that we would like to emphasise:

- The effect of the photo- $z$  uncertainty in the derivation of  $M_{\text{dust}}$  (and  $L_{\text{IR}}$ ) is not negligible and should be accounted for. We find that a photo- $z$  uncertainty of  $\Delta z / (1+z_{\text{spec}}) \sim 0.02$ , characteristic of fields like GOODS-N and COSMOS, introduces an extra 20% of scatter in the derivation of  $M_{\text{dust}}$  and  $L_{\text{IR}}$ .
- As already discussed in the literature, the uncertainty in the derivation of  $M_{\text{dust}}$  increases substantially in the absence of a data point in the R-J tail ( $\lambda_{\text{rest}} > 150 \mu\text{m}$ ). However, the presence of three data points in the mid-to-FIR could securely constrain  $M_{\text{dust}}$  within a factor of  $\sim 0.3$  dex, even if the last available data point is at  $\lambda_{\text{rest}} \approx 150 \mu\text{m}$ .
- When using the  $M_{\text{dust}} - M_* - z$  scaling relations to convert SMF to DMF (or similarly to gas mass functions), the scatter of the relations used for the transformation should be taken into account for a proper comparison to the data. Similarly, any attempt to derive scaling relations between two (or more) parameters through the comparison of mass (or luminosity) functions inferred through the modelling of the observed number densities should entail a proper consideration of the scatter of the parameters in question.
- Both the warm  $M_{\text{dust}}$  and the warm IR emission arising from the PDRs are increasing with respect to the cold  $M_{\text{dust}}$  and cold dust emission as we move above the MS, indicative of more compact/active star-forming activity. Subsequently, the clear and relatively tight trend of decreasing  $M_{\text{dust}}^{\text{cold}}$  (for fixed  $L_{\text{IR}}$ ) with  $\Delta\text{MS}$  is less pronounced for  $M_{\text{dust}}^{\text{warm}}$ . This enforces the overall picture where SBs are characterised by higher star-formation efficiencies and with a larger fraction of their  $M_{\text{dust}}$  being exposed to more intense radiation fields.

<sup>12</sup> Tables containing the DMFs can be accessed here: [https://github.com/VasilyKokorev/sdc.ir\\_properties](https://github.com/VasilyKokorev/sdc.ir_properties)

## ACKNOWLEDGMENTS

We would like to thank the anonymous referee for a number of constructive suggestions. We thank Yohan Dubois and Clotilde Laigle for providing us with HAGN data and their input towards the discussion of simulations, Jenifer Millard for providing us with the DMF data, and Benjamin Magnelli for the help in understanding the dust mass density evolution. The Cosmic Dawn Center is funded by the Danish National Research Foundation under grant No. 140. GEM acknowledges the Villum Fonden research grant 13160 “Gas to stars, stars to dust: tracing star formation across cosmic time,” grant 37440, “The Hidden Cosmos,” and the Cosmic Dawn Center of Excellence funded by the Danish National Research Foundation under the grant No. 140. FV acknowledges support from the Carlsberg Foundation research grant CF18-0388 “Galaxies: Rise And Death”. ID acknowledges support from the European Union’s Horizon 2020 research and innovation programme under the Marie Skłodowska-Curie grant agreement No. 896225. ST, GB and JW acknowledge support from the European Research Council (ERC) Consolidator Grant funding scheme (project ConTEExt, grant No. 648179). SJ acknowledges financial support from the Spanish Ministry of Science, Innovation and Universities (MICIU) under AYA2017-84061-P, co-financed by FEDER (European Regional Development Funds). DL acknowledges funding from the European Research Council (ERC) under the European Union’s Horizon 2020 research and innovation program (grant agreement No. 694343). This work has made use of the CANDIDE Cluster at the Institut d’Astrophysique de Paris and made possible by grants from the PNCG and the DIM-ACAV.

## APPENDIX

## A. SED FITTING

A.1. *Draine & Li (2007) Templates*

In our fitting routine we utilise the dust models of [Draine & Li \(2007\)](#), with the updated opacity from [Draine et al. 2014](#). These models aim for a robust and physically motivated approach to SED fitting in both MIR and FIR, as well as allow us to calculate the amount of luminous dust.

The description of the dust locked in the interstellar medium is one of a mixture of carbonaceous and amorphous silicate grains, with their sizes and distributions following the extinction law in the Milky Way, Large Magellanic Cloud (LMC) and the bar region of the Small Magellanic Cloud (SMC). The carbonaceous grains behave similarly to the polycyclic aromatic hydrocarbon (PAH) molecules, with their properties given by the PAH index  $q_{\text{PAH}}$ , that is defined as a fraction of dust mass locked into the PAH grains.

The models provide a bimodal description of the environments containing the interstellar dust: the diffuse ISM and the PDRs. The bulk of the dust mass is thought to be located in the cold and diffuse part of the interstellar medium, that is being heated by a radiation field of a constant intensity  $U_{\text{min}}$ . A smaller proportion of the mass budget described by the  $\gamma$  index is exposed to a gradient of radiation intensities ranging from  $U_{\text{min}}$  to  $U_{\text{max}}$ , and is supposedly located in the warmer PDRs. Although these warm regions normally contain only a small fraction of the total dust mass, they can make a substantial contribution to the luminosity in the mid-IR SEDs. As described by [DL07](#), the infinitesimal proportion of  $dM_{\text{dust}}$  exposed to radiation fields between  $U$  and  $U + dU$  can be modelled by a power law distribution, and in the case of the diffuse ISM where  $U_{\text{min}} = U_{\text{max}}$ , by a Kronecker  $\delta$ -function. This leads to the following description:

$$dM_{\text{dust}} = (1 - \gamma) \delta(U - U_{\text{min}}) + \gamma M_{\text{dust}} \frac{\alpha - 1}{U_{\text{min}}^{1-\alpha} - U_{\text{max}}^{1-\alpha}} \quad (\text{A1})$$

with  $U_{\text{min}} \leq U_{\text{max}}$  and  $\alpha \neq 1$ . The parameter -  $\gamma$  - is the fraction of dust mass locked into the high starlight intensity regions described by the power-law,  $\alpha$  gives the distribution of radiation intensities in the PDRs and  $M_{\text{dust}}$  as the total dust mass.

The methods described in [DL07](#) allow us to compute a distribution of temperatures for all particles: ones that are small so their size makes them susceptible to the ef-

fects of quantised heating, and the larger ones where the steady-state temperatures dictated by the stellar radiation and radiative cooling equilibrium take hold. One can compute an averaged IR emission for a given grain type by first considering their temperature distribution and cross sections, and then sum everything up to obtain the specific mass weighted power that is being radiated by the dust exposed to starlight of intensity  $U$ . By integrating these numerical recipes from  $U_{\text{min}}$  to  $U_{\text{max}}$ , one can obtain the power per unit frequency per unit mass  $p_{\nu}(q_{\text{PAH}}, U_{\text{min}}, U_{\text{max}}, \alpha)$ .

In line with [DL07](#), one can then model the galaxy spectral energy distribution as a linear combination of the diffuse ISM and the PDRs. This can be written as follows:

$$j_{\nu} = (1 - \gamma) j_{\nu}[U_{\text{min}}, U_{\text{max}}] + j_{\nu}[U_{\text{min}}, U_{\text{max}}, \alpha] \quad (\text{A2})$$

where  $j_{\nu}$  is the emissivity per hydrogen nucleon. If one now considers a galaxy at some distance  $D_{\text{L}}(z)$ , the received flux density can be written as:

$$f_{\nu} = \frac{M_{\text{H}}}{m_{\text{H}}} \frac{j_{\nu}}{D_{\text{L}}^2(z)}. \quad (\text{A3})$$

Since  $j_{\nu}$  is the quantity contained in the [DL07](#) models, the normalisation extracted from the fitting represents the total number of hydrogen nucleons, and can be then converted to the luminous dust mass.

The total luminosity contained in both dust components can be written as:

$$L_{\text{dust}} = \langle U \rangle P_0 M_{\text{dust}} \quad (\text{A4})$$

with  $\langle U \rangle$  representing a mean intensity of the radiation field, given by:

$$\langle U \rangle = (1 - \gamma) U_{\text{min}} + \frac{\gamma \ln(U_{\text{max}}/U_{\text{min}})}{U_{\text{min}}^{-1} - U_{\text{max}}^{-1}}, \quad (\text{A5})$$

for  $\alpha = 2$  and  $P_0$  denoting the power absorbed per unit dust mass in a radiation field of intensity  $U = 1$ .

In principle, one could think of these models as having six effective free parameters -  $q_{\text{PAH}}$ ,  $U_{\text{min}}$ ,  $U_{\text{max}}$ ,  $\alpha$ ,  $\gamma$  and  $M_{\text{dust}}$ - acting as the normalisation as described above. It has been shown in [Draine et al. \(2007\)](#) that the parameter space is insensitive to the adopted dust model (MW, LMC and SMC) and the values of  $\alpha$  and  $U_{\text{max}}$ . It is possible thus to recover a wide range of properties of various SEDs by fixing these to  $\alpha = 2$  and  $U_{\text{max}} = 10^6$ . The values of  $U_{\text{min}}$  below 0.7 correspond to temperatures

below 15 K, and while it is expected to find very few systems that exhibit this behaviour, we have decided not to limit the range of  $U_{\min}$  and allow it to vary between 0.1 and 50, to capture even the most extreme cases. It has been shown that at least in the case of local galaxies in the Spitzer Nearby Galaxy Survey (SINGS), the  $U_{\min}$  can be limited between  $0.7 \leq U_{\min} \leq 25$ , and a MW-like dust model can be adopted to limit  $q_{\text{PAH}}$  between 0.004 and 0.046. Incorporating the use of the optimised set of parameters, which has been done in similar studies (e.g., Magdis et al. 2012a; Magnelli et al. 2012; Santini et al. 2014), might have a positive effect on computational speeds, however we need to consider that this reduced parameter space has only been robustly verified for nearby solar-like metallicity populations of galaxies and might otherwise risk under(over)estimating the dust masses for extremely cold(warm) systems.

We can thus extract the following physical parameters from the fit -  $\gamma$ ,  $q_{\text{PAH}}$ ,  $U_{\min}$ . The dust mass is simply computed from the normalisation, while the  $L_{\text{IR}}$  is  $L_{\nu}$  integrated over the 8 - 1000  $\mu\text{m}$  range. As an additional parameter, we can obtain  $\langle U \rangle$  by either utilising the Equation A5, or alternatively, as prescribed by Magdis et al. (2012a), we can use Equation A4, where we set  $L_{\text{dust}} = L_{\text{IR}}$  and  $P_0 \approx 125$ .

### A.2. Removing AGN contamination

Active galactic nuclei (AGN) can have a significant impact on the ISM of galaxies that host them. They possess an ability to halt star-formation by heating up the gas and dust or completely quenching the galaxy by stripping away its fuel. Under the common assumption (Antonucci 1993; Urry & Padovani 1995; Tristram et al. 2007), AGN are surrounded by dusty tori, that similarly to the ISM dust, can absorb the UV/optical light from the AGN and re-radiate it at redder wavelengths, normally peaking in the mid-infrared (MIR) regime at 20-50  $\mu\text{m}$ . It has also been shown that for select extreme cases (Mullaney et al. 2011), the AGN emission dominates the SED of a galaxy even at 60  $\mu\text{m}$ , which presents a new challenge when calculating an infrared luminosity of a source. Infrared derived star-formation rate estimates rely on a robust understanding of the  $L_{\text{IR}}$ . Therefore, it is imperative to separate the energy contributions from hot dust in the ISM and a possible AGN.

In order to account for the effects of the IR contamination by AGN when calculating  $L_{\text{IR}}$ , as well as to identify all the possible systems that might contain an active nucleus in our sample, we have decided to adopt a set of AGN templates from Mullaney et al. (2011) (M11). These templates have been empirically derived by assuming a modified blackbody function and fitting

it to a set of Swift-BAT AGNs as well as IRAS spectra. The obtained models describe intrinsic AGN emissions in the range spanning from MIR to FIR (6-100  $\mu\text{m}$ ). In this case, a typical AGN SED could be thought of as a broken power law at  $\leq 40 \mu\text{m}$ , that rapidly vanishes when moving above 40  $\mu\text{m}$ . The average intrinsic AGN emission can be described as follows:

$$F_{\nu} = \begin{cases} \lambda^{1.8} & \text{at } 6 \mu\text{m} < \lambda < 19 \mu\text{m} \\ \lambda^{\alpha} & \text{at } 19 \mu\text{m} < \lambda < 40 \mu\text{m} \\ \nu^{1.5} F_{\nu}^{BB} & \text{at } \lambda > 40 \mu\text{m} \end{cases} \quad (\text{A6})$$

where  $F_{\nu}^{BB}$  is the modified blackbody function and  $\alpha$  is the spectral index. In our procedure we utilise the high and the low luminosity templates, with the  $\alpha = 0.0$  and 0.4 respectively. In addition to that, we allow for a linear combination between the two, with varying coefficients, thus expanding the existing template space.

### A.3. Stellar emission component

The contribution of stellar emission in the observed NIR bands, such as *Spitzer* IRAC 1-4, can be quite significant, especially when we move to higher  $z$ . Therefore, if no libraries representing the luminosity from dust attenuated stellar light are available, one might either underestimate the slope of the AGN or overestimate its normalisation. This can lead to erroneously assigning more luminosity to the AGN component in the MIR and therefore underestimating the  $L_{\text{IR}}$ .

To avoid this, we additionally incorporate a library of stellar emission models, which are an updated version of the templates described by Brammer et al. (2008) (GB08). These are based on the stellar population synthesis models (Conroy et al. 2009), that were optimised for deep optical-NIR broadband surveys. The models form a basis set of a larger library, and were derived by using the 'non-negative matrix factorization' algorithm that was described in Blanton & Roweis (2007). The method attempts to reproduce the full library of templates, by finding a non-negative linear combination of a smaller number of models. These can be considered as the 'principal component' blueprint of the larger catalogue. In total there are 12 optical SEDs, which include both dust attenuated and non-attenuated starlight. We have incorporated these models into our fitting routine, and if the UV-optical photometry is available, this allows us to extract properties such as  $M_*$ , SFR,  $E(B-V)$  and SFH. If no UV-optical data is available, the addition of these templates is still useful, as they can account for the excess flux in the rest-frame NIR bands, in conjunction with AGN and IR templates.

To test how our fits behave without the stellar component, we have isolated  $\sim 100$  objects with  $z > 2$ ,



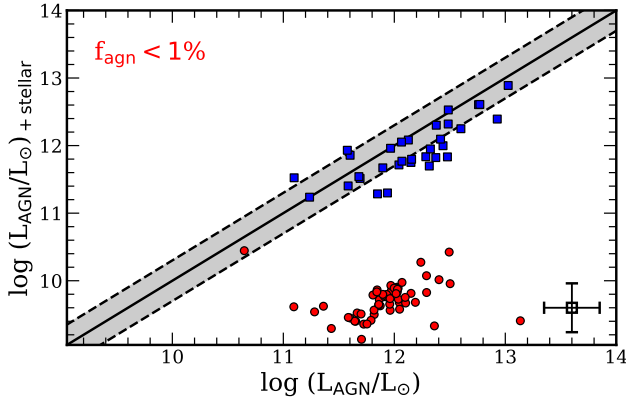


**Figure 18.** A comparison between fits that incorporate the stellar component, and those that do not for  $z > 2$  galaxies. Blue squares and red circles represent objects which were assigned  $f_{\text{AGN}} > 0.01$  and  $f_{\text{AGN}} < 0.01$  respectively, by the means of our three component fit. The median uncertainty for both quantities is in the bottom right corner. The black solid line represents the 1:1 relation and the grey regions cover the 0.3 dex range.

so that our bluest available band traces  $\lambda_{\text{rest}} \sim 1 \mu\text{m}$ , where the contribution from stellar emission becomes non-negligible. We then exclude GB08 templates and re-fit our objects. This results in two outcomes that can be seen in Figure 18. We find that, by removing the additional component, we tend to either overestimate the AGN contribution (blue squares), with the median being  $\sim 1.5$ , or alternatively erroneously assign a galaxy to contain an AGN (red points).

#### A.4. Bringing it all together

In order to model an SED of a galaxy and extract the physical parameters, we first transport all three components - the stellar, the dusty torus AGN and the infrared dust emission to a common wavelength grid spanning the range from  $10^{-4}$  to  $10^5 \mu\text{m}$ . Our method relies on a linear combination of these models, thus making it imperative for them to share a common range, so that co-adding them is made possible. In certain cases where this grid falls outside the original range of the template, we extrapolate bluewards and redwards by using a steeply declining power law. This was done to ensure that the resultant galaxy emission is continuous without any sudden breaks, which could interfere with the fitting, where one of the templates has ran out of range. These added power laws do not introduce any additional emission, as the flux density contribution from them is orders of magnitude lower than that of the original template. We then redshift the wavelength grid on a per galaxy basis and normalise the templates to ensure that

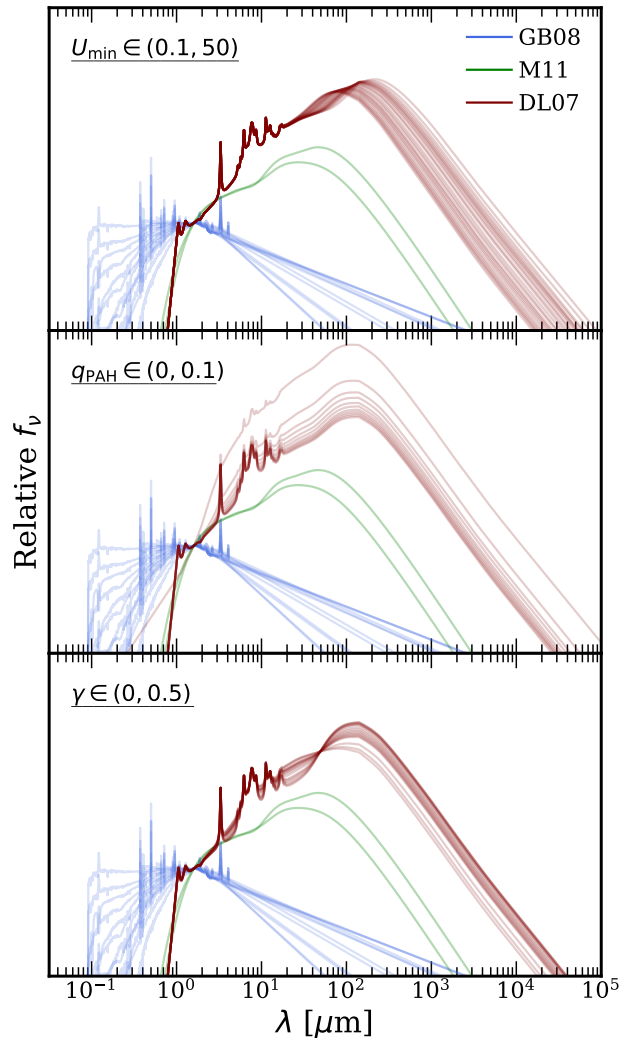


**Figure 19.** A compilation of all template flavours used in *Stardust*. Colour-coding is blue, green and maroon for [Brammer et al. 2008](#) UV-Optical SPS models, [Mullaney et al. 2011](#) AGN models, and [Draine et al. 2007](#) IR dust models respectively. We show the variations in  $U_{\text{min}}$ ,  $q_{\text{PAH}}$ , and  $\gamma$  separately on each panel, while other parameters are fixed. For visualisation purposes all templates shown here have been normalised to the  $K$ -band.

they are not separated by tens of orders of magnitude. In Figure 19 we show all the templates used in *Stardust*, normalised to the  $K$ -band, and in Table 2 we list all the relevant parameters of the models.

Subsequently, we perform a synthetic photometry on all three components separately in all observed bands where data is available. This is done by convolution of the filter transmission curves with the model SEDs. The resultant synthetic fluxes for each template and available observed band are then all combined into a two-dimensional matrix and passed onto

**Table 2.** Template parameters used for **Stardust** fit.

Parameter	Value
Dust emission: DL07 (Updated in <a href="#">Draine et al. 2014</a> )	
$U_{\min}$	[0.1, 0.2, 0.3, 0.4, 0.5, 0.6, 0.7, 0.8, 1.0, 1.7, 2.0, 3.0, 4.0, 5.0, 7.0, 8.0, 10.0, 12.0, 15.0, 20.0, 25.0], 26 values
$q_{\text{PAH}}$	[0; 0.1], 11 values in steps of 0.1
$\gamma$	[0, 0.001, 0.0025, 0.005, 0.0075] +[0.01; 0.1], 9 values in steps of 0.01 +[0.2, 0.35, 0.5], 17 values in total
Optical emission: <a href="#">Brammer et al. 2008</a> <sup>a</sup>	
$A_V$ ( <a href="#">Calzetti et al. 2000</a> )	[0.6, 0.12, 0.19, 0.29, 1.05, 2.68, 0.11, 0.36, 0.98, 1.54, 1.97, 2.96]
$M/L_V$	[0.38, 0.76, 1.68, 4.01, 6.45, 44.48, 0.12, 0.21, 0.33, 0.64, 1.57, 4.00]
$\log_{10}(\text{sSFR})$	[-10.75, -11.37, -11.90, -12.53, -12.05, -12.47, -8.37, -8.60, -8.50, -8.57, -8.93, -8.90]

<sup>a</sup> Please refer to [Brammer et al. 2008](#) for a more detailed description of the creation and selection of these basis set templates. See [Blanton & Roweis 2007](#) for a methodology regarding the SFH.

the non-negative least square (nnls) algorithm in the python `scipy.optimize.nnls` package, that finds the best solution vector for that object. The nnls is a simple minimisation algorithm that in our case takes the form of,

$$\min \|A_{b,t}x^t - y^b\|_2 \quad \text{where } x \geq 0, \quad (\text{A7})$$

with  $A$  being the uncertainty weighted template matrix,  $y$  as the signal to noise for each band respectively,  $x$  the solution vector and  $\|\cdot\|_2$  signifying the Euclidian norm. Instead of finding the best fitting template, the algorithm computes the best-fit coefficients  $x$ , with  $x \geq 0$ . The number of simultaneously fit templates is user defined. For our purposes we chose to fit all 12 GB08 and 2 M11 templates at the same time, each time combining them with a single DL07 template, and iterating through all the possible combinations, and then finding the best fit. Following the [Equation A7](#), this is done by building the matrix  $A$ , for each band  $b$ , and each template  $t$ , where the first 14 templates in the matrix remain fixed, while the last element is being continuously replaced with a new DL07 model and looped over. In the end we obtain 4,862 possible best-fit vectors -  $x^t$ , one per each DL07 model. The final result is then extracted from the  $\chi^2$  distribution of all best-fit solutions. The advantage of this method is in avoiding progressively looping over all possible template combinations to find the best solution, and instead only choosing to loop through DL07 templates. This approach significantly reduces the amount of required computational resources. The resultant solution vector encodes the individual contributions from

each template to the total emitted flux in each band. These are then added together to return the best fit solution. These three component split allows us to predict exactly how much each component contributes to the source's  $L_{\text{IR}}$ , thus allowing us to differentiate between the AGN and the warm ISM dust emissions. In addition to that, the normalisation of DL07 templates leads us directly to the number of hydrogen nucleons, linking it to dust mass via [Equation A4](#). The radio data points are not being considered by our fitting routine, however we add a power-law radio slope with a spectral index of  $-0.75$ , as described by the FIR-radio correlation in [Delvecchio et al. \(2020\)](#), mainly for visualisation purposes, but also to detect the existence of the AGN radio excess.

### A.5. Calculating the IR properties

To derive luminosity estimates, we integrate the three component summed SED in the  $8 - 1000 \mu\text{m}$ . This gives us the  $L_{\text{IR,tot}}$  that contains within itself the energy emitted by the ISM dust and AGN torus, if present. The contribution of stellar emission at  $\lambda_{\text{rest}} > 8 \mu\text{m}$  is negligible, therefore we do not go through an additional step of subtracting those models. We then integrate the best fit template with just the AGN contribution in it, to obtain the  $L_{\text{AGN}}$  and  $L_{\text{IR}} = L_{\text{IR,tot}} - L_{\text{AGN}}$ . We also compute the  $f_{\text{AGN}} = L_{\text{AGN}}/L_{\text{IR,tot}}$  to estimate how strongly the infrared SED of a galaxy is contaminated by AGN activity. In addition to that, it allows us to separate our sample into objects that have an active nucleus and those that do not. The conditions of the ISM in these different environments may vary quite significantly and would affect the extracted scaling relations if not treated correctly.

The normalisation of the DL07 models returns the number of hydrogen nucleons as one of its free parameters, from which we can obtain the fiducial  $M_{\text{H}}$ . We then compute  $M_{\text{dust}}$  by converting this quantity assuming a fixed gas-to-dust ratio of  $\delta_{\text{GDR}} = 100$ , as prescribed in DL07. It is important to note that this ratio is encoded into the models and does not represent an actual physically meaningful conversion factor. We also compute a  $T_{\text{dust}}$  proxy in the form of the average radiation field intensity  $\langle U \rangle$ , from [Equation A4](#), by assuming a  $P_0 = 125$ . We note however that this quantity represents the luminosity-weighted dust temperature and has little to no bearing on the temperature of the cold dust or gas (see e.g. [Scoville et al. 2016, 2017](#)).

## B. STELLAR MASS COMPARISON

To test the robustness of **Stardust** - derived  $M_*$  estimates we start by first comparing them to the  $M_*$  as

given by the original catalogue. The SDC2 takes its  $M_*$  directly from the COSMOS 2015 catalogue (Laigle et al. 2016), which uses SED fitting code **LePhare** (Arnouts et al. 1999; Ilbert et al. 2006) to constrain both the photometric redshift,  $M_*$ , as well as a host of other parameters. Similarly to our approach, **LePhare** relies on Bruzual & Charlot (2003) SSP libraries to fit galaxy SEDs. We begin our fitting procedure by carefully correcting all the COSMOS 2015 aperture fluxes to total fluxes, as well as correcting for the MW extinction, as prescribed in Laigle et al. (2016). We then cross-match these sources to SDC2, by using the  $K$ -band, and fit the entirety of available 36 bands with our code. As a sanity check, we additionally run the same photometric catalogue through **EAZY**, albeit stopping at IRAC 2.

We present this comparison in Figure 20. The  $M_*$  given by the parent catalogue and the ones derived by **Stardust** derived  $M_*$ , agree very well, with **Stardust** on average under-predicting the  $M_*$  by  $\sim 0.01$  dex. We attribute a considerable 0.31 dex scatter to the fact that in their **LePhare** fit, Laigle et al. have used an iterative procedure, that involved correcting the observed fluxes in order to match the colours of the model library.

More reassuringly, we find a good correlation when comparing our  $M_*$  to **EAZY**, with a median offset of  $-0.03$  dex and a minor 0.15 dex scatter being most likely induced by the fact that with **Stardust** we fit the entire available spectrum from UV to FIR, as opposed to just UV-optical, with **EAZY**.

### C. COMPARISON WITH CIGALE

In order to better understand how our independent linear combination approach compares to the energy balance method, we have fit our sources with **CIGALE**. For this we have utilised a set of simple stellar population (SSP) models from Bruzual & Charlot (2003) for the non-obscured stellar light, the revised version of the Draine & Li (2007) templates for the obscured stellar light, reprocessed by dust, and Fritz et al. (2006) for the AGN contribution. The attenuation law that we considered was described in Calzetti et al. (2000). For the SSP templates, we have assumed a single delayed SFH. These **CIGALE** fits should be treated as a ‘basic’ first-pass approach, due to the computational limitations necessitating a constrained range for the template parameters. Ideally, such an analysis would require a flexible SFH, in order to obtain better SFR, as well as a wider range of parameters, both for the DL07 and Fritz et al. templates.

We show the comparison between the two methods in Figure 21. There is a very good agreement between the  $M_{\text{dust}}$  derived with our code and **CIGALE**, with the dif-

ference having a mean of 0.09 dex and median of 0.02 dex. The derived values of  $L_{\text{IR}}$  are however in tension, with a mean of 0.20 dex and median of 0.11 dex. We attribute the significant outliers ( $> 1\sigma$ ) to cases where the energy balance method in **CIGALE** has failed to account for the extra FIR flux. We also compare the **Stardust** and **CIGALE** computed  $M_*$ , and find that the two agree within 0.1 dex, albeit with a significant 0.3 dex scatter. As we have already discussed in Section 3, in certain environments the stellar and the dust emission could be spatially disconnected, thus the energy balance might not be the best physically motivated option. In addition, when dealing with extreme sources, the Calzetti et al. attenuation law might not allow the energy balance approach to account for all IR flux (e.g. see Buat et al. 2019). The above, however, are not the only explanations, as the identification/matching problems as well as IR flux extractions could also play a part in creating this tension between our results and **CIGALE** (e.g. see Małek et al. 2018).

When directly comparing computation times, it is important to note that, **CIGALE** fits sources within redshift blocks, where it pre-compile a set of models first and then estimates the best-fit parameters, while **Stardust** fits sources sequentially. As such, despite both methods being parallelised, it is difficult to achieve a fair comparison between the two. Within a single redshift block, that numbers 288 objects, **CIGALE** has computed  $50 \times 10^6$  models, and found the best fit in about 2.5 hours. Due to how the linear combination is performed within **Stardust**, defining an exact number of models attempted is not possible. However, considering that the 12 optical templates have been constructed as a basis set of  $\sim 3,000$  models described in Brammer et al. (2008), combining that with 2 AGN templates and  $\sim 4,800$  DL07 models, results in roughly  $30 \times 10^6$  total effective model combinations. Our code then takes 14 minutes in total to fit the same 288 objects, which is approximately 11 times faster than **CIGALE**, for the same number of CPU cores.

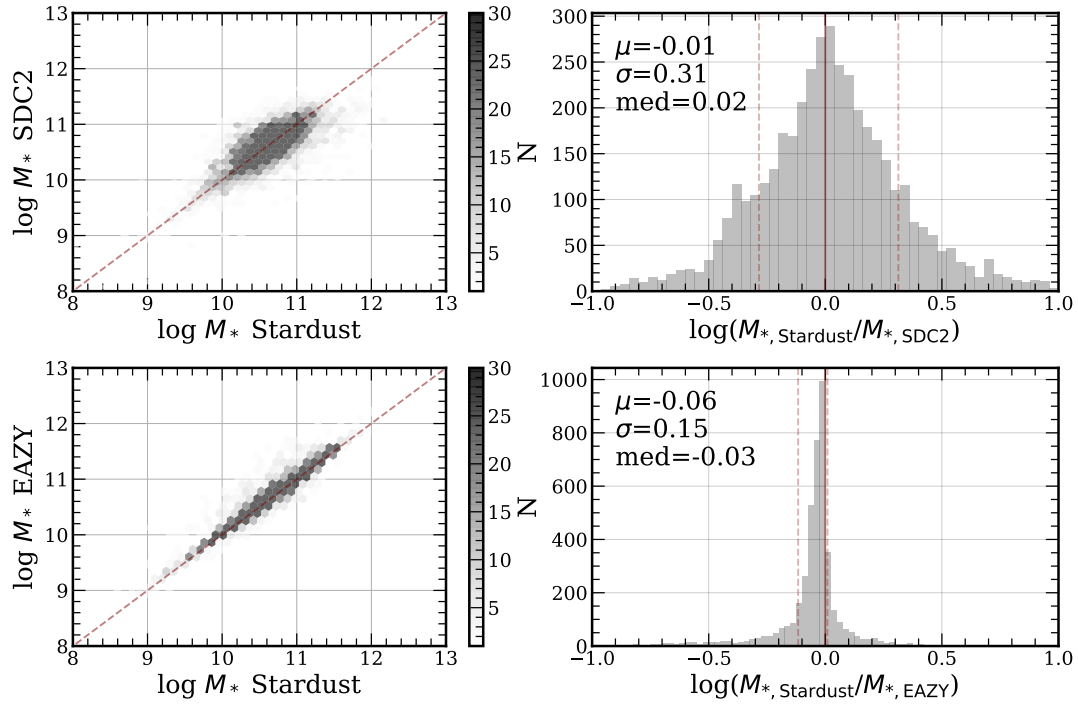


**Figure 20.** Comparison of the *Stardust* derived  $M_*$  vs SDC2 (top) and EAZY (bottom). The dashed maroon line represents a 1:1 relation. The solid and dashed maroon lines represent a 1:1 relation and the 68 % confidence interval, respectively.



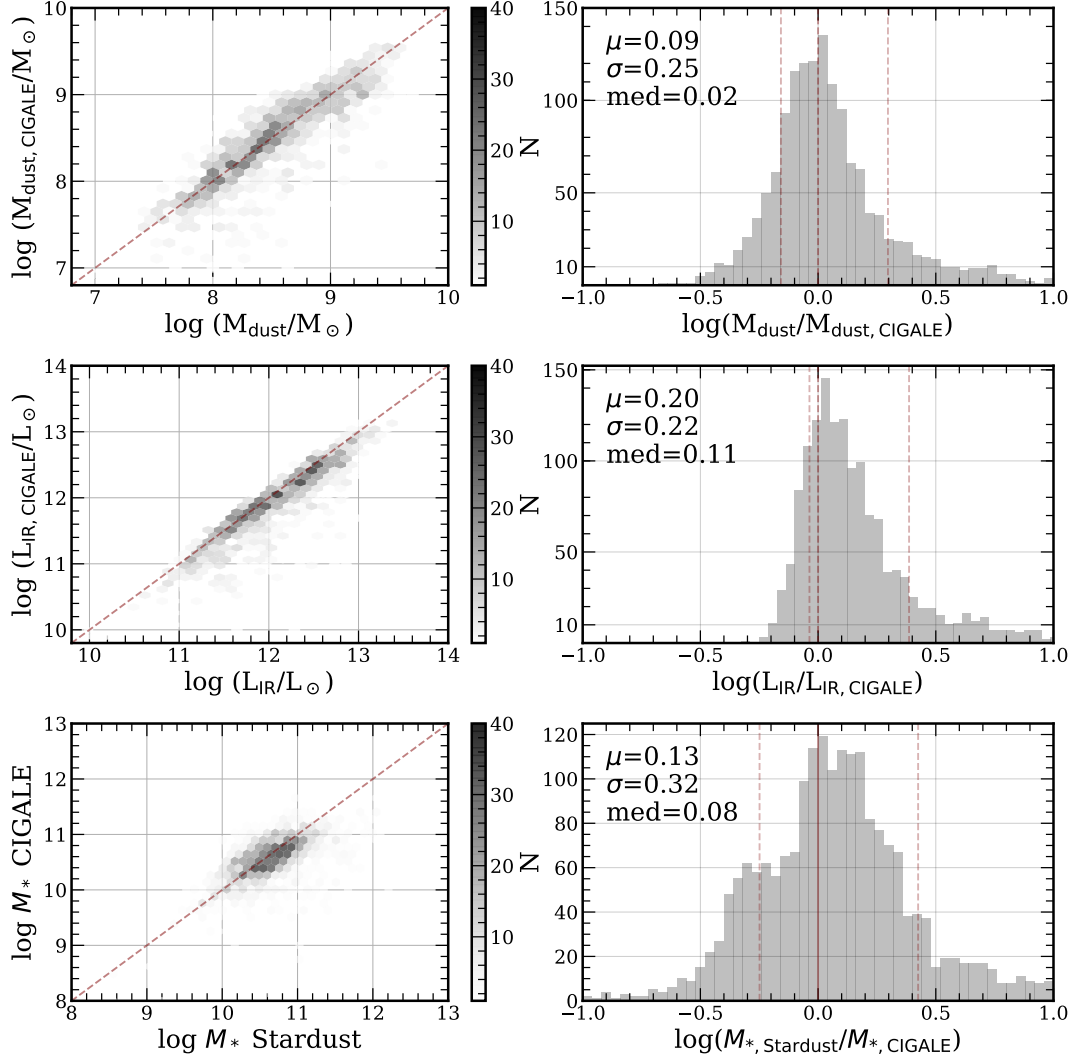


**Figure 21.** Comparison of the derived  $M_{\text{dust}}$  (top) and  $L_{\text{IR}}$  (bottom) between Stardust and CIGALE. The solid and dashed maroon lines represent a 1:1 relation and the 68 % confidence interval, respectively.

**Table 3.** Structure of the best-fit catalogue<sup>a</sup>

Column Name	Units	Description
ID	-	ID of the object from the parent catalogue
RA	deg	The right ascension coordinate, as given in the parent catalogue
DEC	deg	The declination, as given in the parent catalogue
Area	-	Same as <code>goodArea</code> flag in the parent catalogues
z	-	Redshift used for fitting
ztype	-	Redshift type, 1 for spectroscopic, 0 for photometric, and 2 for $z_{\text{phot}}$ from <b>EAZY</b>
LIR_total	$L_{\odot}$	Total FIR luminosity, obtained as the sum between AGN and DL07 components
eLIR_total	$L_{\odot}$	Uncertainty on the total FIR luminosity
Lagn_total	$L_{\odot}$	AGN luminosity
eLagn_total	$L_{\odot}$	Uncertainty on the AGN luminosity
Lir_draine	$L_{\odot}$	Luminosity given by the DL07 template
eLir_draine	$L_{\odot}$	Uncertainty on the luminosity given by the DL07 template
MD	$M_{\odot}$	Dust mass as predicted by the best-fit DL07 template
eMD	$M_{\odot}$	Uncertainty on the dust mass
deltaGDR	-	Gas-to-dust ratio
MG	$M_{\odot}$	Gas mass computed from $\delta_{\text{GDR}}$ and $M_{\text{dust}}$
eMG	$M_{\odot}$	The uncertainty on gas mass
Mstar	$M_{\odot}$	Stellar mass, equal to the one in the original catalogue
lastdet	$\mu\text{m}$	Last band that has a S/N > 3 detection ( $\lambda_{\text{last}}$ ). Given in rest frame.
chi2	-	The $\chi^2$ of the best-fit coefficients
fagn	-	AGN fraction, given as $L_{\text{AGN}}/L_{\text{IR,total}}$
efagn	-	Uncertainty on the AGN fraction
fgas	-	Gas fraction computed as $M_{\text{gas}}/M_{\text{dust}}$
fgas_FMR	-	Gas fraction computed assuming $\delta_{\text{GDR}} = 100$
Umin	-	Best fit $U_{\text{min}}$
gamma	-	Best fit $\gamma$
qpah	-	Index of the best fit $q_{\text{PAH}}$ value
U	-	Average radiation field intensity $\langle U \rangle$
sU	-	Uncertainty on $\langle U \rangle$
deltaMS	-	SFR/SFR <sub>MS</sub> where SFR = $L_{\text{IR,draine}} \times 10^{-10}$ and SFR <sub>MS</sub> is given by <a href="#">Schreiber et al. 2015</a>
e_deltaMS	-	Uncertainty on $\Delta\text{MS}$

<sup>a</sup> **Stardust** also returns  $M_*$ ,  $A_V$  and UV-optical SFR, these are not included in the release version of the catalogue, but are available upon request.

<sup>b</sup> We have used the 7970d55 (28/06/21) version of **Stardust** to produce these catalogues.

## REFERENCES

- Aniano, G., Draine, B. T., Hunt, L. K., et al. 2020, *ApJ*, 889, 150, doi: [10.3847/1538-4357/ab5fdb](https://doi.org/10.3847/1538-4357/ab5fdb)
- Antonucci, R. 1993, *ARA&A*, 31, 473, doi: [10.1146/annurev.aa.31.090193.002353](https://doi.org/10.1146/annurev.aa.31.090193.002353)
- Aoyama, S., Hirashita, H., Lim, C.-F., et al. 2019, *MNRAS*, 484, 1852, doi: [10.1093/mnras/stz021](https://doi.org/10.1093/mnras/stz021)
- Arnouts, S., Cristiani, S., Moscardini, L., et al. 1999, *MNRAS*, 310, 540, doi: [10.1046/j.1365-8711.1999.02978.x](https://doi.org/10.1046/j.1365-8711.1999.02978.x)
- Avni, Y. 1976, *ApJ*, 210, 642, doi: [10.1086/154870](https://doi.org/10.1086/154870)
- Battisti, A. J., da Cunha, E., Grasha, K., et al. 2019, *ApJ*, 882, 61, doi: [10.3847/1538-4357/ab345d](https://doi.org/10.3847/1538-4357/ab345d)
- Beeston, R. A., Wright, A. H., Maddox, S., et al. 2018, *MNRAS*, 479, 1077, doi: [10.1093/mnras/sty1460](https://doi.org/10.1093/mnras/sty1460)
- Bendo, G. J., Galliano, F., & Madden, S. C. 2012, *MNRAS*, 423, 197, doi: [10.1111/j.1365-2966.2012.20784.x](https://doi.org/10.1111/j.1365-2966.2012.20784.x)
- Berta, S., Lutz, D., Genzel, R., Förster-Schreiber, N. M., & Tacconi, L. J. 2016, *A&A*, 587, A73, doi: [10.1051/0004-6361/201527746](https://doi.org/10.1051/0004-6361/201527746)
- Berta, S., Lutz, D., Santini, P., et al. 2013, *A&A*, 551, A100, doi: [10.1051/0004-6361/201220859](https://doi.org/10.1051/0004-6361/201220859)
- Bertoldi, F., Carilli, C., Aravena, M., et al. 2007, *ApJS*, 172, 132, doi: [10.1086/520511](https://doi.org/10.1086/520511)
- Béthermin, M., Daddi, E., Magdis, G., et al. 2015, *A&A*, 573, A113, doi: [10.1051/0004-6361/201425031](https://doi.org/10.1051/0004-6361/201425031)
- Béthermin, M., Fudamoto, Y., Ginolfi, M., et al. 2020, *A&A*, 643, A2, doi: [10.1051/0004-6361/202037649](https://doi.org/10.1051/0004-6361/202037649)
- Blanton, M. R., & Roweis, S. 2007, *AJ*, 133, 734, doi: [10.1086/510127](https://doi.org/10.1086/510127)
- Boquien, M., Burgarella, D., Roehlly, Y., et al. 2019, *A&A*, 622, A103, doi: [10.1051/0004-6361/201834156](https://doi.org/10.1051/0004-6361/201834156)
- Boquien, M., Calzetti, D., Combes, F., et al. 2011, *AJ*, 142, 111, doi: [10.1088/0004-6256/142/4/111](https://doi.org/10.1088/0004-6256/142/4/111)
- Brammer, G. B., van Dokkum, P. G., & Coppi, P. 2008, *ApJ*, 686, 1503, doi: [10.1086/591786](https://doi.org/10.1086/591786)
- Brinchmann, J., Charlot, S., White, S. D. M., et al. 2004, *MNRAS*, 351, 1151, doi: [10.1111/j.1365-2966.2004.07881.x](https://doi.org/10.1111/j.1365-2966.2004.07881.x)
- Bruzual, G., & Charlot, S. 2003, *MNRAS*, 344, 1000, doi: [10.1046/j.1365-8711.2003.06897.x](https://doi.org/10.1046/j.1365-8711.2003.06897.x)
- Buat, V., Ciesla, L., Boquien, M., Malek, K., & Burgarella, D. 2019, *A&A*, 632, A79, doi: [10.1051/0004-6361/201936643](https://doi.org/10.1051/0004-6361/201936643)
- Burgarella, D., Buat, V., & Iglesias-Páramo, J. 2005, *MNRAS*, 360, 1413, doi: [10.1111/j.1365-2966.2005.09131.x](https://doi.org/10.1111/j.1365-2966.2005.09131.x)
- Calistro Rivera, G., Lusso, E., Hennawi, J., & Hogg, D. W. 2016, in *Active Galactic Nuclei: What's in a Name?*, 49, doi: [10.5281/zenodo.60461](https://doi.org/10.5281/zenodo.60461)
- Calistro Rivera, G., Hodge, J. A., Smail, I., et al. 2018, *ApJ*, 863, 56, doi: [10.3847/1538-4357/aacffa](https://doi.org/10.3847/1538-4357/aacffa)
- Calzetti, D., Armus, L., Bohlin, R. C., et al. 2000, *ApJ*, 533, 682, doi: [10.1086/308692](https://doi.org/10.1086/308692)
- Carilli, C. L., & Walter, F. 2013, *ARA&A*, 51, 105, doi: [10.1146/annurev-astro-082812-140953](https://doi.org/10.1146/annurev-astro-082812-140953)
- Casey, C. M., Berta, S., Béthermin, M., et al. 2012, *ApJ*, 761, 140, doi: [10.1088/0004-637X/761/2/140](https://doi.org/10.1088/0004-637X/761/2/140)
- Casey, C. M., Zavala, J. A., Spilker, J., et al. 2018, *ApJ*, 862, 77, doi: [10.3847/1538-4357/aac82d](https://doi.org/10.3847/1538-4357/aac82d)
- Casey, C. M., Zavala, J. A., Aravena, M., et al. 2019, *ApJ*, 887, 55, doi: [10.3847/1538-4357/ab52ff](https://doi.org/10.3847/1538-4357/ab52ff)
- Chabrier, G. 2003, *PASP*, 115, 763, doi: [10.1086/376392](https://doi.org/10.1086/376392)
- Chang, Y.-Y., Le Floch, E., Juneau, S., et al. 2017, *MNRAS*, 466, L103, doi: [10.1093/mnrasl/slz247](https://doi.org/10.1093/mnrasl/slz247)
- Chen, C.-C., Hodge, J. A., Smail, I., et al. 2017, *ApJ*, 846, 108, doi: [10.3847/1538-4357/aa863a](https://doi.org/10.3847/1538-4357/aa863a)
- Chen, Y.-M., Wild, V., Kauffmann, G., et al. 2009, *MNRAS*, 393, 406, doi: [10.1111/j.1365-2966.2008.14247.x](https://doi.org/10.1111/j.1365-2966.2008.14247.x)
- Cibinel, A., Daddi, E., Sargent, M. T., et al. 2019, *MNRAS*, 485, 5631, doi: [10.1093/mnras/stz690](https://doi.org/10.1093/mnras/stz690)
- Cochrane, R. K., Best, P. N., Smail, I., et al. 2021, *arXiv e-prints*, arXiv:2102.07791, <https://arxiv.org/abs/2102.07791>
- Cochrane, R. K., Hayward, C. C., Anglés-Alcázar, D., et al. 2019, *MNRAS*, 488, 1779, doi: [10.1093/mnras/stz1736](https://doi.org/10.1093/mnras/stz1736)
- Conroy, C., Gunn, J. E., & White, M. 2009, *ApJ*, 699, 486, doi: [10.1088/0004-637X/699/1/486](https://doi.org/10.1088/0004-637X/699/1/486)
- Cortzen, I., Magdis, G. E., Valentino, F., et al. 2020, *A&A*, 634, L14, doi: [10.1051/0004-6361/201937217](https://doi.org/10.1051/0004-6361/201937217)
- Cousin, M., Buat, V., Lagache, G., & Béthermin, M. 2019, *A&A*, 627, A132, doi: [10.1051/0004-6361/201834674](https://doi.org/10.1051/0004-6361/201834674)
- da Cunha, E., Charlot, S., & Elbaz, D. 2008, *MNRAS*, 388, 1595, doi: [10.1111/j.1365-2966.2008.13535.x](https://doi.org/10.1111/j.1365-2966.2008.13535.x)
- Daddi, E., Dickinson, M., Morrison, G., et al. 2007, *ApJ*, 670, 156, doi: [10.1086/521818](https://doi.org/10.1086/521818)
- Daddi, E., Elbaz, D., Walter, F., et al. 2010, *ApJL*, 714, L118, doi: [10.1088/2041-8205/714/1/L118](https://doi.org/10.1088/2041-8205/714/1/L118)
- Dale, D. A., Helou, G., Magdis, G. E., et al. 2014, *ApJ*, 784, 83, doi: [10.1088/0004-637X/784/1/83](https://doi.org/10.1088/0004-637X/784/1/83)
- Dale, D. A., Aniano, G., Engelbracht, C. W., et al. 2012, *ApJ*, 745, 95, doi: [10.1088/0004-637X/745/1/95](https://doi.org/10.1088/0004-637X/745/1/95)
- Davé, R., Anglés-Alcázar, D., Narayanan, D., et al. 2019, *MNRAS*, 486, 2827, doi: [10.1093/mnras/stz937](https://doi.org/10.1093/mnras/stz937)
- Davé, R., Crain, R. A., Stevens, A. R. H., et al. 2020, *MNRAS*, 497, 146, doi: [10.1093/mnras/staa1894](https://doi.org/10.1093/mnras/staa1894)
- Davé, R., Finlator, K., & Oppenheimer, B. D. 2012, *MNRAS*, 421, 98, doi: [10.1111/j.1365-2966.2011.20148.x](https://doi.org/10.1111/j.1365-2966.2011.20148.x)

- Davé, R., Rafieferantsoa, M. H., Thompson, R. J., & Hopkins, P. F. 2017, *MNRAS*, 467, 115, doi: [10.1093/mnras/stx108](https://doi.org/10.1093/mnras/stx108)
- Davidzon, I., Ilbert, O., Faisst, A. L., Sparre, M., & Capak, P. L. 2018, *ApJ*, 852, 107, doi: [10.3847/1538-4357/aaa19e](https://doi.org/10.3847/1538-4357/aaa19e)
- Davidzon, I., Ilbert, O., Laigle, C., et al. 2017, *A&A*, 605, A70, doi: [10.1051/0004-6361/201730419](https://doi.org/10.1051/0004-6361/201730419)
- Dekel, A., Sari, R., & Ceverino, D. 2009, *ApJ*, 703, 785, doi: [10.1088/0004-637X/703/1/785](https://doi.org/10.1088/0004-637X/703/1/785)
- Delvecchio, I., Daddi, E., Sargent, M. T., et al. 2020, arXiv e-prints, arXiv:2010.05510. <https://arxiv.org/abs/2010.05510>
- Dickinson, M., Giavalisco, M., & GOODS Team. 2003, in *The Mass of Galaxies at Low and High Redshift*, ed. R. Bender & A. Renzini, 324, doi: [10.1007/10899892\\_78](https://doi.org/10.1007/10899892_78)
- Donevski, D., Lapi, A., Malek, K., et al. 2020, arXiv e-prints, arXiv:2008.09995. <https://arxiv.org/abs/2008.09995>
- Draine, B. T., & Li, A. 2007, *ApJ*, 657, 810, doi: [10.1086/511055](https://doi.org/10.1086/511055)
- Draine, B. T., Dale, D. A., Bendo, G., et al. 2007, *ApJ*, 663, 866, doi: [10.1086/518306](https://doi.org/10.1086/518306)
- Draine, B. T., Aniano, G., Krause, O., et al. 2014, *ApJ*, 780, 172, doi: [10.1088/0004-637X/780/2/172](https://doi.org/10.1088/0004-637X/780/2/172)
- Driver, S. P., Andrews, S. K., da Cunha, E., et al. 2018, *MNRAS*, 475, 2891, doi: [10.1093/mnras/stx2728](https://doi.org/10.1093/mnras/stx2728)
- Dubois, Y., Pichon, C., Welker, C., et al. 2014, *MNRAS*, 444, 1453, doi: [10.1093/mnras/stu1227](https://doi.org/10.1093/mnras/stu1227)
- Dunlop, J. S., McLure, R. J., Biggs, A. D., et al. 2017, *MNRAS*, 466, 861, doi: [10.1093/mnras/stw3088](https://doi.org/10.1093/mnras/stw3088)
- Dunne, L., Gomez, H. L., da Cunha, E., et al. 2011, *MNRAS*, 417, 1510, doi: [10.1111/j.1365-2966.2011.19363.x](https://doi.org/10.1111/j.1365-2966.2011.19363.x)
- Eales, S., Smith, M. W. L., Auld, R., et al. 2012, *ApJ*, 761, 168, doi: [10.1088/0004-637X/761/2/168](https://doi.org/10.1088/0004-637X/761/2/168)
- Elbaz, D., Daddi, E., Le Borgne, D., et al. 2007, *A&A*, 468, 33, doi: [10.1051/0004-6361:20077525](https://doi.org/10.1051/0004-6361:20077525)
- Elbaz, D., Hwang, H. S., Magnelli, B., et al. 2010, *A&A*, 518, L29, doi: [10.1051/0004-6361/201014687](https://doi.org/10.1051/0004-6361/201014687)
- Elbaz, D., Dickinson, M., Hwang, H. S., et al. 2011, *A&A*, 533, A119, doi: [10.1051/0004-6361/201117239](https://doi.org/10.1051/0004-6361/201117239)
- Elbaz, D., Leiton, R., Nagar, N., et al. 2018, *A&A*, 616, A110, doi: [10.1051/0004-6361/201732370](https://doi.org/10.1051/0004-6361/201732370)
- Erfanianfar, G., Popesso, P., Finoguenov, A., et al. 2016, *MNRAS*, 455, 2839, doi: [10.1093/mnras/stv2485](https://doi.org/10.1093/mnras/stv2485)
- Feltre, A., Hatziminaoglou, E., Hernán-Caballero, A., et al. 2013, *MNRAS*, 434, 2426, doi: [10.1093/mnras/stt1177](https://doi.org/10.1093/mnras/stt1177)
- Franco, M., Elbaz, D., Béthermin, M., et al. 2018, *A&A*, 620, A152, doi: [10.1051/0004-6361/201832928](https://doi.org/10.1051/0004-6361/201832928)
- Franco, M., Elbaz, D., Zhou, L., et al. 2020, *A&A*, 643, A30, doi: [10.1051/0004-6361/202038312](https://doi.org/10.1051/0004-6361/202038312)
- Fritz, J., Franceschini, A., & Hatziminaoglou, E. 2006, *MNRAS*, 366, 767, doi: [10.1111/j.1365-2966.2006.09866.x](https://doi.org/10.1111/j.1365-2966.2006.09866.x)
- Galametz, M., Albrecht, M., Kennicutt, R., et al. 2014, *MNRAS*, 439, 2542, doi: [10.1093/mnras/stu113](https://doi.org/10.1093/mnras/stu113)
- Geach, J. E., Smail, I., Moran, S. M., et al. 2011, *ApJL*, 730, L19, doi: [10.1088/2041-8205/730/2/L19](https://doi.org/10.1088/2041-8205/730/2/L19)
- Geach, J. E., Dunlop, J. S., Halpern, M., et al. 2017, *MNRAS*, 465, 1789, doi: [10.1093/mnras/stw2721](https://doi.org/10.1093/mnras/stw2721)
- Genzel, R., Tacconi, L. J., Lutz, D., et al. 2015, *ApJ*, 800, 20, doi: [10.1088/0004-637X/800/1/20](https://doi.org/10.1088/0004-637X/800/1/20)
- Goldsmith, P. F. 2001, *ApJ*, 557, 736, doi: [10.1086/322255](https://doi.org/10.1086/322255)
- Gómez-Guijarro, C., Toft, S., Karim, A., et al. 2018, *ApJ*, 856, 121, doi: [10.3847/1538-4357/aab206](https://doi.org/10.3847/1538-4357/aab206)
- Groves, B. A., Schinnerer, E., Leroy, A., et al. 2015, *ApJ*, 799, 96, doi: [10.1088/0004-637X/799/1/96](https://doi.org/10.1088/0004-637X/799/1/96)
- Hayward, C. C., Narayanan, D., Kereš, D., et al. 2013, *MNRAS*, 428, 2529, doi: [10.1093/mnras/sts222](https://doi.org/10.1093/mnras/sts222)
- Hayward, C. C., Lanz, L., Ashby, M. L. N., et al. 2014, *MNRAS*, 445, 1598, doi: [10.1093/mnras/stu1843](https://doi.org/10.1093/mnras/stu1843)
- Hodge, J. A., & da Cunha, E. 2020, *Royal Society Open Science*, 7, 200556, doi: [10.1098/rsos.200556](https://doi.org/10.1098/rsos.200556)
- Hodge, J. A., Swinbank, A. M., Simpson, J. M., et al. 2016, *ApJ*, 833, 103, doi: [10.3847/1538-4357/833/1/103](https://doi.org/10.3847/1538-4357/833/1/103)
- Hodge, J. A., Smail, I., Walter, F., et al. 2019, *ApJ*, 876, 130, doi: [10.3847/1538-4357/ab1846](https://doi.org/10.3847/1538-4357/ab1846)
- Ilbert, O., Arnouts, S., McCracken, H. J., et al. 2006, *A&A*, 457, 841, doi: [10.1051/0004-6361:20065138](https://doi.org/10.1051/0004-6361:20065138)
- Imara, N., Loeb, A., Johnson, B. D., Conroy, C., & Behroozi, P. 2018, *ApJ*, 854, 36, doi: [10.3847/1538-4357/aaa3f0](https://doi.org/10.3847/1538-4357/aaa3f0)
- Jin, S., Daddi, E., Liu, D., et al. 2018, *ApJ*, 864, 56, doi: [10.3847/1538-4357/aad4af](https://doi.org/10.3847/1538-4357/aad4af)
- Jin, S., Daddi, E., Magdis, G. E., et al. 2019, *ApJ*, 887, 144, doi: [10.3847/1538-4357/ab55d6](https://doi.org/10.3847/1538-4357/ab55d6)
- Kaasinen, M., Walter, F., Novak, M., et al. 2020, *ApJ*, 899, 37, doi: [10.3847/1538-4357/aba438](https://doi.org/10.3847/1538-4357/aba438)
- Karim, A., Schinnerer, E., Martínez-Sansigre, A., et al. 2011, *ApJ*, 730, 61, doi: [10.1088/0004-637X/730/2/61](https://doi.org/10.1088/0004-637X/730/2/61)
- Kashino, D., Silverman, J. D., Rodighiero, G., et al. 2013, *ApJL*, 777, L8, doi: [10.1088/2041-8205/777/1/L8](https://doi.org/10.1088/2041-8205/777/1/L8)
- Kennicutt, Robert C., J. 1998, *ARA&A*, 36, 189, doi: [10.1146/annurev.astro.36.1.189](https://doi.org/10.1146/annurev.astro.36.1.189)
- Kewley, L. J., & Dopita, M. A. 2002, *ApJS*, 142, 35, doi: [10.1086/341326](https://doi.org/10.1086/341326)
- Kewley, L. J., & Ellison, S. L. 2008, *ApJ*, 681, 1183, doi: [10.1086/587500](https://doi.org/10.1086/587500)
- Kriek, M., van Dokkum, P. G., Labbé, I., et al. 2009, *ApJ*, 700, 221, doi: [10.1088/0004-637X/700/1/221](https://doi.org/10.1088/0004-637X/700/1/221)



- Krumholz, M. R., Klein, R. I., & McKee, C. F. 2011, *ApJ*, 740, 74, doi: [10.1088/0004-637X/740/2/74](https://doi.org/10.1088/0004-637X/740/2/74)
- Kurczynski, P., Gawiser, E., Acquaviva, V., et al. 2016, *ApJL*, 820, L1, doi: [10.3847/2041-8205/820/1/L1](https://doi.org/10.3847/2041-8205/820/1/L1)
- Lacey, C. G., Baugh, C. M., Frenk, C. S., et al. 2016, *MNRAS*, 462, 3854, doi: [10.1093/mnras/stw1888](https://doi.org/10.1093/mnras/stw1888)
- Lagos, C. d. P., da Cunha, E., Robotham, A. S. G., et al. 2020, *MNRAS*, 499, 1948, doi: [10.1093/mnras/staa2861](https://doi.org/10.1093/mnras/staa2861)
- Lagos, C. d. P., Crain, R. A., Schaye, J., et al. 2015, *MNRAS*, 452, 3815, doi: [10.1093/mnras/stv1488](https://doi.org/10.1093/mnras/stv1488)
- Lagos, C. d. P., Robotham, A. S. G., Trayford, J. W., et al. 2019, *MNRAS*, 489, 4196, doi: [10.1093/mnras/stz2427](https://doi.org/10.1093/mnras/stz2427)
- Laigle, C., McCracken, H. J., Ilbert, O., et al. 2016, *ApJS*, 224, 24, doi: [10.3847/0067-0049/224/2/24](https://doi.org/10.3847/0067-0049/224/2/24)
- Laigle, C., Davidzon, I., Ilbert, O., et al. 2019, *MNRAS*, 486, 5104, doi: [10.1093/mnras/stz1054](https://doi.org/10.1093/mnras/stz1054)
- Lee, K.-S., Ferguson, H. C., Wiklind, T., et al. 2012, *ApJ*, 752, 66, doi: [10.1088/0004-637X/752/1/66](https://doi.org/10.1088/0004-637X/752/1/66)
- Lee, N., Sanders, D. B., Casey, C. M., et al. 2015, *ApJ*, 801, 80, doi: [10.1088/0004-637X/801/2/80](https://doi.org/10.1088/0004-637X/801/2/80)
- Leja, J., Johnson, B. D., Conroy, C., & van Dokkum, P. 2018, *ApJ*, 854, 62, doi: [10.3847/1538-4357/aaa8db](https://doi.org/10.3847/1538-4357/aaa8db)
- Leroy, A. K., Bolatto, A., Gordon, K., et al. 2011, *ApJ*, 737, 12, doi: [10.1088/0004-637X/737/1/12](https://doi.org/10.1088/0004-637X/737/1/12)
- Leslie, S. K., Schinnerer, E., Liu, D., et al. 2020, *ApJ*, 899, 58, doi: [10.3847/1538-4357/aba044](https://doi.org/10.3847/1538-4357/aba044)
- Liang, L., Feldmann, R., Kereš, D., et al. 2019, *MNRAS*, 489, 1397, doi: [10.1093/mnras/stz2134](https://doi.org/10.1093/mnras/stz2134)
- Lilly, S. J., Carollo, C. M., Pipino, A., Renzini, A., & Peng, Y. 2013, *ApJ*, 772, 119, doi: [10.1088/0004-637X/772/2/119](https://doi.org/10.1088/0004-637X/772/2/119)
- Liu, D., Daddi, E., Dickinson, M., et al. 2018, *ApJ*, 853, 172, doi: [10.3847/1538-4357/aaa600](https://doi.org/10.3847/1538-4357/aaa600)
- Liu, D., Lang, P., Magnelli, B., et al. 2019a, *ApJS*, 244, 40, doi: [10.3847/1538-4365/ab42da](https://doi.org/10.3847/1538-4365/ab42da)
- Liu, D., Schinnerer, E., Groves, B., et al. 2019b, *ApJ*, 887, 235, doi: [10.3847/1538-4357/ab578d](https://doi.org/10.3847/1538-4357/ab578d)
- Liu, D., Daddi, E., Schinnerer, E., et al. 2021, arXiv e-prints, arXiv:2101.06646. <https://arxiv.org/abs/2101.06646>
- Loveday, J., Peterson, B. A., Efstathiou, G., & Maddox, S. J. 1992, *ApJ*, 390, 338, doi: [10.1086/171284](https://doi.org/10.1086/171284)
- Lutz, D., Poglitsch, A., Altieri, B., et al. 2011, *A&A*, 532, A90, doi: [10.1051/0004-6361/201117107](https://doi.org/10.1051/0004-6361/201117107)
- Maddox, S. J., Valiante, E., Cigan, P., et al. 2018, *ApJS*, 236, 30, doi: [10.3847/1538-4365/aab8fc](https://doi.org/10.3847/1538-4365/aab8fc)
- Magdis, G. E., Elbaz, D., Daddi, E., et al. 2010, *ApJ*, 714, 1740, doi: [10.1088/0004-637X/714/2/1740](https://doi.org/10.1088/0004-637X/714/2/1740)
- Magdis, G. E., Daddi, E., Elbaz, D., et al. 2011, *ApJL*, 740, L15, doi: [10.1088/2041-8205/740/1/L15](https://doi.org/10.1088/2041-8205/740/1/L15)
- Magdis, G. E., Daddi, E., Béthermin, M., et al. 2012a, *ApJ*, 760, 6, doi: [10.1088/0004-637X/760/1/6](https://doi.org/10.1088/0004-637X/760/1/6)
- Magdis, G. E., Daddi, E., Sargent, M., et al. 2012b, *ApJL*, 758, L9, doi: [10.1088/2041-8205/758/1/L9](https://doi.org/10.1088/2041-8205/758/1/L9)
- Magdis, G. E., Rigopoulou, D., Helou, G., et al. 2013, *A&A*, 558, A136, doi: [10.1051/0004-6361/201322226](https://doi.org/10.1051/0004-6361/201322226)
- Magdis, G. E., Rigopoulou, D., Daddi, E., et al. 2017, *A&A*, 603, A93, doi: [10.1051/0004-6361/201731037](https://doi.org/10.1051/0004-6361/201731037)
- Magdis, G. E., Gobat, R., Valentino, F., et al. 2021, arXiv e-prints, arXiv:2101.04700. <https://arxiv.org/abs/2101.04700>
- Magnelli, B., Lutz, D., Santini, P., et al. 2012, *A&A*, 539, A155, doi: [10.1051/0004-6361/201118312](https://doi.org/10.1051/0004-6361/201118312)
- Magnelli, B., Popesso, P., Berta, S., et al. 2013, *A&A*, 553, A132, doi: [10.1051/0004-6361/201321371](https://doi.org/10.1051/0004-6361/201321371)
- Magnelli, B., Lutz, D., Saintonge, A., et al. 2014, *A&A*, 561, A86, doi: [10.1051/0004-6361/201322217](https://doi.org/10.1051/0004-6361/201322217)
- Magnelli, B., Boogaard, L., Decarli, R., et al. 2020, *ApJ*, 892, 66, doi: [10.3847/1538-4357/ab7897](https://doi.org/10.3847/1538-4357/ab7897)
- Małek, K., Buat, V., Roehlly, Y., et al. 2018, *A&A*, 620, A50, doi: [10.1051/0004-6361/201833131](https://doi.org/10.1051/0004-6361/201833131)
- Mannucci, F., Cresci, G., Maiolino, R., Marconi, A., & Gnerucci, A. 2010, *MNRAS*, 408, 2115, doi: [10.1111/j.1365-2966.2010.17291.x](https://doi.org/10.1111/j.1365-2966.2010.17291.x)
- McCracken, H. J., Milvang-Jensen, B., Dunlop, J., et al. 2012, *A&A*, 544, A156, doi: [10.1051/0004-6361/201219507](https://doi.org/10.1051/0004-6361/201219507)
- McKinnon, R., Torrey, P., Vogelsberger, M., Hayward, C. C., & Marinacci, F. 2017, *MNRAS*, 468, 1505, doi: [10.1093/mnras/stx467](https://doi.org/10.1093/mnras/stx467)
- Millard, J. S., Diemer, B., Eales, S. A., et al. 2020, *MNRAS*, doi: [10.1093/mnras/staa3207](https://doi.org/10.1093/mnras/staa3207)
- Moustakas, J., Coil, A. L., Aird, J., et al. 2013, *ApJ*, 767, 50, doi: [10.1088/0004-637X/767/1/50](https://doi.org/10.1088/0004-637X/767/1/50)
- Mullaney, J. R., Alexander, D. M., Goulding, A. D., & Hickox, R. C. 2011, *MNRAS*, 414, 1082, doi: [10.1111/j.1365-2966.2011.18448.x](https://doi.org/10.1111/j.1365-2966.2011.18448.x)
- Muzzin, A., Marchesini, D., Stefanon, M., et al. 2013, *ApJ*, 777, 18, doi: [10.1088/0004-637X/777/1/18](https://doi.org/10.1088/0004-637X/777/1/18)
- Narayanan, D., & Davé, R. 2012, *MNRAS*, 423, 3601, doi: [10.1111/j.1365-2966.2012.21159.x](https://doi.org/10.1111/j.1365-2966.2012.21159.x)
- Narayanan, D., Krumholz, M., Ostriker, E. C., & Hernquist, L. 2011, *MNRAS*, 418, 664, doi: [10.1111/j.1365-2966.2011.19516.x](https://doi.org/10.1111/j.1365-2966.2011.19516.x)
- Narayanan, D., Krumholz, M. R., Ostriker, E. C., & Hernquist, L. 2012, *MNRAS*, 421, 3127, doi: [10.1111/j.1365-2966.2012.20536.x](https://doi.org/10.1111/j.1365-2966.2012.20536.x)
- Narayanan, D., Turk, M., Feldmann, R., et al. 2015, *Nature*, 525, 496, doi: [10.1038/nature15383](https://doi.org/10.1038/nature15383)

- Noeske, K. G., Weiner, B. J., Faber, S. M., et al. 2007, *ApJL*, 660, L43, doi: [10.1086/517926](https://doi.org/10.1086/517926)
- Noll, S., Burgarella, D., Giovannoli, E., et al. 2009, *A&A*, 507, 1793, doi: [10.1051/0004-6361/200912497](https://doi.org/10.1051/0004-6361/200912497)
- Oliver, S., Frost, M., Farrah, D., et al. 2010, *MNRAS*, 405, 2279, doi: [10.1111/j.1365-2966.2010.16643.x](https://doi.org/10.1111/j.1365-2966.2010.16643.x)
- Oliver, S. J., Bock, J., Altieri, B., et al. 2012, *MNRAS*, 424, 1614, doi: [10.1111/j.1365-2966.2012.20912.x](https://doi.org/10.1111/j.1365-2966.2012.20912.x)
- Owen, F. N. 2018, *ApJS*, 235, 34, doi: [10.3847/1538-4365/aab4a1](https://doi.org/10.3847/1538-4365/aab4a1)
- Pannella, M., Carilli, C. L., Daddi, E., et al. 2009, *ApJL*, 698, L116, doi: [10.1088/0004-637X/698/2/L116](https://doi.org/10.1088/0004-637X/698/2/L116)
- Pannella, M., Elbaz, D., Daddi, E., et al. 2015, *ApJ*, 807, 141, doi: [10.1088/0004-637X/807/2/141](https://doi.org/10.1088/0004-637X/807/2/141)
- Pantoni, L., Lapi, A., Massardi, M., Goswami, S., & Danese, L. 2019, *ApJ*, 880, 129, doi: [10.3847/1538-4357/ab2adc](https://doi.org/10.3847/1538-4357/ab2adc)
- Pearson, W. J., Wang, L., Hurley, P. D., et al. 2018, *A&A*, 615, A146, doi: [10.1051/0004-6361/201832821](https://doi.org/10.1051/0004-6361/201832821)
- Penner, K., Pope, A., Chapin, E. L., et al. 2011, *MNRAS*, 410, 2749, doi: [10.1111/j.1365-2966.2010.17650.x](https://doi.org/10.1111/j.1365-2966.2010.17650.x)
- Pettini, M., & Pagel, B. E. J. 2004, *MNRAS*, 348, L59, doi: [10.1111/j.1365-2966.2004.07591.x](https://doi.org/10.1111/j.1365-2966.2004.07591.x)
- Pillepich, A., Nelson, D., Springel, V., et al. 2019, *MNRAS*, 490, 3196, doi: [10.1093/mnras/stz2338](https://doi.org/10.1093/mnras/stz2338)
- Popping, G., Somerville, R. S., & Galametz, M. 2017, *MNRAS*, 471, 3152, doi: [10.1093/mnras/stx1545](https://doi.org/10.1093/mnras/stx1545)
- Popping, G., Somerville, R. S., & Trager, S. C. 2014, *MNRAS*, 442, 2398, doi: [10.1093/mnras/stu991](https://doi.org/10.1093/mnras/stu991)
- Popping, G., Pillepich, A., Calistro Rivera, G., et al. 2021, arXiv e-prints, arXiv:2101.12218. <https://arxiv.org/abs/2101.12218>
- Pozzi, F., Calura, F., Zamorani, G., et al. 2020, *MNRAS*, 491, 5073, doi: [10.1093/mnras/stz2724](https://doi.org/10.1093/mnras/stz2724)
- Press, W. H., Flannery, B. P., & Teukolsky, S. A. 1986, *Numerical recipes. The art of scientific computing* (Cambridge University Press)
- Puglisi, A., Daddi, E., Liu, D., et al. 2019, *ApJL*, 877, L23, doi: [10.3847/2041-8213/ab1f92](https://doi.org/10.3847/2041-8213/ab1f92)
- Reddy, N., Dickinson, M., Elbaz, D., et al. 2012, *ApJ*, 744, 154, doi: [10.1088/0004-637X/744/2/154](https://doi.org/10.1088/0004-637X/744/2/154)
- Reiter, M., Guzmán, A. E., Haworth, T. J., et al. 2020, *MNRAS*, 496, 394, doi: [10.1093/mnras/staa1504](https://doi.org/10.1093/mnras/staa1504)
- Rémy-Ruyer, A., Madden, S. C., Galliano, F., et al. 2014, *A&A*, 563, A31, doi: [10.1051/0004-6361/201322803](https://doi.org/10.1051/0004-6361/201322803)
- Rodighiero, G., Daddi, E., Baronchelli, I., et al. 2011, *ApJL*, 739, L40, doi: [10.1088/2041-8205/739/2/L40](https://doi.org/10.1088/2041-8205/739/2/L40)
- Rodighiero, G., Renzini, A., Daddi, E., et al. 2014, *MNRAS*, 443, 19, doi: [10.1093/mnras/stu1110](https://doi.org/10.1093/mnras/stu1110)
- Saintonge, A., Catinella, B., Tacconi, L. J., et al. 2017, *ApJS*, 233, 22, doi: [10.3847/1538-4365/aa97e0](https://doi.org/10.3847/1538-4365/aa97e0)
- Salim, S., Rich, R. M., Charlot, S., et al. 2007, *ApJS*, 173, 267, doi: [10.1086/519218](https://doi.org/10.1086/519218)
- Salmi, F., Daddi, E., Elbaz, D., et al. 2012, *ApJL*, 754, L14, doi: [10.1088/2041-8205/754/1/L14](https://doi.org/10.1088/2041-8205/754/1/L14)
- Salpeter, E. E. 1955, *ApJ*, 121, 161, doi: [10.1086/145971](https://doi.org/10.1086/145971)
- Santini, P., Fontana, A., Grazian, A., et al. 2009, *A&A*, 504, 751, doi: [10.1051/0004-6361/200811434](https://doi.org/10.1051/0004-6361/200811434)
- Santini, P., Maiolino, R., Magnelli, B., et al. 2014, *A&A*, 562, A30, doi: [10.1051/0004-6361/201322835](https://doi.org/10.1051/0004-6361/201322835)
- Santini, P., Fontana, A., Castellano, M., et al. 2017, *ApJ*, 847, 76, doi: [10.3847/1538-4357/aa8874](https://doi.org/10.3847/1538-4357/aa8874)
- Sargent, M. T., Daddi, E., Béthermin, M., et al. 2014, *ApJ*, 793, 19, doi: [10.1088/0004-637X/793/1/19](https://doi.org/10.1088/0004-637X/793/1/19)
- Schechter, P. 1976, *ApJ*, 203, 297, doi: [10.1086/154079](https://doi.org/10.1086/154079)
- Schmidt, M. 1968, *ApJ*, 151, 393, doi: [10.1086/149446](https://doi.org/10.1086/149446)
- Schreiber, C., Elbaz, D., Pannella, M., et al. 2018, *A&A*, 609, A30, doi: [10.1051/0004-6361/201731506](https://doi.org/10.1051/0004-6361/201731506)
- Schreiber, C., Pannella, M., Elbaz, D., et al. 2015, *A&A*, 575, A74, doi: [10.1051/0004-6361/201425017](https://doi.org/10.1051/0004-6361/201425017)
- Scoville, N., Aussel, H., Brusa, M., et al. 2007, *ApJS*, 172, 1, doi: [10.1086/516585](https://doi.org/10.1086/516585)
- Scoville, N., Sheth, K., Aussel, H., et al. 2016, *ApJ*, 820, 83, doi: [10.3847/0004-637X/820/2/83](https://doi.org/10.3847/0004-637X/820/2/83)
- Scoville, N., Lee, N., Vanden Bout, P., et al. 2017, *ApJ*, 837, 150, doi: [10.3847/1538-4357/aa61a0](https://doi.org/10.3847/1538-4357/aa61a0)
- Shim, H., Chary, R.-R., Dickinson, M., et al. 2011, *ApJ*, 738, 69, doi: [10.1088/0004-637X/738/1/69](https://doi.org/10.1088/0004-637X/738/1/69)
- Shivaei, I., Reddy, N. A., Steidel, C. C., & Shapley, A. E. 2015, *ApJ*, 804, 149, doi: [10.1088/0004-637X/804/2/149](https://doi.org/10.1088/0004-637X/804/2/149)
- Silverman, J. D., Daddi, E., Rodighiero, G., et al. 2015, *ApJL*, 812, L23, doi: [10.1088/2041-8205/812/2/L23](https://doi.org/10.1088/2041-8205/812/2/L23)
- Silverman, J. D., Rujopakarn, W., Daddi, E., et al. 2018, *ApJ*, 867, 92, doi: [10.3847/1538-4357/aae25e](https://doi.org/10.3847/1538-4357/aae25e)
- Simpson, J. M., Smail, I., Swinbank, A. M., et al. 2015, *ApJ*, 799, 81, doi: [10.1088/0004-637X/799/1/81](https://doi.org/10.1088/0004-637X/799/1/81)
- Skelton, R. E., Whitaker, K. E., Momcheva, I. G., et al. 2014, *ApJS*, 214, 24, doi: [10.1088/0067-0049/214/2/24](https://doi.org/10.1088/0067-0049/214/2/24)
- Sobral, D., Best, P. N., Smail, I., et al. 2014, *MNRAS*, 437, 3516, doi: [10.1093/mnras/stt2159](https://doi.org/10.1093/mnras/stt2159)
- Speagle, J. S., Steinhardt, C. L., Capak, P. L., & Silverman, J. D. 2014, *ApJS*, 214, 15, doi: [10.1088/0067-0049/214/2/15](https://doi.org/10.1088/0067-0049/214/2/15)
- Steinhardt, C. L., Speagle, J. S., Capak, P., et al. 2014, *ApJL*, 791, L25, doi: [10.1088/2041-8205/791/2/L25](https://doi.org/10.1088/2041-8205/791/2/L25)
- Symeonidis, M., Vaccari, M., Berta, S., et al. 2013, *MNRAS*, 431, 2317, doi: [10.1093/mnras/stt330](https://doi.org/10.1093/mnras/stt330)
- Tacchella, S., Dekel, A., Carollo, C. M., et al. 2016, *MNRAS*, 457, 2790, doi: [10.1093/mnras/stw131](https://doi.org/10.1093/mnras/stw131)

- Tacconi, L. J., Genzel, R., & Sternberg, A. 2020, *ARA&A*, 58, 157, doi: [10.1146/annurev-astro-082812-141034](https://doi.org/10.1146/annurev-astro-082812-141034)
- Tacconi, L. J., Genzel, R., Neri, R., et al. 2010, *Nature*, 463, 781, doi: [10.1038/nature08773](https://doi.org/10.1038/nature08773)
- Tacconi, L. J., Neri, R., Genzel, R., et al. 2013, *ApJ*, 768, 74, doi: [10.1088/0004-637X/768/1/74](https://doi.org/10.1088/0004-637X/768/1/74)
- Tacconi, L. J., Genzel, R., Saintonge, A., et al. 2018, *ApJ*, 853, 179, doi: [10.3847/1538-4357/aaa4b4](https://doi.org/10.3847/1538-4357/aaa4b4)
- Tadaki, K.-i., Genzel, R., Kodama, T., et al. 2017, *ApJ*, 834, 135, doi: [10.3847/1538-4357/834/2/135](https://doi.org/10.3847/1538-4357/834/2/135)
- Tan, Q., Daddi, E., Magdis, G., et al. 2014, *A&A*, 569, A98, doi: [10.1051/0004-6361/201423905](https://doi.org/10.1051/0004-6361/201423905)
- Tasca, L. A. M., Le Fèvre, O., Hathi, N. P., et al. 2015, *A&A*, 581, A54, doi: [10.1051/0004-6361/201425379](https://doi.org/10.1051/0004-6361/201425379)
- Tristram, K. R. W., Meisenheimer, K., Jaffe, W., et al. 2007, *A&A*, 474, 837, doi: [10.1051/0004-6361:20078369](https://doi.org/10.1051/0004-6361:20078369)
- Urry, C. M., & Padovani, P. 1995, *PASP*, 107, 803, doi: [10.1086/133630](https://doi.org/10.1086/133630)
- Valentino, F., Magdis, G. E., Daddi, E., et al. 2020, *ApJ*, 890, 24, doi: [10.3847/1538-4357/ab6603](https://doi.org/10.3847/1538-4357/ab6603)
- van der Wel, A., Chang, Y.-Y., Bell, E. F., et al. 2014, *ApJL*, 792, L6, doi: [10.1088/2041-8205/792/1/L6](https://doi.org/10.1088/2041-8205/792/1/L6)
- Vijayan, A. P., Clay, S. J., Thomas, P. A., et al. 2019, *MNRAS*, 489, 4072, doi: [10.1093/mnras/stz1948](https://doi.org/10.1093/mnras/stz1948)
- Walter, F., Decarli, R., Aravena, M., et al. 2016, *ApJ*, 833, 67, doi: [10.3847/1538-4357/833/1/67](https://doi.org/10.3847/1538-4357/833/1/67)
- Wang, T., Elbaz, D., Schreiber, C., et al. 2016, *ApJ*, 816, 84, doi: [10.3847/0004-637X/816/2/84](https://doi.org/10.3847/0004-637X/816/2/84)
- Weigel, A. K., Schawinski, K., & Bruderer, C. 2016, *MNRAS*, 459, 2150, doi: [10.1093/mnras/stw756](https://doi.org/10.1093/mnras/stw756)
- Whitaker, K. E., van Dokkum, P. G., Brammer, G., & Franx, M. 2012, *ApJL*, 754, L29, doi: [10.1088/2041-8205/754/2/L29](https://doi.org/10.1088/2041-8205/754/2/L29)
- Whitaker, K. E., Franx, M., Leja, J., et al. 2014, *ApJ*, 795, 104, doi: [10.1088/0004-637X/795/2/104](https://doi.org/10.1088/0004-637X/795/2/104)
- Whitaker, K. E., Franx, M., Bezanson, R., et al. 2015, *ApJL*, 811, L12, doi: [10.1088/2041-8205/811/1/L12](https://doi.org/10.1088/2041-8205/811/1/L12)
- Williams, C. C., Spilker, J. S., Whitaker, K. E., et al. 2020, arXiv e-prints, arXiv:2012.01433. <https://arxiv.org/abs/2012.01433>
- Zahid, H. J., Bresolin, F., Kewley, L. J., Coil, A. L., & Davé, R. 2012, *ApJ*, 750, 120, doi: [10.1088/0004-637X/750/2/120](https://doi.org/10.1088/0004-637X/750/2/120)